Faculty of Physics and Astronomy
University of Heidelberg

Master Thesis in Physics
submitted by

Marc Botz

born in Weinheim (Germany)

2022

Experimental Determination of Relative Electron Collision Excitation Cross Sections of Highly Charged Tin in an EBIT

This Master Thesis has been conducted by Marc Botz at the
Max-Planck-Institut for Nuclear Physics in Heidelberg
under supervision of
Prof. Dr. José R. Crespo López-Urrutia
and
Prof. Dr. Thomas Pfeifer

Abstract

As previously calculated, the contribution of transitions between multiply excited states to the EUV(extreme ultraviolet)-spectrum of laser produced tin plasmas may be larger than initially presumed. Experimental data, probing line intensities for varying degrees of excitation, needs to be delivered for further investigation of this phenomenon. To achieve this, highly charged tin ions of several selected charge states (Sn^{11+}-Sn^{15+}) were produced and trapped inside an electron beam ion trap (EBIT) and brought into contact with electrons of varying kinetic energies during fast energy sweeps of up to 200 ms duration. The spontaneously emitted EUV-radiation around the industrially relevant 13.5 nm-region, following collisional excitation, was recorded and related to the electron energy. Projecting the intensity of each recorded spectral line onto the kinetic energy of the beam electrons, allowed extracting relative collisional excitation cross sections. Comparing this experimental data to both the results of fits employing multiple Van Regemorter relations as well as calculations using the collisional radiative model included in the flexible atomic code (FAC), additional energy thresholds for the production of EUV light in tin were found. Consequently the contribution of transitions between multiply excited states to the EUV spectrum were experimentally determined.

Zusammenfassung

Theoretische Modellierungen von laserinduzierten Zinnplasmen ergaben kürzlich, dass Übergänge zwischen mehrfach angeregten Zuständen einen größeren Anteil am, für Nanolithografie relevanten, EUV(extreme ultraviolet)-Spektrum haben als zuvor angenommen. Experimentelle Daten, die Linienstärken für verschiedene Grade an Anregungen dokumentieren, stehen aus, um diese Aussage zu überprüfen. Um solche Messungen durchzuführen, wurden hochgeladene Zinnionen mehrerer, ausgewählter Ladungszustände (Sn^{11+}-Sn^{15+}) mithilfe einer Elektronenstrahl-Ionenfalle (EBIT) erzeugt und mit Elektronen variabler Energie in kurzen Scans mit einer Dauer von bis zu 200 ms in Kontakt gebracht. Die EUV-Strahlung wird durch den Zerfall von, durch Stoßanregung produzierter, angeregter Zustände erzeugt, aufgenommen, und mit der Elektronenstrahlenergie während des Scans in Verbindung gebracht. Projektionen der Intensität der so aufgenommenen Spektrallinien auf die Elektronenstrahlenergie erlauben die Bestimmung relativer Wirkungsquerschnitte der Elektronenstoßanregung. Fits mit mehreren Van Regemorter-Funktionen erlaubten die Extraktion von zusätzlichen Energieschwellen für die Emission von EUV-Licht, um so die Beiträge von mehrfach angeregten Zuständen zum Spektrum von hochgeladenem Zinn zu bestimmen.

Contents

Chapter 1

Introduction

For many decades an important driver for technological innovation and economic growth on a global scale has been the miniaturization of circuits and therefore the increase in available computing power. As computer chips play a vital role in virtually every aspect of modern industry, and material footprint as well as cost of chips are both inversely proportional to the density of transistors on them, increasing this density has been an important driver for continued economic growth [31]. From the first chips entering mass production, which contained transistors of sizes in the range of 10 μm, modern chips have reached transistor sizes in the range of 10 nm, often in multiple layers to increase the transistor density even further.

This miniaturization has been following an empiric trend, the so called "Moore's Law" [73], predicting a doubling in circuit density on computer chips every one to two years [74]. This law has continued to describe the industrial reality for many years successfully, more or less becoming a self-fulfilling prophecy.

Recently, physical limits have raised the question whether Moore's law would continue to reflect the reality deeper into the 21st century [106]. If this exponential trend continued, feature sizes on integrated circuits would become so small, only a couple of atoms large, that they become dysfunctional due to the nature of quantum mechanics. Insulating layers inside of transistors would become conducting due to electron tunnelling, rendering the fundamental elements of integrated circuits unreliable and hence useless [83].

But even before those fundamental problems come to fruition, other problems would arise, as was well known already in the late 90s [77]. One of those problems regards the practical manufacturing process of chips with nanometer-scale features, since imprinting ever smaller features on silicon wafers poses significant challenges [109].

Indeed, in recent times, technical limits in the context of imprinting those features are being reached. Circuits have become small enough, that the previously used methods of producing chips needed to be replaced with entirely new ideas. One of the most widely employed methods for imprinting features on silicon wafers is called photolithography [102]. Different variations exist, but all of them rely on the following scheme. The semiconducting plate, supposed to become the chip, is covered with a photoresistive layer. On top of that, a light absorbing mask is positioned. Ultraviolet light, most commonly produced by laser or plasma sources, is then impinged on the photoresistor. The exposure of the substrate is limited to positions as given by the absorbing mask. Following this illumination, a chemical substance is introduced to remove the photoresistor in illuminated locations, leaving the wafer below exposed. This bare wafer is then chemically etched to produce the conducting pathways and hence imprint the desired features on the chip.

To produce chips with ever increasing circuit densities, it is necessary to decrease the wavelength of the used light source, as for the critical distance r_{crit}, the smallest possible distance to be resolved on the wafer by the means of photolithography, the proportionality

$$r_{\text{crit}} \propto \lambda$$

holds as a result of the Rayleigh criterion [111]. This means that the formerly most widely employed sources, based on ArF-excimerlasers [26] with a wavelength of 194.3 nm needed to be replaced by light sources of lower wavelength. This demand for light sources of a shorter wavelength, led to a new technology entering mass production, EUV-lithography. Instead of the formerly employed laser source, plasmas are now used to generate high-energy photons in the 13.5 nm-band, a wavelength determined by the most efficient multilayer-optics in the EUV-regime [29] [49]. Inside of these high temperature plasmas, electronic transitions take place in the ions making up the plasma, producing the characteristic photons determined by the energetic structure of the particular ions.

Nowadays, laser-produced tin-plasmas are commonly used in nanolithography, as with them a high conversion efficiency (meaning fraction of input energy converted to EUV-photons) can be reached [114]. The functioning principle of an EUV-source employing a laser-produced tin plasma is for example described in [113] and [1]. Small droplets of tin are inserted into a vacuum chamber. A first laser pulse hits the droplet to flatten it into a pancake-like shape and allow a second laser pulse to convert the liquid into a cloud of plasma of high surface area. This plasma, containing a wealth of different tin charge states, then emits the desired 13.5 nm-radiation for the lithographic application. The emitted light gets collected by a collector mirror and focused onto a set of mirrors. Those multilayer mirrors then transport the light towards the wafer which is to be imprinted with the desired features.

Such sources have been developed and optimized for many years now, and find application in many production facilities all around the world. However, the physical properties of the tin-plasma supplying the EUV-light are far from completely understood [96]. This is due to the complicated atomic structure of the tin ions in the plasma. The tin charge states radiating strongly in the 13.5 nm are Sn^{11+} - Sn^{14+} [92]. With a nuclear charge of $Z = 50$ in the case of tin, these charge states still contain many interacting shell electrons in the $n = 4$-shell, partaking in the transitions resulting in the EUV-light.

Recent theoretical studies have led to the question, if the most commonly regarded transitions in the plasma, transitions from singly-excited states to the ground state, are actually the states which contribute the most to emissions in the relevant wavelength range, or if multiply excited states play a more important role than previously thought [108], [97].

In this thesis, laboratory experiments are conducted, to answer open questions on the prevalence of emissions between the different multiply excited states. By

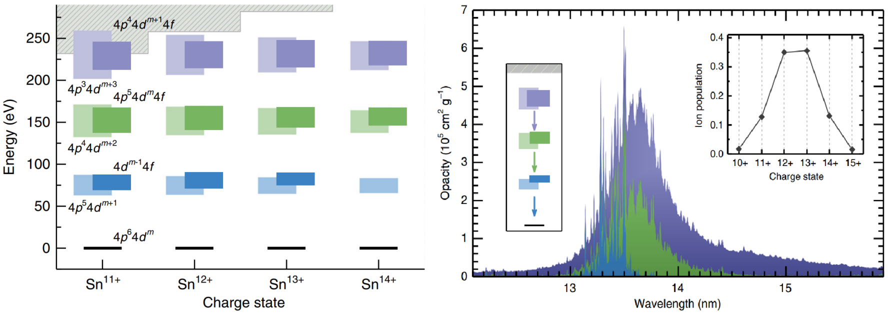

Figure 1.1: Visualized level structure and opacity spectrum resulting from transition between the different blocks of energy levels in a laser-produced tin-plasma, calculated in and taken from [108]. There prominent contributions of multiply excited states to the opacity of laser-produced tin plasmas were found.

employing an electron beam ion trap (EBIT) atomic tin is multiply ionized. By choosing several different experimental settings, several charge states of interest between Sn^{11+} and Sn^{15+} are produced and trapped. By bringing these ions into contact with electrons of various, well-defined energies from 90 eV to 500 eV and observing the resulting EUV-spectra at each electron energy with high resolution, the atomic structure of the ions is investigated.

The precise definition of the electron energy allows a selection of the available excited states in the tin plasma. As electron impact excitation is the main driver of excited state populations in the observed plasma, ideally only electronic states with an energy below the kinetic energy of the free electrons may be produced. This way one could observe the spectra emitted from singly excited states as well as from multiply excited states separately, to answer, whether transitions from multiply excited states indeed play a leading role in the generation of the EUV-light.

Additionally, this variation of the electron energy with simultaneous collection of the emitted EUV-light, all while keeping electron and ion densities in the trap constant, allows for direct measurements of the relative electron collisional excitation cross sections, which may give further answers on the energetic structure of the investigated tin ions and the relative strengths of the different possible transitions.

Comparisons to calculations allow tests of the models on the experimental results, to see whether theory can be reliably used to predict further properties of additional charge states not investigated in this thesis, as well as to obtain the electronic states responsible for the emission spectrum.

In the following, first a short overview over the theoretical foundations governing the emergence of atomic spectra, as observed in this work, is given. Ways to calculate energy levels in atomic systems of varying complexity are shown and the various types of possible transitions between those levels are described. Afterwards a description of the experimental apparatus FLASH-EBIT with its different components is given. There also the employed measurement scheme, designed to systematically determine the electronic states contributing to the spectrum of highly charged tin in laser produced plasmas, is explained. Afterwards the experimental results are shown, together with the various steps undertaken in the data analysis to determine the contribution of the multiply excited states in question. In the end these results are discussed and the properties of highly charged tin which were discovered compared to theoretical predictions, closed with an outlook on how to continue the systematic examination of the atomic structure of highly charged tin.

Chapter 2

Theory

Radiation sources in modern nanolithography are based on the emissions of laser-produced tin plasmas. But what is it, that makes these plasmas emit light with their characteristic spectrum?

Generally, plasmas are made up of positive, often highly charged ions and free electrons. Crucial for the spectral properties of this type of matter is the emission of each individual ion making up the plasma, as interactions between the individual particles is weak, as contrary to a liquid or a solid [89].

Ever since Fraunhofer's studies of the solar spectrum in the 19th century [33], the fact that elements radiate light of specific wavelengths has been known. As was found out by Bohr 1913, [13] these characteristic spectral lines are the result of transitions of electrons between the different possible orbits they are allowed to occupy in the individual atoms' shells. This picture of orbiting electrons has been refined since, with the formulation of quantum mechanics and quantum electrodynamics, but the intuitive understanding of the origins of radiation emitted by atoms and ions stayed the same. Changes between distinct energetic levels, the electrons can occupy in the atomic shell, lead to the emission of a photon with an energy of exactly that energy difference. Therefore the light emitted by such an atomic system may be used as a direct probe for its underlying energetic structure. Using this connection, the structure of the industrially interesting tin ions, Sn^{11+} up to Sn^{15+}, is to be observed in this work. Of special interest is the question, which energetic states prominently contribute to the extreme ultraviolet spectrum. Therefore an experimental scheme is developed to selectively elevate electrons into specific states to observe radiation originating from the decay of those states.

In order to understand the following experiment, some theoretical basics on atomic physics have to be covered.

As this light is the result of transitions between the discrete energy levels of electrons populating the shells of ions trapped inside the experimental apparatus, it is crucial to understand how the different energy levels emerge and how they are populated, including a description of the energetic ordering of these levels. The mechanisms governing the transitions of electrons between those energy levels need to be described, including the transitions leading to the emissions of photons making up the observed signals.

Starting with a description of the simple one electron system of hydrogen, as it has the only analytically solvable atomic structure [22], we work our way towards the more complex systems of the highly charged tin ions covered in this work. Continuing with methods on how to calculate these energetic levels theoretically, we end up with a description of the different transitions observed and discuss their properties. These include excitation processes driven in the plasma inside the EBIT and radiative de-excitation processes, together providing a probe to extract the energetic structure of the trapped ions.

2.1 Hydrogen Atom

In a first step, it is instructive to discuss the hydrogen atom, the simplest atomic system with only one electron, making it the only atomic system with an analytically solvable electronic structure, before going on to describe more complex systems.

In order to understand the quantum mechanical structure of the electronic shell of an atom, the electron wavefunctions $\Psi(\vec{r}, t)$ have to be calculated. Their squared value $|\Psi(\vec{r}, t)|^2$ gives a spatial probability for where to find the particle at a given time [22]. As will be seen below, the averaged distance from the nucleus will play a large role in defining the energetic level of the electron, defining the structure of the atom, making this wavefunction the central quantity to be understood.

2.1.1 Classical Solution and Corrections

A starting point for finding the electron wavefunctions is the Schrödinger equation [7], which describes the temporal evolution of $\Psi(\vec{r})$:

$$\hat{H}\Psi(\vec{r}, t) = \frac{\partial}{\partial t}\Psi(\vec{r}, t) \tag{2.1}$$

The hamilton operator $\hat{H}$ introduced here describes the energy of a quantum mechanical system. A solution for this problem is for example given in [22], on which this section orients on. For the calculation of the electron wavefunction, a suitable hamiltonian for the electron surrounding the nucleus needs to be defined. This hamilton operator $\hat{H}$, can be split up into an kinetic term, potential term and an interaction term for the case of the hydrogen atom at hand:

$$\hat{H}_{\text{tot}} = \hat{H}_{\text{kin}} + \hat{H}_{\text{pot}} + \hat{H}_{\text{int}} \tag{2.2}$$

These individual terms are now to be specified.
The kinetic term of the hamiltonian in the presented case is

$$\hat{H}_{\text{kin}} = -\frac{\hbar^2}{2m}\vec{\nabla}_r - \frac{\hbar^2}{2M}\vec{\nabla}_R \tag{2.3}$$

with the location vectors $\vec{r}$ for the electron and $\vec{R}$ for the nucleus. m and M describe the masses of the electron and the nucleus respectively. ∇_i describes the derivative of one of the coordinate vectors $\vec{r_i}$ along the three spatial coordinates

$$\vec{\nabla}_i = \left(\frac{\partial \vec{r_i}}{\partial r_1}, \frac{\partial \vec{r_i}}{\partial r_2}, \frac{\partial \vec{r_i}}{\partial r_3} \right)$$

The motion of the atom as a whole, including the nucleus, can be coupled-out as a center-of-mass motion. Hence it is sufficient to only describe the relative motion of the electron here, in order to obtain the inner energetic structure. From here on out, $\vec{r}$ describes the location of the electron relative to the nucleus. Then the kinetic term can be rewritten using the momentum operator $\hat{p} = -i\hbar\nabla$ as

$$\hat{H}_{\text{kin}} = \frac{\hat{p}^2}{2\mu} = -\frac{\hbar}{2\mu}\Delta_r \tag{2.4}$$

with μ being the reduced mass $\frac{mM}{m+M}$, which is approximately m, as the mass of the nucleus is much higher than that of the electron. The Laplace operator Δ_r is defined as $\vec{\nabla}_r^{\,2}$ for the location of the electron.
The potential term is given by the central coulomb potential of the nucleus:

$$\hat{H}_{\text{pot}} = -\frac{Ze^2}{4\pi\epsilon_0|\vec{r}|} \tag{2.5}$$

with the nuclear charge Z, which is 1 in the case of the hydrogen atom. In this simplest case, the interaction hamiltonian $\hat{H}_{\text{int}}$ can be left out, as there is only one electron in the system. This interaction term will be reintroduced in the following section.
With the hamiltonian defined, one can insert it back into the Schrödinger equation 2.1. This results in an analytically solvable set of differential equations, as one can seperate the radial and angular parts of the equation. After a rather lengthy calculation, for example presented in [22], one arrives at the seperated wavefunction

$$\Psi(\vec{r}, t) = R_{nl}(r) Y_{lm}(\Theta, \Phi) \tag{2.6}$$

made up of the radial wave function $R_{nl}(r)$ and the angular part $Y_{lm}(\Theta, \Phi)$, which are the spherical harmonics [75]. The radial part of the wavefunction, can be written as

$$R_{nl}(r) = D_{nl} e^{-}\frac{Zr}{na_0} \left(\frac{2Zr}{na_0} \right)^l L_{n+l}^{2l+1} \left(\frac{2Zr}{na_0} \right) \tag{2.7}$$

with the Laguerre polynomials L_{n+l}^{2l+1}, a normalization constant D_{nl} and the Bohr radius a_0.
The indices n, l and m further define which solution for the differential equation 2.1 the wavefunction is, as there is an infinite set of possible solutions.
These indices, known as quantum numbers, also bear significant physical meaning. n, known as the main quantum number has generally the largest influence on the energy of a shell electron, as seen below in equation 2.11, and on the average distance of the electron from the nucleus. l is known as the orbital angular momentum quantum number, as the orbital angular momentum of the

electron can be obtained from it via the relation [22]

$$L^2\Psi = \hbar l(l+1)\Psi \tag{2.8}$$

with the orbital angular momentum operator L and the reduced Planck's constant $\hbar$. m is the magnetic quantum number, defining the magnitude of the angular momentum in one specified spatial direction z

$$L_z\Psi = \hbar m\Psi \tag{2.9}$$

Now the energy eigenvalues for the hydrogen atom can be calculated by inserting the obtained wavefunction 2.6 into the stationary Schrödinger equation

$$\hat{H}\Psi(\vec{r},t) = E\Psi(\vec{r},t) \tag{2.10}$$

Solving this eigenvalue equation with known $\hat{H}$ and Ψ, the energy eigenvalues are calculated as

$$E = -\frac{\mu e^4 Z^2}{8\epsilon_0^2 h^2 n^2} = -\frac{Z^2}{n^2}Ry \tag{2.11}$$

where the Rydberg energy Ry is approximately 13.6 eV, n denotes the principal quantum number and Z the nuclear charge. Note the negative value of the energies here, as the electrons are bound to the nucleus, with higher negative values meaning a stronger binding. One can see, that the energy of the state is only dependant on the principal quantum number n in this first approximation, while being degenerate in terms of the angular momentum quantum number l and the magnetic quantum number m.

However, the energetic values for the different atomic states calculated this way are not exact. This can for example immediately be seen by the fact, that the calculation so far has been classical and not relativistic, using the kinetic energy term 2.4 from above.

So, in a first step to refine these energy values, one can expand this classical kinetic energy term. A completely correct solution would contain the relativistic energy term

$$H_{\text{kin}} = \sqrt{p^2c^2 + m^2c^4} - mc^2 \tag{2.12}$$

where c is the speed of light.

By expanding this kinetic energy term for small kinetic energies (meaning the rest mass of the electron (511 keV) is much higher than the kinetic energy), one gets an approximate result of

$$H_{\text{kin}} \approx \frac{p^2}{2m} - \frac{p^4}{8m^3c^2} \tag{2.13}$$

where the first term recovers the classical kinetic energy from equation 2.4 and the second term is the first order relativistic correction. By applying perturbation theory with this first order correction as a perturbation, one can extract

[32] a correction of the energy eigenvalues of

$$E_{\text{rel}} - E := \Delta E_{\text{rel}} = -E\frac{Z^2\alpha^2}{n}\left(\frac{3}{4n} - \frac{1}{l+\frac{1}{2}}\right) \tag{2.14}$$

with the classical energy eigenvalue E from equation 2.11 and the fine structure constant $\alpha \approx \frac{e^2}{4\pi\epsilon_0\hbar c} \approx \frac{1}{137}$ [51]. This corrective term for the energy depends on the angular momentum quantum number l of the electron, and thus lifts the degeneracy of the energy for levels with the same n but different l, with energies of electrons with high angular momentum l having higher eigenenergies. As this energy correction is proportional to the fine structure constant squared,

$$\Delta E_{\text{rel}} \propto Z^2\alpha^2 \approx \left(\frac{Z}{137}\right)^2$$

the correction is usually small, except for hydrogenic systems with a very high nuclear charge. So one speaks of fine structure, as opposed to the gross structure determined by the principal quantum number n.

Another term contributing to this fine structure stems from the fact that the electron is a fermion, meaning a particle with an inherent spin of $\frac{1}{2}$. This circumstance leads to further splitting of the energy levels. The reason for that can be seen by taking the point of view of an electron orbiting the nucleus. In a frame of reference where the electron is at rest, the nucleus orbits the electron, giving rise to a ring current and thus generating a magnetic field $\vec{B}$. Analogous to the classical Zeeman effect [119], which leads to the modification of energy levels due to the coupling of the electron orbital angular momentum to an external magnetic field [22], this magnetic field may now interact with the intrinsic magnetic moment of the electron which is a result of its spin, $\vec{\mu_s}$. This effect is called spin-orbit coupling [11] and leads to the corrective term in the hamiltonian of

$$H_{\text{spin-orbit}} = \left(\frac{Ze^2}{4\pi\epsilon_0}\right)\left(\frac{g_s - 1}{2m^2c^2}\right)\frac{\vec{L}\cdot\vec{S}}{r^3} \tag{2.15}$$

with the electron orbital angular momentum $\vec{L}$, spin angular momentum $\vec{S}$ and spin g-factor g_s [82]. This additional term in the hamiltonian results in the eigenenergies needing to be corrected by [22]

$$\Delta E_{\text{spin-orbit}} = -E_n\frac{Z^2\alpha^2}{2nl(l+1)}(j(j+1) - l(l+1) - s(s+1)) \tag{2.16}$$

depending on the electronic energy level defined by the principal quantum number n as obtained via equation 2.11. Here the newly introduced quantum number j is a measure for the total angular momentum of the electron $\left|\vec{j}\right| = \sqrt{j(j+1)}\hbar$ [32] with the allowed values of j being $l + \frac{1}{2}$ and $l - \frac{1}{2}$. This total angular momentum is a result of the coupling of spin and orbital angular momentum of the electron. Due to the proportionality $E_n \propto Z^2$, this energy correction scales with

$$\Delta E_{\text{spin-orbit}} \propto \alpha^2 Z^4$$

and therefore usually again equates to only a minor energy shift, except for ions of a very high nuclear charge.

Another relevant correction to the electronic energy levels is given by the fact, that the exact location of the electron at any given time can not be obtained to its nature as a wave-packet. This gives rise to the Darwin-term [22], resulting in the additional energy correction of

$$\Delta E_{\text{Darwin}} = 4Z^4 m_e c^2 \alpha^4 \propto Z^4 \alpha^4 \tag{2.17}$$

even smaller than the corrections presented before.
Additional corrections to the energy values exist, such as the Lamb shift [50], consisting of the self-energy of the electron, vacuum polarisation effects and the anomalous magnetic moment of the electron. These corrections lead to even smaller energy splittings and are thus not described here further, as the energy contributions discussed so far define the ordering of the different energy levels for the most part.

2.1.2 Exact Solution

Even after employing the several corrections in the preceding section, the obtained energies of the hydrogen levels are not exact. A more complete calculation of the energies involves the Dirac equation instead of the Schrödinger equation. This treatment then also includes all relativistic effects and is for example described in [34], on which this section orients on.
The Dirac equation [57] involves treating the wavefunction Ψ as a 4-dimensional bispinor. The hamiltonian gets replaced by a 4x4 matrix, which can be written as

$$H_D = \begin{pmatrix} mc^2 \mathbb{1} & c(\vec{\sigma} \cdot \vec{p}) \\ c(\vec{\sigma} \cdot \vec{p}) & -mc^2 \mathbb{1} \end{pmatrix} - \frac{Ze^2}{r} \tag{2.18}$$

with the coloumb potential of the nucleus $V(r) = -\frac{Ze^2}{r}$. Here each entry represents a 2x2 matrix as $\vec{\sigma}$ describes the usual pauli matrices [115], $\vec{p}$ the momentum vector of the particle and $\mathbb{1}$ the 2-identity matrix. By inserting this new hamiltonian into the dirac equation [57]

$$i\hbar \frac{\partial \Psi}{\partial t} = H_D \Psi \tag{2.19}$$

one obtains the Dirac wavefunctions. Again, for the central potential of the hydrogen atom one gets an analytical result for the electron wavefunction:

$$\Psi = \begin{pmatrix} \frac{P_{n\kappa}(r)}{r} \\ i\frac{Q_{n\kappa}(r)}{r} \end{pmatrix} Y_{lm}(\Theta, \Phi) \chi_\nu(s) \tag{2.20}$$

using the radial functions $P_{n\kappa}$ $Q_{n\kappa}$, the spherical harmonics as above and the spin wave functions χ, as spin is implicitly included [34] in the full relativistic treatment the Dirac equation provides.
Again, as in the previous, non-relativistic case, the wavefunctions can be used

to then calculate the corresponding atomic energy levels with

$$E_{jn}\Psi = H_D\Psi \rightarrow E_{jn} = \mu c^2 \left(1 + \left[\frac{Z\alpha}{n - |j+\frac{1}{2}| \sqrt{(j+\frac{1}{2})^2 - Z^2\alpha^2}}\right]^2\right)^{-1/2} \tag{2.21}$$

The resulting energy equation is also known as the ”Sommerfeld formula” [69]. Now the energy E_{jn} is dependant on the principal quantum number n, as well as on the total angular momentum of the electron j, which is the vector sum of the spatial angular momentum l and the spin angular momentum s. $\alpha \approx \frac{1}{137}$ denotes the fine structure constant and c the speed of light.

In addition to the classical energy contribution from the coulomb field, the Sommerfeld formula takes into account relativistic effects due to being a result of the calculations using the Dirac equation.

In addition to these relativistic effects, to get the complete result, one needs to add several quantum electrodynamical (QED) effects like the already mentioned Lamb shift [50]. These additional energy contributions then also lift the degeneracy of energy levels in regards to the orbital momentum quantum number l of the electron again.

2.2 Multi Electron Systems

Now that a model to obtain electron wave functions and electron energies for an atom with a single electron has been described, an approach towards systems with many electrons, as studied for the example of tin in the following experiment, has to be made.

As mentioned beforehand, the hydrogen atom with its single electron is the only analytically solvable atomic system. Adding further particles to the system provides the need to calculate the structure numerically.

The simplest multi-electron system consists of a nucleus and two accompanying electrons, the helium atom. In order not to convolute the explanation, here the non-relativistic case is assumed. Thus, to get the hamiltonian for this system, we first insert equation 2.4 and 2.5 as the single electron terms into the total hamiltonian from equation 2.2 for both electrons seperately:

$$H_{12}(\vec{r_1}, \vec{r_2}) = \sum_{i=1,2} \left(-\frac{\hbar}{2m}\Delta_{r_i} - \frac{Ze^2}{4\pi\epsilon_0|\vec{r_i}|}\right) \tag{2.22}$$

Here and in the following $\vec{r_i}$ describes the location vector of electron i.

What is missing now is a third term in the total hamiltonian, describing the interaction between the two electrons present in the atomic shell. This interaction arises due to the coulomb repulsion between the two electrons and can thus be formulated as

$$H_{\text{int}}(r_{12}) = \frac{e^2}{4\pi\epsilon_0 r_{12}} \tag{2.23}$$

with $r_{12} = |\vec{r_1} - \vec{r_2}|$ being the absolute distance between the electrons. Combining all three terms, while summing over the electrons of the system, the total hamiltonian becomes

$$H_{\mathrm{He}}(\vec{r_1}, \vec{r_2}) = \sum_{i=1,2} \left(-\frac{\hbar}{2m} \Delta_{r_i} - \frac{Ze^2}{4\pi\epsilon_0 |\vec{r_i}|} \right) + \frac{e^2}{4\pi\epsilon_0 r_{12}} \tag{2.24}$$

As an analytical solution is not possible anymore, one needs to simplify the problem. Instead of treating the problem as a system of multiple particles, each interacting with one another, one can reduce it to a series of one-particle problems, where the other electron only contributes by shielding the nuclear charge, thus reducing the coulomb interaction and lowering the binding energy.
In a first simple approximation, one could imply full shielding of the nucleus by the other electron. As an example, for the helium atom, this results in the problem being again reduced to the hydrogen problem, with the same resulting wavefunctions and energy levels. Improved approaches work iteratively to produce a realistic shielding effect.
In the following such methods are described. As they are also valid for any number of electrons in the system, and not only for the helium atom, the general case for n electrons will immediately be described.

2.2.1 Hartree Methods

One very common algorithm to calculate the energy level of each electron in a multi-electron-system is the Hartree method [30].
In a first step to calculate the energy eigenstate of one single electron i in the shell, one assumes a certain potential V_0, consisting of the nuclear coulomb field and the shielding of all the other electrons. As an assumption full or no shielding might be used.
This potential is then inserted into the Schrödinger equation 2.1 together with the kinetic energy term of the electron. Solving the Schrödinger equation analogously to the hydrogen problem then yields a wave function $\Psi_0(\vec{r_i}, t_i)$. This process is repeated for all electrons in the shell, yielding an initial approximation for the wave function for each of them.
As the wavefunction of a particle directly connects to its spatial probability distribution,

$$\rho(\vec{r_i}, t_i) = |\Psi(\vec{r_i}, t_i)|^2 \tag{2.25}$$

this wavefunction can then be used to calculate a value of the shielding effect by the electron for all the other electrons.
This spatial probability is calculated for each electron from the first iteration step, thus yielding a total shielding of the nuclear charge to be inserted as a new potential in a next iteration step:

$$V_1(r_i) = -\frac{e}{4\pi\epsilon_0} \left(\frac{Z}{r_i} - \sum_{j \neq i} \int \frac{\rho}{r_{ij}} \right) \tag{2.26}$$

With the potential of the multi-particle problem now approximated and the situation thus reduced to a one-electron problem, the Schrödinger equation can be solved once more to obtain another set of wavefunctions for each electron $\Psi_1(\vec{r_i}, t_i)$. Now, iteratively, again, a new set of potentials may be calculated from these wavefunctions to further refine the next set of wavefunctions. This is done repeatedly, until the solutions converge, meaning the next set of wavefunctions, and corresponding eigenenergies, are within a set boundary to the ones calculated in the prior step.

Now, in order to compile all of these single-electron wavefunctions into one multi-electron-wavefunction, one can not simply add all of them up. Although, as the Schrödinger equation is a linear equation and thus a sum would again be a solution, the Pauli principle forbids this method of addition [22].
The Pauli principle [79] states that, for each fermion, meaning spin-$\frac{1}{2}$-particle, which includes the electron, a multi-particle wavefunction has to be antisymmetric under the exchange of two particles.
A natural way, to make sure this condition is fulfilled when combining many single-particle functions is the Slater-determinant [100], here for n electrons:

$$\Psi_{tot}(\vec{r_1}, t_1, ..., \vec{r_1}, t_1) = \frac{1}{\sqrt{N!}} \begin{vmatrix} \Psi_1(\vec{r_1}, t_1) & \Psi_2(\vec{r_1}, t_1) & ... & \Psi_n(\vec{r_1}, t_1) \\ \Psi_1(\vec{r_2}, t_2) & \Psi_2(\vec{r_2}, t_2) & ... & \Psi_n(\vec{r_2}, t_2) \\ ... & ... & ... & ... \\ \Psi_1(\vec{r_n}, t_n) & \Psi_2(\vec{r_n}, t_n) & ... & \Psi_n(\vec{r_n}, t_n) \end{vmatrix} \tag{2.27}$$

The index i of the wavefunctions inside the determinant denotes single electron wavefunctions, calculated using the Hartree method described above.
Only taking into account the spatial wavefunction of an electron does not present the complete information about the particle. Again, the spin wavefunction χ has to be introduced into the slater determinant [22]:

$$\Psi_{\text{tot}}(\vec{r_1}, t_1, ..., \vec{r_n}, t_n) = \frac{1}{\sqrt{N!}} \begin{vmatrix} \Phi_1(\vec{r_1}, t_1)\chi_1(1) & \Phi_2(\vec{r_1}, t_1)\chi_2(1) & ... & \Phi_n(\vec{r_1}, t_1)\chi_n(1) \\ \Phi_1(\vec{r_2}, t_2)\chi_1(2) & \Phi_2(\vec{r_2}, t_2)\chi_2(2) & ... & \Phi_n(\vec{r_2}, t_2)\chi_n(2) \\ ... & ... & ... & ... \\ \Phi_1(\vec{r_n}, t_n)\chi_1(n) & \Phi_2(\vec{r_n}, t_n)\chi_2(n) & ... & \Phi_n(\vec{r_n}, t_n)\chi_n(n) \end{vmatrix} \tag{2.28}$$

where $\phi_i(\vec{r_j}, t_j)$ describe the spatial wavefunctions and $\chi_i(j)$ the spin wavefunctions for electron j. This inclusion of the spin wavefunctions extends the Hartree method to the Hartree-Fock method.

2.2.2 Configuration Interaction

More sophisticated algorithms for the numerical solution of multi-electron wavefunctions than the Hartree-Fock method exist. One example for such a method is configuration interaction (CI) [98], as used in the flexible atomic code (FAC) [39], employed in this work. The Configuration interaction (CI) takes into account many different slater determinants. So far, in the Hartree methods described, the influence of the electrons on each other was only taken into account as a time averaged potential shielding. The correlation between electrons however was neglected, and can be approximated using CI [95].
One builds up a new wavefunction from several configurations. One configuration Ψ_i describes one possible distribution of the electrons on the atomic orbitals with corresponding angular momentum coupling,

$$\Psi_{\text{CI}}(\vec{r_1}, t_1, ..., \vec{r_n}, t_n) = \sum_i c_i \Psi_i(\vec{r_1}, t_1, ..., \vec{r_n}, t_n) \tag{2.29}$$

The wavefunction Ψ_i of such a configuration can be obtained with the aforementioned Hartree-Fock method. The individual weights of the configurations, c_i are obtained by diagonalizing the total hamiltonian of the system, which reads as an extension of equation 2.24 for the case of n electrons (for simplicity now in atomic units) [39]:

$$H = \sum_{i=1}^{N} H_D(i) + \sum_{i<j}^{N} \frac{1}{r_{ij}} \tag{2.30}$$

With these new wavefunctions, also products of different configurations appear when calculating the energy of a given state:

$$E = \langle \Psi_{\mathrm{CI}} | H | \Psi_{\mathrm{CI}} \rangle = \left(\sum_i c_i \langle \Psi_i | \right) E \left(\sum_j c_j | \Psi_j \rangle \right) = \sum_{i,j} c_i c_j \langle \Psi_i | E | \Psi_j \rangle \tag{2.31}$$

leading to the more accurate results.

Theoretically, one can obtain exact results for atomic energy states, even for multi-electron systems from CI, if one would include all possible configurations in the calculation. As this is not possible, as the dimension of the hamiltonian, which needs to be diagonalized to obtain the state coefficients c_i, scales exponentially with the number of included states, one needs to balance accuracy against computation time with this approach.

2.2.3 Level Notation and Angular Momentum Coupling

Now that it is established, how to calculate the potential energy for a bound electron in an atomic shell, the filling of these energetic levels will be discussed, including rules governing the ordering of the energy levels depending on the values of the quantum numbers of each electronic state.

As an overview, each electron in an atomic shell possesses the following quantum numbers, determining the state it is in and the energy of the state as presented in equation 2.21:

Table 2.1: Quantum numbers describing the properties of electrons inside the atomic shell.

Quantum number	Symbol	Possible values
Principal	n	1,2,3,...
Orbital angular momentum	l	1,2,3,..,n
Magnetic	m_l	-l,...,-1,0,1,...l
Spin	m_s	$-\frac{1}{2}$, $\frac{1}{2}$
Total angular momentum	j	$\lvert l-s\rvert$,$\lvert l-s\rvert+1$,...,$l+s-1$,$l+s$
Angular momentum projection	m_j	$-j$, ..., $+j$

Using these quantum numbers and the methods described in this section, one can calculate approximate energies for each electronic state of the atomic shell.

This leads to two principles in building up an electronic shell with multiple electrons. The first being the fact, that the ground state of any atom, is the state with the minimally possible energy. Secondly, the filling of the energy levels adheres to the Pauli principle [2], stating, that no two electrons may be in the same location and the same state, defined by their quantum numbers. This prevents all electrons in the ground state of the atom to condense into the lowest lying energy state. Instead, only $2n^2$ electrons may fit into each shell, as defined by the principal quantum number n, and $2l + 1$ electrons into each subshell, as defined by the orbital angular momentum quantum number l. Thus one subshell after another is being filled, according to their energetic ordering. With these two principles in place, valid electronic configurations for ground states may be defined.

To preserve the relevant information of an electronic level in the following discussions, specific symbols are used when naming an electronic level. These symbols are defined as

$$nl_j \tag{2.32}$$

Here l is given in terms of a letter, representing the orbital angular momentum, with $s, p, d, f, g, ...$ correlating to $0, 1, 2, 3, 4, ...$ Regarding nomenclature, electrons of the same principal quantum number are said to be part of the same shell, which can also be labeled with a letter, relating $K, L, M, N, O, P, ...$ to $n = 1, 2, 3, 4, 5, 6, ...$

One example for a level symbol would be given by the configuration of a valence electron (meaning electron in the outer most shell) for the groundstate of the observed Sn^{15+}:

$$4s_{1/2} \tag{2.33}$$

meaning the electron is in a state with a principal quantum number of 4, an orbital angular momentum of 0 and a total angular momentum of 1/2.

In the case of multiple electrons in the atomic shell, as is the case for the ions investigated in this work, the definition of level symbols has to accommodate those multiple electrons and their couplings to each other.

First of all, a useful information, which is given later multiple times, is the distribution of the shell electrons on the available subshells, defined by their principal quantum number n and orbital angular momentum l. As an example for the case of the groundstate of Sn^{13+}, omitting the electrons in the shells up to the M-shell ($n = 3$), as they are completely filled, one obtains

4s2 4p6 4d1

Now one has to keep in mind, that in the case of multiple electrons the angular momenta of the different electrons couple to each other in order to define a total angular momentum J for a specific level. This total angular momentum is a critical piece of information when trying to gauge the energy of a given level, as different couplings of individual angular momenta result in different level energies. Two approximate coupling schemes exist, LS-coupling [23] and jj-coupling [90], to obtain the total angular momentum from the momenta of the singular electrons. LS-coupling is the limiting case for light atoms, for which the coupling of the orbital angular momenta and spin angular momenta of different electrons couple to each other more strongly than the orbital and spin angular momentum of the individual electrons. jj-coupling is the limiting case for heavy atoms, where the momenta of the individual electrons are coupled more strongly. In tin, jj-coupling is prevalent, which warrants an explanation of the level symbols used there.

As a short remark, to avoid confusion, it has to be mentioned that there are three different ways to specify an electronic configuration of an atom. When talking about a term, a configuration with a specific value for the total orbital angular momentum L and the total spin angular momentum S is given. Such a term can be further specified by its total angular momentum J as a level, where for each term $(2S+1)(2L+1)$ possible levels arise. By then defining the projection of the total angular momentum, M_J, a unique state is defined. Again, each yields $2J+1$ possible states, due to the possible values of M_J ranging from $-J$ to $+J$. Here, configurations are usually defined as levels, due to the prevalent form of angular momentum coupling discussed below.

In the case of jj-coupling first a total angular momentum for each individual electron is defined as above, via the vectorial sum

$$\vec{j} = \vec{l} + \vec{s}$$

Then these total angular momenta of the individual electrons i couple to each other again, via a vectorial sum, to a total angular momentum of the level

$$\vec{J} = \sum_i \vec{j}_i$$

This coupling is strongest among electrons in the same subshell, meaning with the same n and l, which is why they couple first to define a total angular momentum of that subshell. Using the nomenclature of [59], for example one gets for the groundstate of Sn^{13+} the level symbol

$$([4\mathrm{d}-]^{1}_{\frac{3}{2}})_{\frac{3}{2}}$$

Here every closed shell is omitted and only valence electrons displayed. This level symbol means that one electron populates the 4d-shell, with downwards spin. The spin and orbital angular momenta of this electron couple to $j_{4d-} = \frac{3}{2}$. If there are several populated, not completely filled subshells, their total angular momenta can couple again to a total angular momentum of the state. In this case, with only one, not completely filled subshell, the total angular momentum is again $j_{\mathrm{tot}} = j_{4d-} = \frac{3}{2}$. One more complicated example would be an excited state of Sn^{13+} identified as a metastable state later in section 5:

$$([4\mathrm{p}+]^{3}_{\frac{3}{2}}[4\mathrm{d}-]^{1}_{\frac{3}{2}}[4\mathrm{d}+]^{1}_{\frac{5}{2}})_{\frac{11}{2}}$$

Now, three spin up electrons populate the 4p-shell, meaning it is not completely filled, 1 spin-down electron the 4d-shell and 1 spin up electron 4d-shell. The intermediate angular momenta $j_{4\mathrm{p}+} = \frac{3}{2}$, $j_{4\mathrm{d}-} = \frac{3}{2}$ and $j_{4\mathrm{d}+} = \frac{5}{2}$ follow. These momenta then couple to the total angular momentum of the configuration of $j_{\mathrm{tot}} = \frac{11}{2}$.

2.3 Atomic processes

So far descriptions of possible energy states for the electrons were presented. However, transitions between these states also exist. Some of those transitions include processes, in which a change of electronic energy leads to the emission of a photon. Those photons then make up the characteristic lines of the atomic spectrum, with their energy sharply defined by the energy of the involved levels. Hence the emitted light is a direct probe of the previously described energetic structure and the distribution of electrons on the possible states. These characteristic lines are hence used as an observable in the experiments conducted in this work.
The theory behind the following processes is also used later to generate theoretical electronic state distributions and photon spectra.
An overview over those processes is given in [20], which this section orients on.

2.3.1 Collisional Ionization

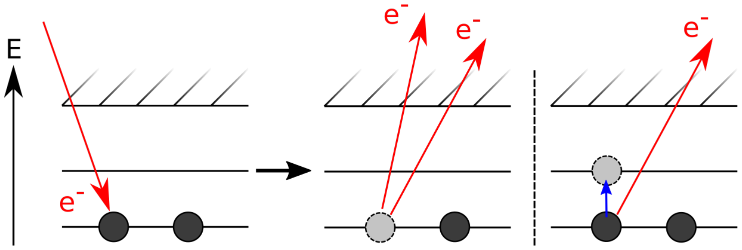

Figure 2.1: Symbolic depiction of the collisional ionization and excitation processes. A free electron hits the target atom or ion, scatters, leading to a shell electron being ejected or excited to a higher lying energy level.

In order to investigate the highly charged tin ions of interest, they first have to be produced. Inside an EBIT, described in the following chapter, one facilitates highly energetic electrons to initiate electron collision ionization.
If the kinetic energy of the electrons is sufficient, i.e. higher than the ionization potential of the target ion, $E_{\text{kin}} > E_{\text{ion}}$, then one shell electron of the ion may be removed upon collision of electron and ion.
Overall the process of ionization of an ion A of charge state q can be summarized by the following formula [20]:

$$A^{q+} + e^-(E_{\text{kin}}) \to A^{(q+1)+} + e^-(E_1) + e^-(E_2)$$

where the energies of the involved electrons have to adhere to the relation

$$E_{\text{kin}} - E_{\text{ion}} = E_1 + E_2$$

in order to fulfill energy conservation.
By repeating this process multiple times, highly charged ions can be produced from the originally neutral atoms.
The cross section σ of this interaction, for a given shell electron i, depends strongly on the kinetic energy E_{kin} of the incident free electron. This dependence

can be approximately be described by the empirical Lotz-formula [66]:

$$\sigma_i = a_i \frac{ln(E_{\text{kin}}/P_i)}{E_{\text{kin}} P_i}(1 - b_i e^{-c_i(\frac{E_{\text{kin}}}{P_i} - 1)}) \tag{2.34}$$

where a_i,b_i and c_i are empirical constants and P_i is the binding energy of the electron, which has to be lower than the kinetic energy E_{kin} of the free electron for the ionization process to occur. This ionization cross section describes the ionization from one specific electronic shell. For an estimation for the total ionization cross section, each of those individual contributions have to be added up:

$$\sigma_{\text{tot}} = \sum_i \sigma_i \tag{2.35}$$

By tuning the energy available to the electrons, i.e. the acceleration voltage in the setup, the prevalent charge states can be chosen, as the kinetic energy of the electrons limits the highest possible charge state that can be produced. This is because, for each electron removed from the ion, the ionization potential is increased, as the remaining hull electrons are more strongly bound due to the reduced shielding of the nucleus.

For tin, which is investigated in the later experiments, the ionization energies for ionization from the ground state are presented in Table 2.3.1, as given in [87], [18], [72], [44], [43] and [14].

If electronic levels with energies above the ground state are populated, then ionization may occur at lower energies.

Note here the large gaps between ionization energies of subsequent charge states, when a new subshell is to be opened up.

The maximum value for the electron impact ionization cross section as approximated by the Lotz formula 2.34 is reached at several times the ionization potential. Therefore it is beneficial for the production of a specific charge states to have free electrons, which have an energy just below the ionization potential of the next highest charge state.

Charge State	Ionization Energy
Sn	7.34 eV
Sn^{+}	14.63 eV
Sn^{2+}	30.51 eV
Sn^{3+}	40.74 eV
Sn^{4+}	77.03 eV
Sn^{5+}	94.0 eV
Sn^{6+}	112.9 eV
Sn^{7+}	135.0 eV
Sn^{8+}	156.0 eV
Sn^{9+}	184.0 eV
Sn^{10+}	208.0 eV
Sn^{11+}	232.0 eV
Sn^{12+}	258 eV
Sn^{13+}	282 eV
Sn^{14+}	379 eV
Sn^{15+}	407 eV
Sn^{16+}	437 eV
Sn^{17+}	466 eV
Sn^{18+}	506 eV
Sn^{19+}	537 eV
Sn^{20+}	608 eV

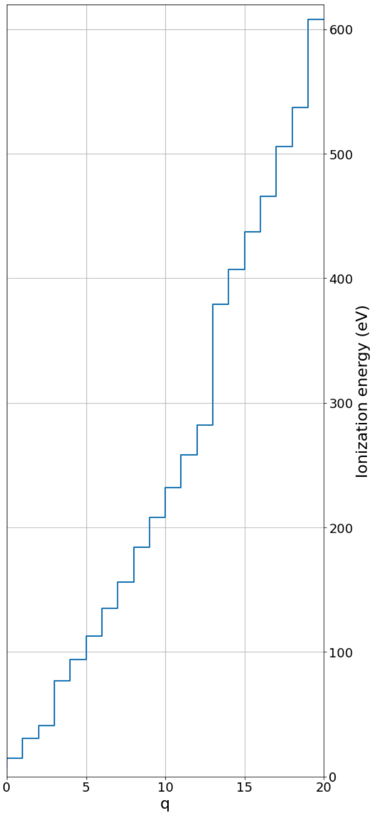

Table 2.2: Ionization energies of the first twenty ionization stages of tin as found in [87], [18], [72], [44], [43] and [14]. These ionization energies are depicted in the panel on the right, there the large gaps in ionization energies, when opening a new electronic subshell, are apparent.

2.3.2 Collisional Excitation

Another result of a collision of an electron and an ion, might be the excitation of one of the shell electrons of the ion. Instead of completely removing the electron from the ionic hull, as was the case for the collisional ionization, the electron is only elevated to a higher energy state [20]:

$$A^{q+} + e^{-}(E_{\text{in}}) \rightarrow [A^{q+}]^{*} + e^{-}(E_{\text{out}}) \qquad (2.36)$$

The now excited ion A^{q+} may in a next step either decay via spontaneous or stimulated photon emission, or autoionize in a next step, leading again to the loss of an electron (see also Auger-Effect [15]).

To quantify the excitation rates, induced by electron collision, several semi-empirical formulae exist. One commonly used equation is the Van-Regemorter formula [6]. As it is used later on to quantify the contributions of multiply excited states, it is discussed here in more detail. The description orients on the one given in [6].

Be Φ_n the unperturbed atomic wavefunction of the target ion for the energy level n, as determined with one of the methods described in the previous section 2.2. Introducing the wavefunction of the colliding electron as χ_n as a perturbation, one can define a total wavefunction of the two-particle system as

$$\Psi(\vec{r}_1, \vec{r}_2) = A \sum_n \Phi_n(\vec{r}_1)\chi_n(\vec{r}_2) \tag{2.37}$$

where $\vec{r}_1$ describes the location of the target ion, $\vec{r}_2$ the location of the projectile electron and A the antisymmetrizing operator. Inserting this total wavefunction into the time-independent Schrödinger equation

$$H\Psi(\vec{r}_1, \vec{r}_2) = E\Psi(\vec{r}_1, \vec{r}_2) \tag{2.38}$$

with solutions for the unperturbed atomic wavefunction known, one is left with a set of equations for the perturbing electron wavefunction

$$\left(\nabla^2 + \vec{k}_n^2\right) \chi_n(\vec{r}_2) = 2 \sum_{n'} \left(V_{nn'} - W_{nn'}\right) \chi_{n'}(\vec{r}_2) \tag{2.39}$$

with n' denoting the eigenstates of the electron after collision, $V_{nn'}$ being the interaction potential for the interaction between electron and ion and $W_{nn'}$ being the exchange operator. In order to solve this set of equations, one commonly used approximation is the Born-approximation [71], assuming that the electron only interacts weakly with the ionic collision partner, a plane wave for the electron wave function with the wave vector $\vec{k}_n$ can be imposed:

$$\chi_n = e^{i\vec{k}_n \vec{r}_2} \tag{2.40}$$

This approximation needs to be extended to the Coulomb-Born-approximation in the case of positive ions, as present in this thesis, to encompass Coulomb-waves [37], which are solutions for the Schrödinger equation for a spinless charged particle (another approximation) in a stationary $1/r$-potential, as the one of the target ion:

$$F_{\eta l}(\rho) = C_{\eta l}\rho^{l+1} e^{\pm i\rho} M(l + 1 \pm i\eta, 2l + 2, \mp 2i\rho) \tag{2.41}$$

using the radial coordinate $\rho = kr$, the angular momentum l of the free electron, the Sommerfeld parameter η, quantifying the perturbation of the plain wave due to the coulomb field and the confluent hypergeometric function M [67].

As stated before, this approximation is only valid if the interaction between the electron and the target ion remains weak, which is the case for electrons of high kinetic energies. Then the interaction time and thus the perturbation of the electron plain wave is low. In the case of highly charged ions, the coulomb interaction even at longer distances will be strong, making close collisions between electron and ion less important, improving the accuracy of the approximations done here when compared to lowly charged ions or neutrals, also for lower collision energies [6]. If one wants to include certain close-range perturbations for more accurate results, they can be reintroduced using the distorted-wave Born approximation [56].

With the Coulomb-Born approximation in place, the following proportionality for the collisional excitation cross section $Q_{nn'}$ can be used:

$$Q_{nn'} \propto |\langle\psi_{n'}|\, V_{nn'}\, |\psi_n\rangle|^2 \tag{2.42}$$

with $\psi_i = \phi_i F_i$. Now, one can assume the Bethe-approximation [71], stating that at high energies encounters with a large distance between the electron and the ion are most important, meaning the electron stays outside of the ionic volume. After a rather lengthy calculation, one arrives at the approximate electron impact excitation cross section Q_{if} for a transition between the atomic energy levels i and f:

$$Q_{if} = \frac{8\pi}{\sqrt{3}} \frac{1}{k_i^2} \frac{f_{if}}{\Delta E(Ry)} \overline{g} \pi a_0^2 \tag{2.43}$$

where f_{if} is the electric oscillator strength of the transition, k_i the wave number of the impact electron, $\Delta E(Ry)$ the energy of the transition in units of Rydberg (13.6 eV), a_0 the Bohr radius, and $\overline{g}$ is the effective Gaunt factor [9], which rescales the classical oscillator strength to the quantum mechanical system. For this factor, an empirical approximation can be used:

$$\overline{g} = 0.349 \log \frac{E_{\mathrm{kin}}}{\Delta E} + 0.455 \frac{\Delta E}{E_{\mathrm{kin}}} + 0.0988 \tag{2.44}$$

which is also dependant on the kinetic energy E_{kin} of the colliding electron. Inserting this approximation into the Bethe-approximation 2.43, the Van Regemorter formula is obtained. This cross section describes one specific excitation pathway, from the initial atomic state i to the final state f. When several possible final states exist, then a total cross section is formed by a sum over the individual cross sections

$$Q_i^{\mathrm{tot}} = \sum_f Q_{if} \tag{2.45}$$

This approximate cross section is proportional to the inverse of the electron energy (when disregarding the electron energy dependence of the approximation made for the gaunt factor). This can be understood as the interaction between electron and ion being less likely at higher electron velocities, due to shorter interaction times between the potential collision partners.

Although the accuracy of the Van Regemorter formula has been questioned [91], the general shape of this result for the electron energy-dependant cross-section makes for a good overview. It will thus be used later to fit experimental data. For the calculations done in this thesis, the distorted-wave Born approximation has been used, as implemented in the flexible atomic code (FAC), to obtain more accurate results.

For electron impact excitation to occur, again due to energy conservation, the energy of the incident electron has to be as high or higher than the energy gap of the electronic energy levels involved in the excitation process. Therefore a sharp rise of the cross section directly at threshold is to be expected, going from zero to a value of the order inscribed by the formula 2.43 at the threshold energy.

This, in theory sharp edge is softened in the experiment due to the finite energy spread of the electrons in the EBIT.

2.3.3 Spontaneous Emission

The main relaxation path for excited states in the conducted experiments is that of spontaneous emission [70]. Any atomic state, which isn't the groundstate may decay by emission of a photon, in order to minimize the energy of the system. This decay can either occur spontaneously, at a random time without external influences, or stimulated, where an external photon interacts with the excited ion, inciting it to emit another photon in the process of reaching the groundstate. In the conducted experiment, spontaneous emission is expected to be by far more prevalent, due to the low photon densities expected during the measurements (the present photons are mostly produced by spontaneous emission of other excited states). Thus, here only spontaneous emission will be discussed.
Overall, the process can simply be described by [20]

$$[A^{q+}]^* \rightarrow A^{q+} + \gamma(\Delta E) \tag{2.46}$$

where one photon γ with the energy ΔE, which corresponds to the energy difference of the involved atomic states, will be emitted.
Of course such a transition does not need to be from an excited state to specifically the groundstate. Instead, the destination of the transition may still be an excited state. This state then may itself decay again to another lower state, until, after several emissions, the groundstate is reached. Such a multitude of consequent decays is also called a "cascade" [35]. Especially in cases where there are a lot of different, closely lying atomic levels, cascades play an important role in explaining the emitted spectrum by an atom or ion.

The nature of quantum mechanics makes the it impossible to exactly define the time, when the decay occurs. Therefore only an average "lifetime" τ can be attributed to a certain transition [112]. This lifetime describes the average time it takes for a state to decay via spontaneous emission. An exponential decay of the excited population ensues:

$$N_{\text{exc}}(t) = N_{\text{exc}}(t=0)e^{-\frac{t}{\tau}} \tag{2.47}$$

This means even after a certain time, a population excited to a specific state earlier in a measurement cycle may still radiate later on.
The lifetime τ of an atomic state is directly inverse to the total transition rate:

$$\tau = \frac{1}{\sum_i T_i} \tag{2.48}$$

which is the sum of all individual transition rates for the transitions to energetically lower lying states.
A consequence of the spontaneous nature of the decay is the connection of the population of the excited state to the intensity of the emitted radiation, as can be seen from a derivation of 2.47:

$$I \propto \left|\dot{N}_{\text{exc}}(t)\right| = \frac{N_{\text{exc}}(t=0)}{\tau} e^{\frac{-t}{\tau}} \tag{2.49}$$

The strongest transition probabilities are inherent to electric dipole transitions [32]. Electric dipole transitions are transitions which are "allowed" according to classical quantum mechanics, without relativistic or quantum-electrodynamical effects. They are characterized by several selection rules for the magnetic quantum number m, orbital angular momentum quantum number l and the spin quantum number s of the initial state i and final state f partaking in the transition [32]:

$$\Delta m = m_i - m_f = 0, \pm 1$$
$$\Delta l = l_i - l_f = \pm 1$$
$$\Delta s = s_i - s_f = 0$$

Transitions between states not fulfilling these requirements, are classically "forbidden". They can still occur, but have much lower transition rates than electric dipole transitions. States with very long lifetimes (up to several seconds or even longer) due to only having access to such forbidden transitions are called metastable states. These states may then still be observed at a later time in the measurement cycles, long after being produced by electron collision.

Further, this lifetime is connected to the energy width of the spectral line. Due to Heisenbergs uncertainty relation for time and energy [53] there is a lower limit for the accuracy of the simultaneous determination of the time and the energy for an event:

$$\Delta E \cdot \tau \geq \frac{\hbar}{2} \tag{2.50}$$

with τ again being the average time of a transition to take place, ΔE the energy uncertainty and $\hbar$ the reduced Planck constant. This gives a lower limit for the accuracy with which a spectral line can be determined, with stronger transitions having a larger natural linewidth. A line resolved up to its natural linewidth has a lorentzian profile [22]. In the experiments presented here additional line broadening mechanisms are expected to dominate, such as doppler broadening [22] and detector resolution. These additional broadening effects are expected to result in a gaussian line profile.

2.3.4 Radiative Recombination

Inside an EBIT another important mechanism producing highly energetic photons is radiative recombination. This process encompasses a free electron recombining into a vacant position in an electronic shell of an ion. The energy, which is freed up by this process is then radiated away by a photon. Overall, the process can be written as [20]:

$$A^{q+} + e^{-}(E_{\text{kin}}) \rightarrow A^{(q-1)+} + \gamma(E_{\gamma}) \tag{2.51}$$

For the energy of the released photon the relation

$$E_{\gamma} = E_{\text{binding}} + E_{\text{kin}} \tag{2.52}$$

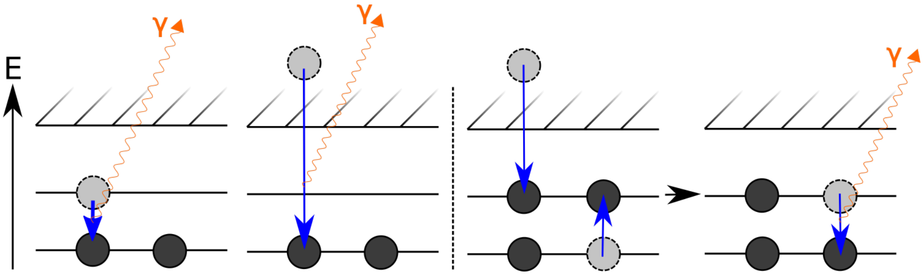

Figure 2.2: Left: Spontaneous emission and radiative recombination. An excited electron may spontaneously drop down to an energetically lower state under emission of a photon with an energy equal to the energy difference of the levels. Radiative recombination occurs when a free electron recombines into a vacant position in the atomic shell. A photon is released with energy equal to the binding energy of the new state and the kinetic energy of the recombining electron. **Right:** Symbolic depiction of a dielectronic recombination process. In a first step a free electron recombines with an ion under simultaneous excitation of a shell electron. Thus the energy condition for the kinetic energy of the free electron $E_{\text{kin}} = E_{\text{binding}} + E_{\text{exc}}$, as described in the main text must be fulfilled. In a second step the resulting excited state decays under the emission of a photon.

must hold, where E_{binding} is the binding energy of the newly captured electron in the atomic shell. Therefore the energy of photons, released via radiative recombination, is directly connected to the energy of the electron beam in the EBIT. Apart from being responsible for a part of the emitted photons, radiative recombination also plays an important role in the charge state balance [81], as it is one of the main drivers, reducing the charge state of the produced ions.

2.3.5 Dielectronic Recombination

Another important form of electronic recombination, which is observed in this work, is dielectronic recombination. A free electron recombines with an ion while simultaneously exciting one of the shell electrons of the ion. This results in a doubly excited state, which, in a subsequent step, either leads to re-emission of an electron (autoionization) or emission of a photon due to the relaxation of the excited state. The photon emission completes the dielectronic recombination. The complete process can be written as [20]:

$$A^{q+} + e^-(E_{\text{kin}}) \rightarrow [A^{(q-1)+}]^{**} \rightarrow A^{(q-1)+} + \gamma(E_\gamma) \tag{2.53}$$

where $[A^{(q-1)+}]^{**}$ symbolizes the doubly excited ion. The process is resonant, as the energy relation

$$E_{\text{kin}} = E_{\text{binding}} + E_{\text{exc}} \tag{2.54}$$

with the binding energy of the free electron after the recombination E_{binding} and the energy needed to excite the shell electron E_{exc}, has to be fulfilled. As seen in 2.53, the initial and final state of dielectronic and radiative recombination may be the same. This leads to quantum interferences and to so called "Fano profiles" when observing both forms of recombination simultaneously [52].

As a resonant process DR is very strong, if the energy condition 2.54 is fulfilled. At these electron energies bright emission features will occur and the charge

state balance is shifted towards lower charge states [40].
Dielectronic resonances are named according to the main quantum number of the involved electrons. For example, when speaking of an M-NO-resonances, one specifies, that the free electron recombines into the O-shell ($n = 5$) while exciting a shell electron from the M-shell ($n = 3$) to the N-shell ($n = 4$).

2.4 FAC Calculations

To have theoretical values as a comparison to the experimental results, calculations are done using the flexible atomic code (FAC [39]). The flexible atomic code is a software package doing its atomic structure calculations based on configuration interaction.

As described in section 2.2.2, generally using CI and its implementation in the FAC one can obtain energies of atomic states. Starting from this calculated atomic structure, radiative transition probabilities and electron energy dependant collisional excitation probabilities between different states can be obtained. The calculation of the electron impact excitation cross sections is performed using the distorted wave Born-approximation [116], and the radiative transition rates using the single multipole approximation, described further in [39].
However, from these raw quantities, no sensible spectra can be generated yet. First one has to obtain the population of the different energetic levels, as they will define the intensity of any spectral line, due to the number of radiative trasnsitions being directly related to the population of the excited state (see equation 2.49).
These populations are calculated using a collisional radiative model (CRM) [85], which is also included as a package in the FAC. In the following, the working principle of the used CRM for one isolated charge state is described, orienting on the description given in [38].
In collisional radiative models, one numerically solves a set of linear differential equations, each describing the evolution of the population of one specific electronic state.
Generally, there are both populating and depopulating processes for each state. For the calculation, one assumes all of the states to be in equilibrium, meaning the population of each state is constant after evolving for a finite time.
Then, in equilibrium, one can fix the the total population rate of a sample state i to equate the total depopulation rate of the state:

$$\sum_j C_i^j n_j = \sum_j C_j^i n_i \tag{2.55}$$

where n_a describes the population of level a and C_b^a the total transition rate from state a to state b. This transition rate can be comprised of many different factors. In the calculations conducted for this thesis collisional excitation and spontaneous emission are taken into account as they are the main drivers of population changes in the presented experiment. However, dielectronic resonances may also contribute strongly, if present and if one hits just the right beam energy to drive them. Due the complexity of the calculations needed, in order to find the multitude of resonances, which could be present here, their

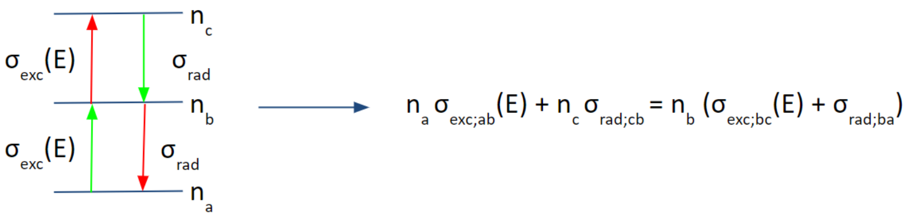

Figure 2.3: Simple case of a CRM calculation. In this three-level case, to calculate the population n_b of level b, all outgoing rates must equate all incoming rates. Fulfilling this condition for all levels simultaneously lets one solve the level populations using the CRM.

effect on the state populations is omitted.
With the set of equations of the form 2.55 for every single state i, one can solve numerically for the state populations n_i. As was seen in section 2.3, transition rates via collisional excitation are strongly dependant on the energy of the electrons in the plasma as well as the densities of ions and electrons. Thus, also the state population and therefore the spectra generated with this method change with the electron energy, especially once additional level thresholds are met and new states may be populated.

How such a state balance could look in a simple 3-state case is depicted in Figure 2.3. To calculate the population n_b of state b, all incoming rates (green) have to equate all outgoing rates (red). Asserting this condition for all levels, one can numerically solve for all level populations.

2.5 Multiply Excited States

Due to the recent findings in [108], the contributions of multiply excited states to the photon spectrum of several tin charge states are of special interest for this work.
In this work, multiply excited states are defined by the respective energy of the electronic state for simplicity. It turns out, that for several charge states of tin, the existent level structure can be grouped into several blocks of similar energies, which only overlap partially. This effect can be seen in Figure 2.4, where the calculated density of states for Sn^{12+} to Sn^{14+} is given.
When following the common definition for multiply excited states, as states which contain multiple different excited electrons, then these defined level blocks consist of states with different degrees of excitation. However, as in the experiment this separation cannot be made, and the different states can only be separated by their respective energies, here the different energy blocks are named by this excitation degree.

To obtain such multiply excited states, one can have a single excitation process, producing it directly from the ground state ion. This in turn means that the exciting particle, in the case of this work the free electron, needs a high energy.
Another pathway for the production of those multiply excited states would include several excitations with electrons of smaller energies. Then the first

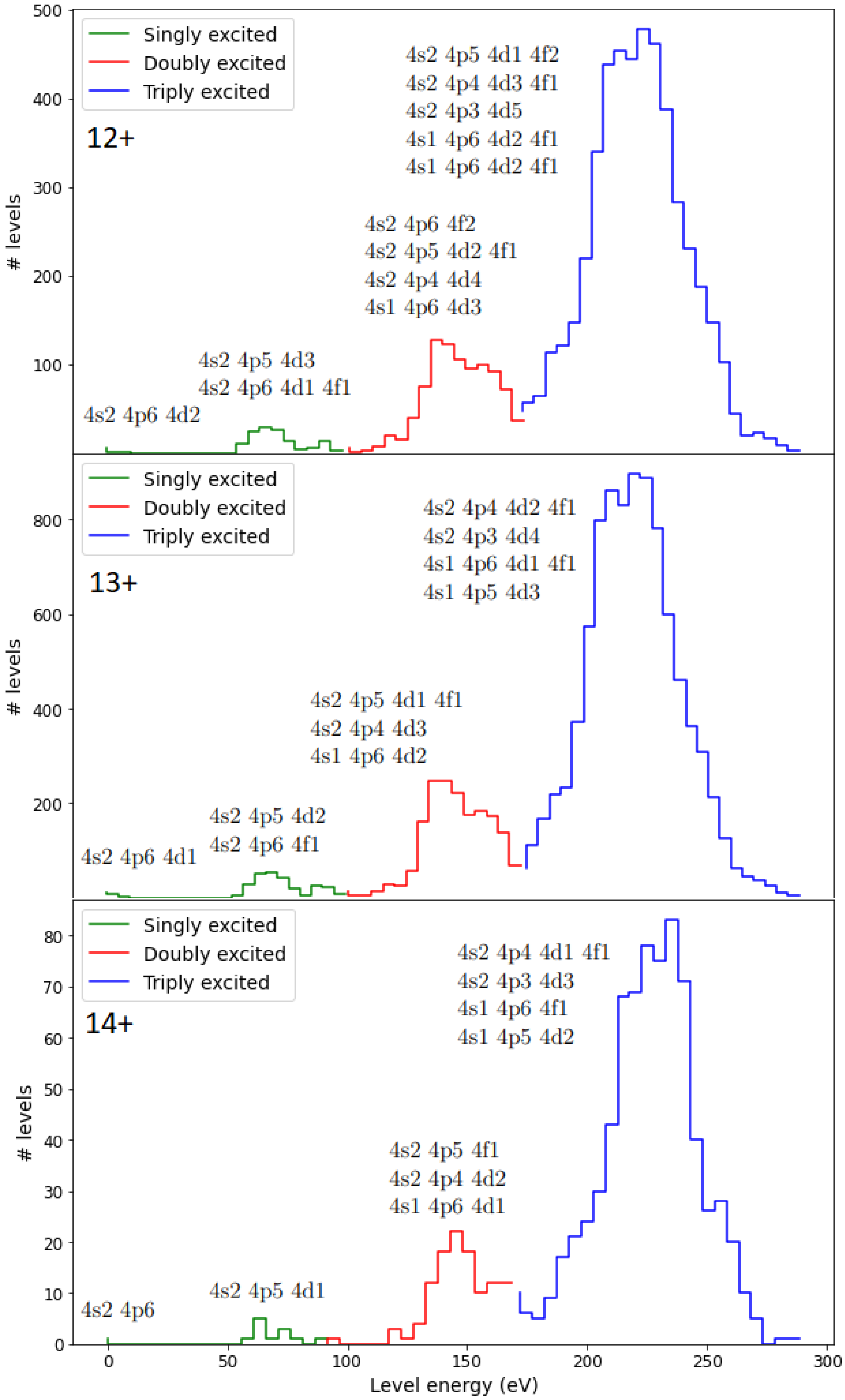

Figure 2.4: Density of electronic configurations in the energy space for Sn^{12+} - Sn^{14+}. The different energy blocks contained electron energy levels with the corresponding terms, just above the graph. At an energy of 0 eV the atomic ground state is displayed.

excitation process would produce a state of intermediate energy. The second excitation process would then elevate the ion from this intermediate energy level to the multiply excited state. For this production pathway to be relevant, an intermediate state needs to exist, which has a sufficiently long lifetime, as to not radiatively decay before the second excitation process occurs.

Therefore the production rate for a multiply excited state should be usually low at low energies due to the necessity of a metastable state of sufficiently long lifetime to exist. At higher energies an additional threshold is met, when the exciting electrons have enough energy to immediately produce the multiply excited state from the ground state, leading to highly amplified production rates. The relative prevalence of those different production pathways is defined by the plasma conditions however. In the present experiment, it can be expected, that most ions are in the ground state or a few metastable states at any given time. This is a result of relatively low electron and ion densities in the EBIT plasma as well as relatively low photon density during the experiment. In a laser-produced plasma on the other hand, such as investigated in [108], due to much higher densities, more persistent populations in excited states are to be expected. Therefore also the production rates of multiply excited states might be very different from the ones presented in the later parts of this work.

As can be seen in Figure 2.4, several thresholds can be made out, where the number of possible energy levels rises sharply. The number of available levels furthermore increases dramatically with the degree of excitation, due to more and more electrons being excited into previously empty shells of high orbital angular momentum l, meaning many different electron configurations of similar energy become possible.

This effect, leads to a presumedly strong amplification of spectral lines originating from transitions between different multiply excitated states. Even though populations, as well as transition rates might be smaller for any isolated state than for singly excited states, which would normally only lead to weak spectral lines, the sheer amount of different possible states can lead to strong contributions, which is to be quantified later on as part of the data analysis.

The complete results of the performed calculations, going further than the density of states in Figure 2.4, including transition wavelengths between the different excited states, are discussed later, when comparing them to the experimental results in section 7. There also results for Sn^{11+} and Sn^{15+} are shown, which were investigated in the experiment as well. Their density of state resembles the one from Sn^{12+} to Sn^{14+} shown above, with slight differences in energies of the multiply excited blocks and relative states contained in each block.

Chapter 3

Experimental Setup

After giving a short overview of the theoretical foundations of the atomic structure calculations and the different possible transitions between the electronic levels, the experimental apparatus in use is to be described next. The investigation of transitions originating from multiply excited states in highly charged tin leads to several requirements, which need to be fulfilled by such an apparatus. A device producing and trapping the highly charged ions is needed. The trapped ions need to be brought into contact with electrons of a well-defined energy, as to selectively produce only parts of the possible energy levels in the highly charged tin. Additionally, detectors are needed to characterize the light emitted from those excited states.

3.1 Electron Beam Ion Traps

As a method of producing and trapping the highly charged tin ions, the FLASH-EBIT [27] [28] at the Max-Planck-Institut für Kernphysik in Heidelberg has been facilitated.
An electron beam ion trap (EBIT) provides a magnetically compressed electron beam to repeatedly ionize inserted neutral atoms and trap the resulting (highly charged) ions via the space charge of the beam. Figure 3.1 shows a symbolic depiction of an EBIT, outlining the fundamental principles of its operation.

An electron gun, seen on the left hand side of the depiction supplies free electrons via a heated cathode. These free electrons are then accelerated by a potential difference between the negatively biased cathode and positively biased cylindrical electrodes, also known as drift tubes, in the the center of the machine. Controlling this potential difference allows for the control of the kinetic energy of the electrons making up the beam. This beam is compressed by a strong magnetic field produced by a pair of, in this case superconducting, Helmholtz coils surrounding the drift tube assortment. In the region surrounded by the drift tubes, the electron beam interacts with gas, let in via a differentially pumped injection system. This neutral gas gets collisionally ionized several times to produce highly charged ions. The producible charge states are limited by the kinetic energy of the beam electrons. These positive ions are then trapped radially by the space charge of the electron beam itself, and axially by the voltages

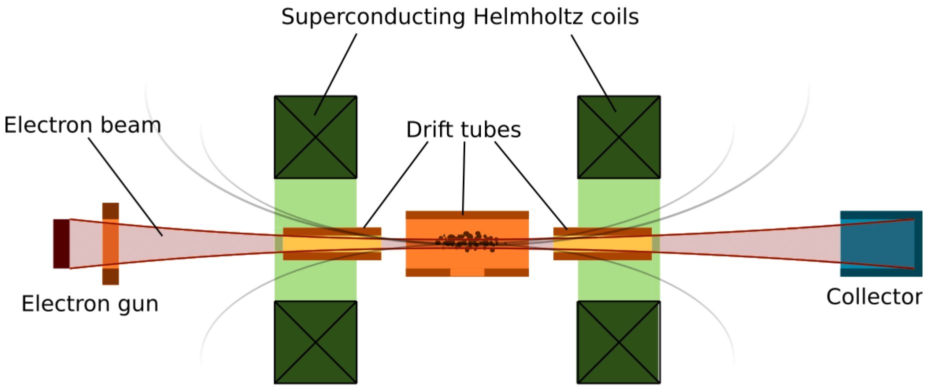

Figure 3.1: Symbolic depiction of an electron beam ion trap. Free electrons are supplied by a heated cathode and accelerated to an array of cylindrical drift tubes, set to a positive potential. The electron beam produced this way is compressed via a magnetic field. Interactions between the electrons and inserted neutrals leads to the production of highly charged ions, which are trapped in the central drift tube. The electron beam gets dumped in the end in a collector.

put on the drift tubes, with the central drift tube being on a lower potential than the adjacent ones. Interactions between the free electrons and the trapped ions may lead to photon emissions (see section 2.3), which can be detected by several spectrometers, connected to the central drift tube via viewports in that electrode. After passing the drift tubes and interacting with the inserted neutrals and produced ions, the electron beam gets decelerated at the collector and absorbed, closing the electric circuit.
A birdseye overview over FLASH-EBIT, the specific EBIT facilitated in this work, is shown in Figure 3.2.
In the following the different essential parts of the machine marked in Figure 3.2 are described in more detail..

3.1.1 Electron Gun

In a first step, free electrons are produced by a cathode made up of a tungsten-barium matrix [27], which is put on a negative potential. This cathode is heated by a surrounding coil to temperatures usually between $T_{\text{cat}} = 1300\,\text{K}$ and $T_{\text{cat}} = 1500\,\text{K}$ to allow for the escape of fast electrons out of the bulk material.
To produce a steady stream of electrons, a focus electrode and anode are placed in front of the cathode and put on a positive potential to guide the electrons in the direction of the trap center. The voltage settings of the two potentials controls the value of the electron beam current, with the current being connected to the focus voltage via the relation [61]

$$I = kV^{\frac{3}{2}} \tag{3.1}$$

with the constant of proportionality k being dependant on the cathode material and specific model, as well as the heat supplied by the coupled heater.
As the principles of operation of an EBIT make the presence of a strong magnetic

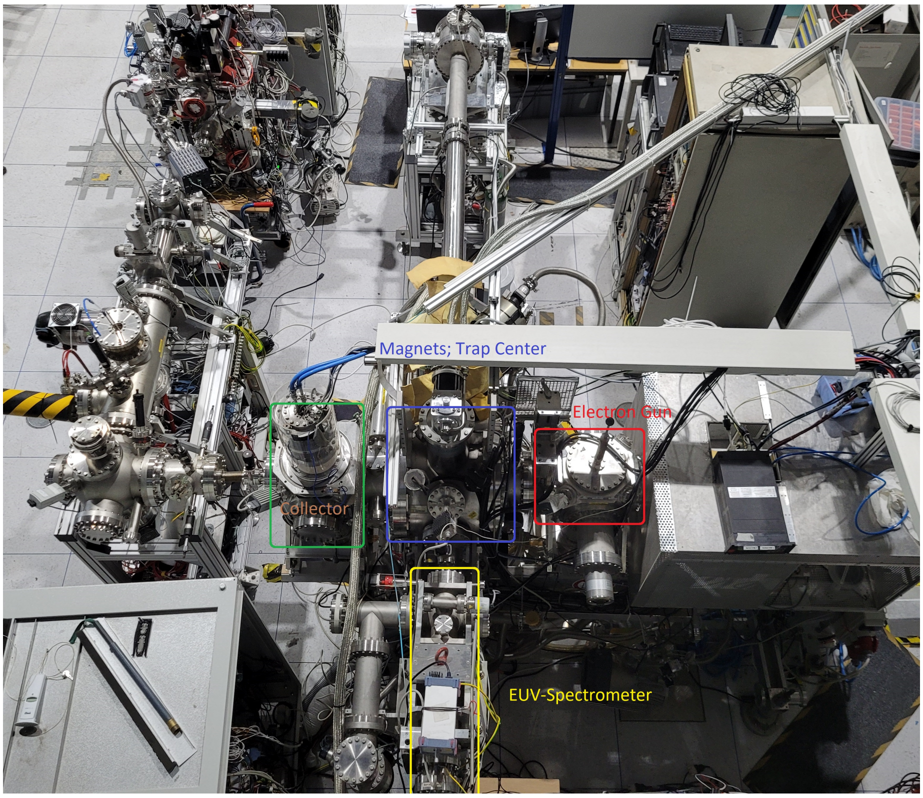

Figure 3.2: Birdseye view of FLASH-EBIT, the experimental apparatus used for the following experiments. The position of the central parts have been marked and labeled.

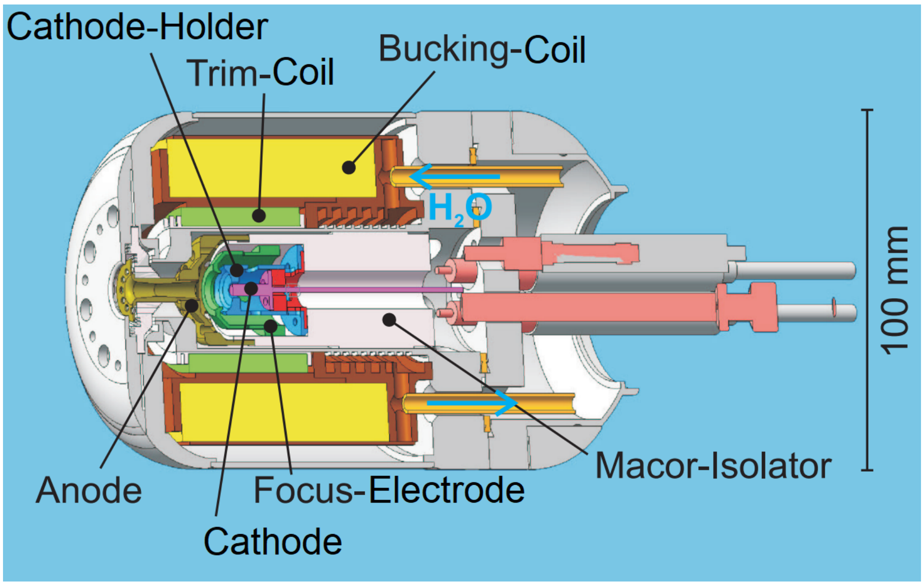

Figure 3.3: Model of the electron gun built installed in FLASH-EBIT. Adapted from [27].

field at the trap center necessary, the electron gun also includes a pair of small coils to offset the remaining magnetic field at the gun position. This magnetic field compensation allows the electron beam to be compressed further by the magnetic field at the trap center than if there still would be a magnetic field left [46]. This additional compression is beneficial as it directly results in higher current densities, leading to higher interaction rates between electrons and ions, improving count rates in the experiments to follow. The heat produced by the cathode heater and the coils offsetting the magnetic field of the main magnet gets transported away by a water chiller connected to the gun socket.

3.1.2 Trap Region

After the free electrons leave the gun, they get accelerated towards the center of the trap via a potential difference between the cathode and the trap center. There, several cylindrical electrodes are set to a positive potential. This accelerating potential sharply defines the kinetic energy of the electrons in the beam. Overall, including the space charge of the electron beam and trapped ions $\Phi_{\text{Spacecharge}}$, for which an approximate expression is derived in section 3.2, the total kinetic energy of the beam electrons is given by

$$E_{\text{kin}} = e\left(U_{\text{DT}} - U_{\text{Cathode}} + \Phi_{\text{Spacecharge}}\right) \tag{3.2}$$

with the elementary charge e, the voltages supplied to the cathode U_{Cathode} and the central drift tube U_{DT}.
FLASH-EBIT in particular possesses nine trap electrodes, also known as drift tubes, as depicted in Figure 3.4. The two outer ones (labeled C1 and G1 in the Figure) have the form of trumpets, as to better guide the electron beam into and out of the trap region and to shield the region of interaction between

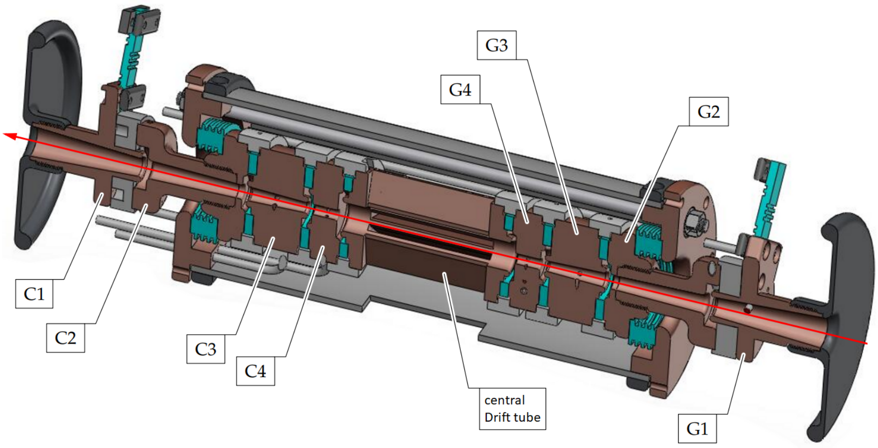

Figure 3.4: Model of the drift tube assortment in FLASH-EBIT. On each side of the central drift tube four additional electrodes are installed (G1-G4 on the gun side and C1-C4 on the collector side) to achieve axial trapping of the ion cloud. The red arrow indicates the electron beam path through the setup. Adapted from [8].

electrons and ions from outside radiation, possibly influencing the experiment. The most central drift tube, where the ion cloud resides, has a larger diameter than the surrounding drift tubes and several windows in the electrode material, allowing for light to escape to connected spectrometers and neutral gas to be inserted directly into the relevant region.
Radial trapping of the ions produced in the interaction region in the trap center is achieved via the space charge potential of the beam, approximately calculated in the later section 3.2.
To trap the ions in the axial direction, the drift tubes neighboring the central one (C4 and G4 in the Figure) are set to a more positive potential. This way a three-dimensional potential well is realized to keep the highly charged ions in the trap center. On the contrary, if one wants to empty the trap to get rid of residual gas, which also gets ionized by the electron beam, the central drift tube can be set to a high positive potential, "dumping" those unwanted contaminants.

Further radial trapping is achieved by a pair of Helmholtz-coils surrounding the drift tube setup. In the case of FLASH-EBIT these magnets are superconducting, in order to achieve high magnetic fields. Particles with radial momentum are being deflected due to the Lorentz force and describe a tight cyclotron motion [55]. Therefore it is even possible to trap the ions inside the trap for a limited amount of time without an electron beam (magnetic trapping mode) [5]. This effect also applies to the beam electrons, which leads to the electron beam being compressed by the ever increasing magnetic field near the trap region. The explicit effect on the electron beam radius is described in [46].
The need for superconducting magnets, as a way to produce the very high magnetic field of approximately 6 T [27] at the trap center, means that the machine needs to be cryogenically cooled. This is done via a helium compressor and corresponding cold head, cooling the magnet down as far as 4 K.

An additional benefit of this cooling is an improvement in the achievable vacuum. As is usual for atomic physics experiment, the environment of the particles must be under extremely low pressure, meaning ultra high vacuum at around $5 \cdot 10^{-10}$ mbar, maintained by an array of turbomolecular pumps. Much higher pressures would make the electron beam interact with residual gas long before reaching the trap region and the machine being non-functional, the ions in question not examinable. Even before reaching those conditions, charge exchange processes become more important as pressures rise [68]. This fact would in turn make the establishment of the wanted charge state distributions more difficult. Now the cryogenic environment additionally lets most residual gases in the EBIT freeze on its surfaces, meaning a decrease in free gas particles and thus pressure, basically letting the cold surfaces act as a cryopump [47].

The charge state balance inside the trap region is governed by the settings of the electron beam (energy and current), as well as the depth of the trapping potential set by the drift tube voltages and the amount of injection of neutral atoms. The ionization and recombination processes listed in section 2.3 drive the increases and reductions of the charges of the trapped ions. At any given trap condition, those processes balance out after a given trapping time to yield the observed charge state balance [65].

3.1.3 Collector

After the electron beam has passed the trap region and interacted with the inserted neutrals and produced ions, it needs to be dumped to complete the electric circuit. This is done in the collector, a schematic depiction of which can be seen in Figure 3.5.

As the beam electrons usually have a high kinetic energy, in the order of hundreds of electronvolts or even kiloelectronvolts, some electromagnetic deceleration and defocusing of the beam is needed. Otherwise the focused electron beam would damage the wall material of the machine, increasing pressure inside the vacuum chamber and producing dangerous radiation.

To supply this stopping power, the far side of the collector consists of an "extractor" electrode, set to a very high negative voltage, higher than the cathode voltage, to prevent piercing of the collector by the beam. This high negative voltage already achieves some level of defocusing of the beam. To add more to that, one additionally employs a collector-coil to produce a magnetic field inside of the collector, offsetting the main magnetic field. As an additional means to help in this beam widening, potentials can also be set on the front-shield, backshield and suppressor electrodes.

This widened beam then comes into contact with the inner walls of the collector, where the electrons are being absorbed.

This absorption heats up the collector material. To offset this temperature increase and keep the collector stable and operational it is connected to a water chiller, similar to the gun.

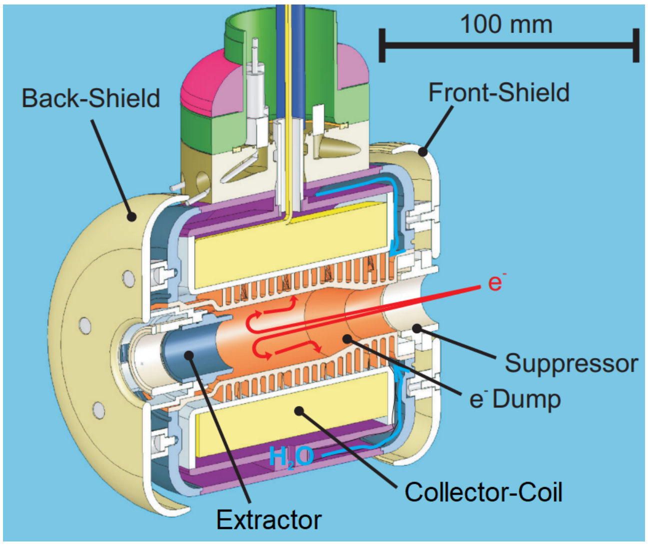

Figure 3.5: Model of the collector installed in FLASH-EBIT. Adapted from [27].

3.1.4 Injection System

In order to have highly charged ions produced inside the EBIT, first atoms have to be introduced into the trap region. This is achieved by a differentially pumped injection system, leading to the formation of an atomic beam.

Two stages, pumped by one turbomolecular pump each, lead to a directed beam of neutrals, directly from the source to the central trap region, inserted through a window in the central drift tube. As a source gases, liquids and solids can be used. In this work either molecular oxygen for the calibration of the used spectrometers or the different tin compounds, tin-acetyl-acetonate, tetra-n-butyl-tin or tin-propyl-tin have been inserted.

3.2 Space Charge in an EBIT

A central part of the working principle of an EBIT is the space charge of the electron beam, allowing for the radial trapping of the highly charged ions.

An additional effect of this space charge is the change of the electron energy itself due to its presence, as the repulsion of the electrons inside the trap at any given moment reduces the effective potential difference between the gun cathode and the trap center.

As later in the experimental part of this thesis, measurements with a variation of the energy of the electron beam will be conducted, in order to find excitation thresholds and contributions of multiply excited states in highly charged tin, an exact knowledge of the total electron beam energy needs to be achieved. Hence a derivation of the space charge and its dependence on the settings of the EBIT will be presented here.

For the sake of simplification, lets assume the electron beam to be an infinitely long cylinder of constant charge density ρ. This is a sufficient approximation, as the path the electron beam takes, from the gun all the way to the collector is much longer than the relevant interaction region in the central drift tube, which has a length of less than 10 cm. Using this approximation, the charge density will be dependant on the electron velocity v_e and the beam radius r_H [21], which can be estimated by Herrmann's method [46]:

$$\rho = \frac{I_e}{\pi r_H^2 v_e} \tag{3.3}$$

Using these assumptions, together with Gauss's law [24], two different cases for the space charge potential arise, depending on the distance to the beam axis:

(a) $r > r_H$:

$$\oint_A \vec{E}\, d\vec{A} = \frac{Q}{\epsilon_0} \tag{3.4}$$

$$\Rightarrow 2\pi r l E(r) = \frac{\pi r_H^2 \rho l}{\epsilon_0}$$

$$\Rightarrow E(r) = \frac{\rho r_H^2}{2 r \epsilon_0}$$

$$\Rightarrow \Phi_e = \int_0^r E(r^{'})\, dr^{'} = \frac{I_e}{2\pi v_e \epsilon_0} ln\,(r)$$

With Φ_D being the potential of the drift tube at the discussed location with a radius of r_D. Using this, one obtains

$$\Rightarrow \Phi_e = \Phi_D + \frac{I_e}{2\pi v_e \epsilon_0} ln \left(\frac{r}{r_D} \right) \tag{3.5}$$

(b) $r \leq r_H$:

$$\oint_A \vec{E}\, d\vec{A} = \frac{Q}{\epsilon_0}$$

$$\Rightarrow 2\pi r l E(r) = \frac{\pi r^2 \rho l}{\epsilon_0}$$

$$\Rightarrow E(r) = \frac{\rho r}{2\epsilon_0}$$

$$\Rightarrow \Phi_e = \int_0^r E(r^{'})\, dr^{'} = \frac{I_e}{4\pi v_e \epsilon_0 r_H^2} r^2$$

$$\Rightarrow \Phi_e = \frac{I_e}{4\pi v_e \epsilon_0} \left[\left(\frac{r}{r_H} \right)^2 + 2\,ln \left(\frac{r_H}{r_D} \right) - 1 \right] \tag{3.6}$$

In the last step, the result from formula 3.5 has been used.

Combining everything, the final expression for the space charge becomes

$$\Phi_e = \begin{cases} \frac{I_e}{4\pi v_e \epsilon_0} \left[\left(\frac{r}{r_H} \right)^2 + 2\,ln \left(\frac{r_H}{r_D} \right) - 1 \right] & r \leq r_H \\ \frac{I_e}{4\pi v_e \epsilon_0} 2\,ln \left(\frac{r}{r_D} \right) & r > r_H \end{cases} \tag{3.7}$$

In the end, one can see, that the space charge depends on both the electron beam current I_e, as well as the electron velocity, which relates directly to the electron energy:

$$\Phi_e \propto \frac{I_e}{\sqrt{E_e}} \tag{3.8}$$

Here and throughout the classical kinetic energy

$$E_{\text{kin}} = \frac{1}{2} m v^2$$

has been used as the energy of the electrons during the experiment is small and relativistic effects therefore negligible. The maximally used electron energy during the main experiments of 500 eV, results in a classical electron velocity of $v = 1.3 \cdot 10^7\ \frac{\mathrm{m}}{\mathrm{s}}$. This corresponds to a Lorentz factor [4] of

$$\gamma = \frac{1}{\sqrt{1 - \left(\frac{v}{c}\right)^2}} = 1.001$$

with the speed of light c.
As consequence of the result 3.8, if one wants to keep the spacecharge potential constant, and thus the trap depth, while varying either the energy or the current, the other quantity has to be varied accordingly as well.
Keeping the space charge potential constant has several advantages for the following measurements. For one, if the space charge potential, and with it the trap depth for the positive ions, changes rapidly, the ion cloud will contract and expand rapidly. This in turn might lead to a loss in trapped ions, reducing observed event rates in the experiments. Additionally having a constant space charge lets one ascertain the actual, space charge corrected, electron kinetic energy at any point during the measurement, if it was determined for one specific combination of I_e and E_e.
Apart from the electron space charge potential, there is another influence on the potential landscape inside the trap region. As positive ions are being produced by the means of electron impact ionization, the negative space charge of the electrons is being compensated. This compensation is dependant on the injection pressure of neutral gas, as well as the trap depth. A deeper trap will let more positive ions accumulate and a higher injection pressure will increase production rates. During the experiments presented here, a shallow trap of similar depth was chosen throughout and the injection pressure was not varied to a

large degree. Therefore this compensation effect can be assumed to be roughly constant over the different measurements and will not be considered further. However, this compensation makes an assumption of the actual electron density from the space charge difficult.

3.3 Detection System

Two different detectors are employed in this experiment, an EUV spectrometer, based on a flat-field reflection grating and a microchannel plate (MCP) to detect radiation in the wavelength region from 12 nm - 18 nm, as well as a silicon-drift-detector (SDD), to detect high-energy X-rays with energies of at least 250 eV. The individual parts of those detection systems will be discussed in the following sections.

3.3.1 Microchannel Plates

Microchannel plates, or MCPs, are widely used detection systems for laboratory experiments on atomic systems. A comprehensive overview can be found in [118]. Specific details on the MCP used in this work, the DLD 40 by Roentdek, can be found in [88], with information in this section being from those two sources.
The body of the detector, encased by two metal plates, is made of a insulating glass slab, in which multiple holes are drilled. These holes are tilted against the normal of the plate in most modern variations of this detector type. For the detector in use here, this angle is 8 °. The inner walls of these holes are coated with a semiconductor material. The two metal plates are set to be on a high voltage potential difference, with the back side being much more positive than the front side. During this experiment, the voltage difference between the sides of the MCP mounted in the EUV spectrometer was set to 2400 V.
Now, if a charged particle or a photon reaches one of the holes (channels) of the MCP, it will impact on the inner wall of the channel, due to its tilt. Upon impact, the particle will release electrons from the semiconductor material, which will be accelerated due to the potential difference between the two sides of the MCP. The accelerated electrons will again hit the wall, releasing more subsequent electrons. A cascade ensues. The electron cascade travels through the channel and gets collected on the back side of the MCP. The employed tilted configuration of the channels here leads to little radiation passing the detector without hitting a wall, resulting in high detection efficiencies.
In the end, the single particle entering the detector produces many secondary charges, resulting in a measurable electronic signal at the back side of the detector with a typical amplification of a factor of 10^3 to 10^4, which can subsequently be amplified even further by readout electronics and fed into a data acquisition system.
One commonly used configuration of the MCP, known as the "Chevron configuration" [19], consists of two MCPs stacked on top of each other. The channels of one MCP are rotated by 180 ° with respect to the ones of the other plate. This yields the benefit of detecting even particles, which would normally hit the detector at such an angle, that they wouldn't come into contact with the channel walls, passing the detector without interactions. Furthermore the amplification

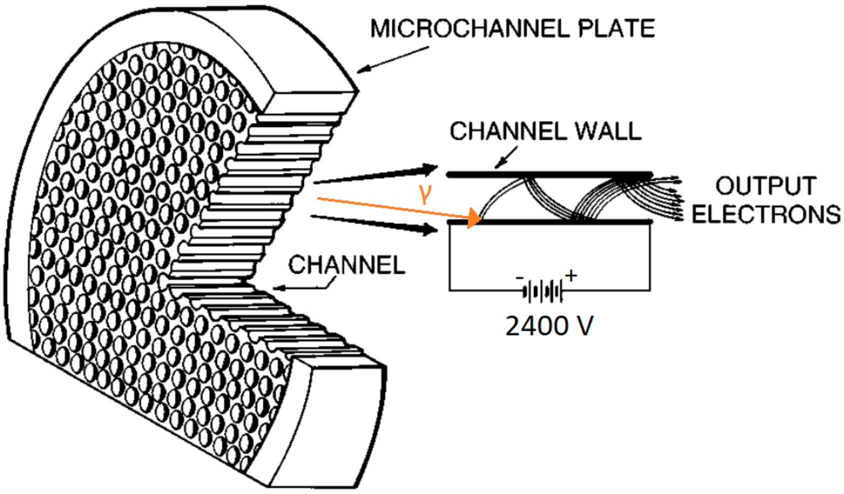

Figure 3.6: Schematic representation of the working principle of an MCP. Incoming photons release an electron from the semiconductor coated wall of one of the channels. The electron gets accelerated via the voltage difference applied between the sides of the MCP and releases secondary electrons from the wall material. A cascade ensues. The electron cascade gets caught on the back side as an electrical signal for further processing. Figure adapted from [117].

of the two MCPs is multiplied. This configuration is employed in the detector used in this work, yielding an amplification factor of at least 10^7 [88].
To gain the information, of where the initial particle hit the MCP, or in which channel the cascade was produced, one can apply several electronic configurations for the back side anode of the MCP. The MCP employed in the EUV spectrometer here uses a delay-line anode [101].
A delay-line anode consists of two bent wires, crossing each other and creating a mesh over the whole detector area. When the electron cascade hits the anode, the charge is transferred to the wires and transported off to the signal processing electronics. The time delay between the signal arriving at the end of each of the two wires is recorded and due to the wire shape, this delay is unique for every position on the anode. This simple method has one drawback however, as it is vulnerable to an unwanted bending of the delay lines, which introduces additional errors in the data, as will be seen later in the analysis.
Additionally to the time delays, which provide the spatial information for each recorded event, the MCP also provides the timing information for each event.

3.3.2 EUV Spectrometer

The spectroscopic system in the EUV range used here is a simple two-part spectrometer. A detailed description of it can be found in [58]. Light coupled out from the trap region reaches a Hitachi flat-field grating [42] with a spectral range of 5 nm - 35 nm, at grazing incidence and gets reflected towards a light-sensitive-detector, in this case the aforementioned MCP.

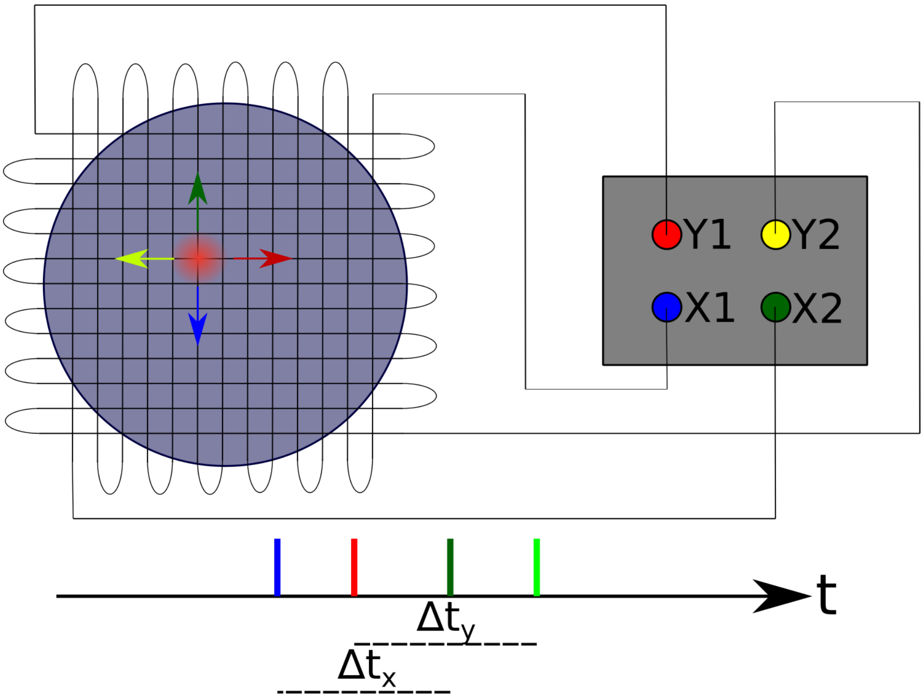

Figure 3.7: Schematic representation of the delay line principle. The deposited charge on the MCP anode gets transported along two bent wires. The resulting time delays for the signals in the accompanying readout electronics, stemming from the difference in traveled distance, lets one reconstruct the position of the incoming particle.

The Roentdek MCP in use, with an active, signal collecting diameter of 45 mm can be moved up and down along the dispersive axis of the reflective grating using an ultrahigh-vacuum-compatible manipulator. This way, one can select the spectral range, which is to be recorded. Also, the choice can be made to either record the emission spectrum in first order for higher count rates, or in second order to achieve a higher resolution. In favor of the high resolution, the spectra shown in this thesis are recorded in second order.
Three screws on the mounting of the MCP allow for the setting of a two-dimensional tilt, normal to the incident light. The variation of this tilt is used to find the best possible focusing of the spectrometer and is done for a specific height, and thus spectral range, of the MCP. The ideal settings are found by varying the tilt and recording spectral lines, while minimizing their width. This optimization was done before taking the first spectra for this work.

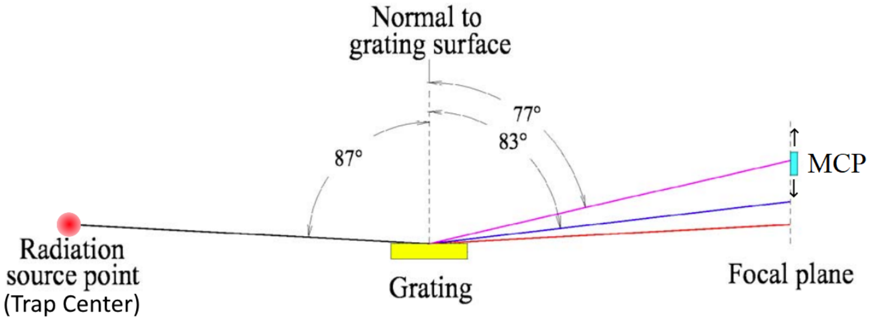

Figure 3.8: Schematic representation of the spectrometer setup for the EUV-range. Figure adapted from [58].

3.3.3 X-Ray Detector

In addition to the EUV-spectrometer, a silicon drift detector [103] is installed to detect x-rays produced in the trap region.

A silicon drift detector (SDD) is a semiconductor detector. Its body is made up of a disc of an n-doped silicon wafer. The back of the detector is contacted on a negative potential. A small central region on the front side is contacted on a positive potential. The contacts, as well as a series of rings on the front side of the detector are p-doped.

When highly energetic photons hit the detector, they produce electron-hole pairs in the substrate. The electrons drift towards the front side, due to the voltage difference applied between the sides of the detector. Additionally they drift towards the central collecting anode, as a result of the voltages applied to the rings on the front side. The constructed potential landscape inside the substrate makes sure a high amount of the produced electrons gets collected at the anode, being beneficial for the efficiency and the energy resolution.

The electrons reaching the anode produce an electrical pulse, which gets amplified by the readout electronics to be converted into a digital voltage and recorded as a photon event.

The number of electrons and therefore the signal strength is directly proportional to the photon energy deposited in the detector material. As one can record the time of the individual electrical pulses, this detector also supplies a time resolution for each observed photon.

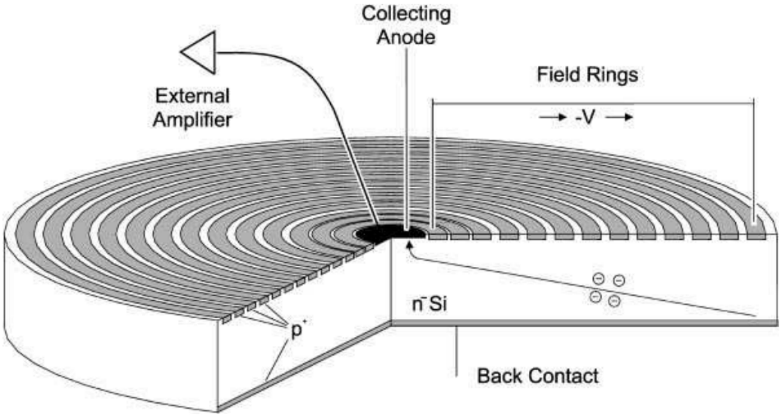

Figure 3.9: Schematic representation of a silicon drift detector. Figure taken from [62]. High energy photons impacting on the detector create electron-hole pairs in the semiconductor material. The free electrons get transported to the anode and can be read out as an electrical signal.

3.4 Measurement Scheme

The aim of the conducted experiments is to gauge, how much multiply excited states in highly charged tin ions from Sn^{11+} up to Sn^{15+} contribute to the extreme ultraviolet (EUV) spectrum.
In order to answer this question, one needs to selectively produce these tin charge states, excite shell electrons to specific energy states and observe their subsequent radiative decay.
These requirements make it necessary to employ a measurement cycle consisting of multiple phases.
First, the desired highly charged tin ions are being produced inside the EBIT. The best settings for the electron energy to produce the desired charge states are estimated from a measurement, discussed in section 5. This production phase is set for a time period long enough to get a steady state charge state distribution. After the production phase, the settings are switched over to the scanning phase. During this phase, the electron beam energy is being swept across a large range, while simultaneously recording the photon spectrum with the EUV spectrometer. Timestamps for each event are generated to relate the photon spectrum to the electron energy later. This scanning phase needs to be sufficiently short, as not to lose a significant portion of the ions produced in the breeding phase to recombination processes.

At each electron energy during this scanning phase, only certain upper states are available for production due to electron impact excitation, as the electron kinetic energy must at least be as high as the transition energy for the specific production channel. All of these produced upper states are then expected to decay radiatively. Therefore the detected intensity at each electron energy can be related to the production rate of the upper states via collisional excitation and thus the electron energy dependant collisional excitation cross section. As

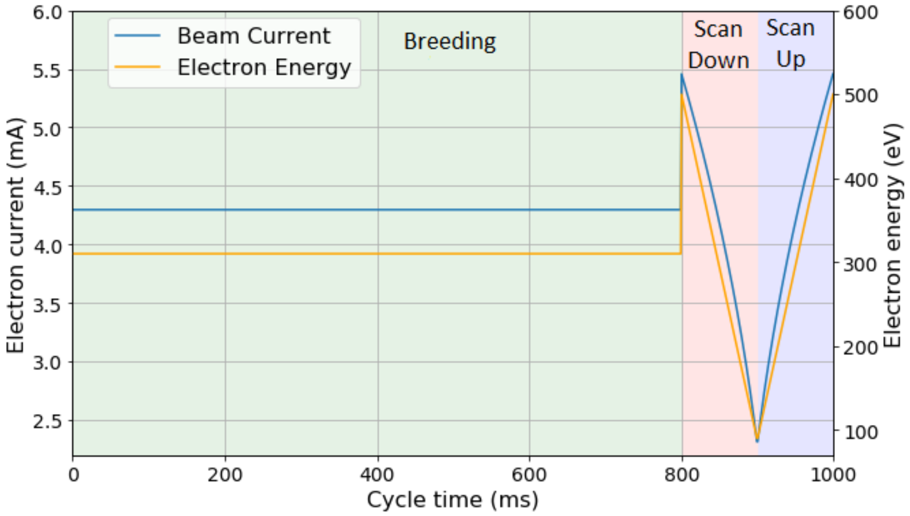

Figure 3.10: A typical measurement cycle as employed in the experiment. After a breeding cycle to produce the wanted tin charge state, a fast energy sweep is conducted to record the EUV-spectrum of highly charged tin dependant on the energy of the electrons, exciting the ions. Electron energy and beam current are varied simultaneously to keep the electron density constant.

the different upper levels furthermore each have radiative transitions of different wavelengths, it is possible to individually determine the production thresholds for those states by observing only the intensity in a tight wavelength window. By the relative change in intensity at these thresholds, also the relative oscillator strengths for the different excitation pathways can be determined.
In a low density plasma, with high electron densities, as present in the EBIT, electron impact excitation is by far the most important process for populating excited states. During a fast scan as presented here, the contribution to the spectrum stemming from metastable states produced during the breeding phase should be approximately constant, given long enough lifetimes. The contributions of short-lived metastable states would decay exponentially during the measurement cycle. If they are prevalent, then both flanks of the scanning phase will not be symmetric. This symmetry is checked later and confirmed.
Therefore during the fast scan, only transitions originating from short lived states produced during the fast scan are expected to contribute to variations of line intensities. Thus for the electron energy dependant intensity the connection to the collisional excitation cross section σ_{CE},

$$I(E_{\mathrm{kin}}) \propto \sigma_{\mathrm{CE}}(E_{\mathrm{kin}}) \cdot f + N_{\mathrm{ms}}(E_{\mathrm{breed}}) \cdot \mathrm{e}^{-\frac{t}{\tau}} \cdot f_{\mathrm{ms}} \tag{3.9}$$

can be made, with the transition strengths f and f_{ms} for the short lived and the metastable states and the metastable population at the breeding energy $N_{\mathrm{ms}}(E_{\mathrm{breed}})$ with a lifetime of τ. Assuming fast, and complete de-excitation of the upper levels via radiative transitions, the intensity will just be dependant

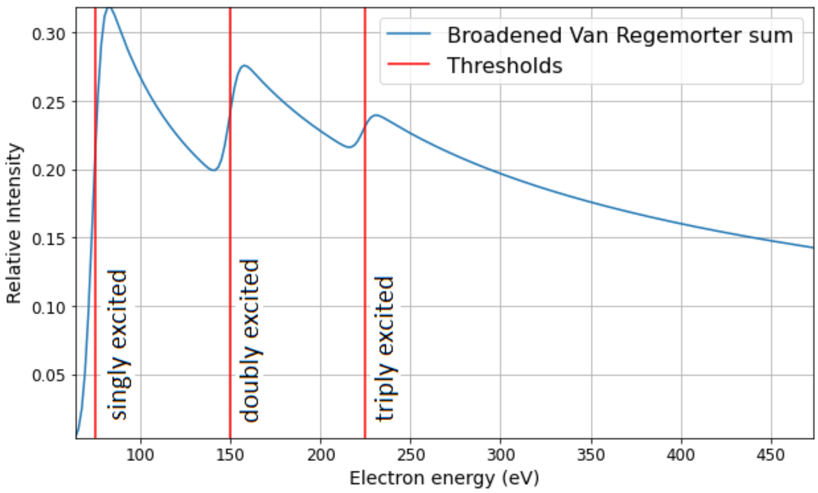

Figure 3.11: Expected intensity in a specific wavelength region depending on the electron beam energy with contribution of three energy levels as upper states. Upon reaching their production threshold via collisional excitation, new upper levels may become available for transitions in a specific spectral region. Each available energy state is assumed to be populated via collisional excitation, following the approximate Van Regemorter relation. Expecting sufficiently fast radiative decays, the line intensity becomes proportional to the collisional excitation rate. Multiple transitions are then adding up to a total intensity in a given spectral region. The complete intensity function is folded with a gaussian for better comparison to expected experimental results, taking into account the finite electron energy width.

on the population rate of the upper level,

$$I(E_{\mathrm{kin}}) \propto \sigma_{\mathrm{CE}}(E_{\mathrm{kin}})$$

For the case of transitions from several different upper states radiating in an observed wavelength region, for the total electron impact excitation cross section $\sigma_{\mathrm{CE}}(E_{\mathrm{kin}})$ a sum of Van Regemorter relations 2.43 can be imposed, as presented in Figure 3.11.

As discussed in section 2.3.2, for a given transition, this cross section gets reduced for higher electron energies.

However, if the energy of the electrons is high enough to allow the excitation of an additional level with a radiative transition in the defined wavelength region, the recorded intensity is expected to rise at that electron energy, as the individual production rates can be added up and all contribute to the recorded intensity. This way the energies of multiply excited states as well as their relative contributions to the EUV-spectrum of highly charged tin can be extracted by these apparent steps in the relative spectral intensity. If one assumes, that initially most ions are in their ground state, then the location of the thresholds is a direct probe of the individual energy levels of the excited states. The resulting distribution of thresholds should then reproduce the energetic structure of the tin ions, with several blocks of multiply excited states as presented in Figure 2.4.

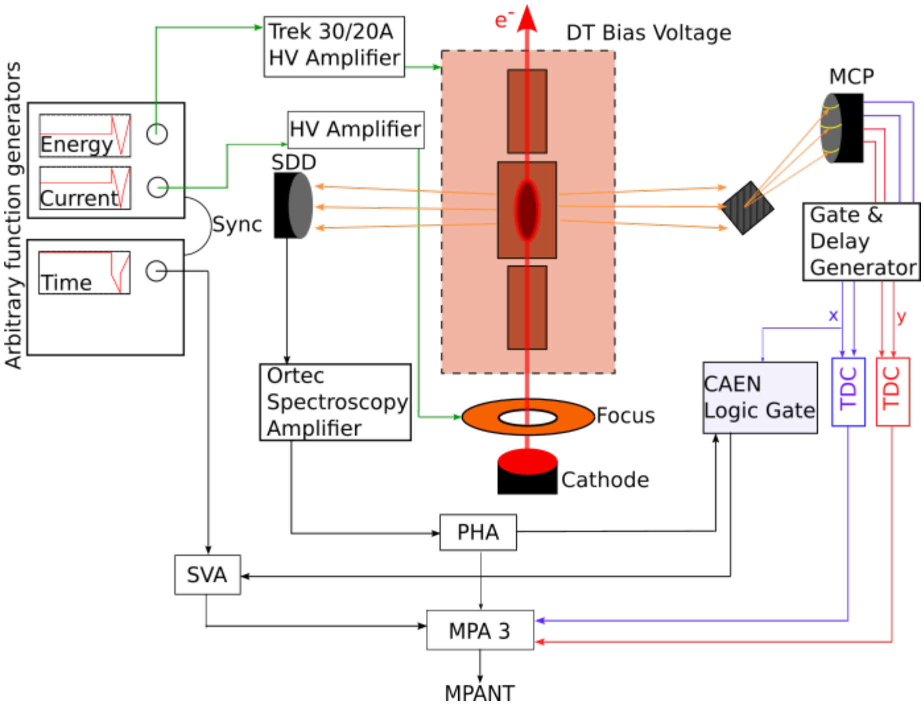

Figure 3.12: Scheme of the experimental control as employed in the presented measurements.

In addition to a variation of the energy, the current is varied as well during the experiments. As seen in section 3.2, to keep the space charge constant, the settings of the EBIT must follow the trend

$$I \propto \sqrt{E_e} \tag{3.10}$$

As discussed previously, keeping the space charge constant has several benefits. One of those benefits is, that when keeping the ratio $\frac{I}{\sqrt{E_e}}$ constant, the space charge needs to be determined only once, to know the actual electron energy at any point during the measurement. Additionally, a quickly alternating space charge value can have a detrimental effect on the ion population. The ion cloud might expand and contract rapidly, causing it to heat up. This heating may then lead to a significant fraction of the ions to be expelled from the trap in each measurement cycle.

A complete scheme of the experimental control setup, used to control the beam energy and current, as well as to collect the signals from the employed detectors is shown in Figure 3.12.

Two synchronized arbitrary function generators supply three signals to control the experiment. One channel controls the bias voltage of the drift tube setup, and with that the electron beam energy, by controlling the voltage supplied by a TREK 30/20A high voltage amplifier. The second channel sends its signal to another high-voltage amplifier supplying the focus electrode and thus controlling the beam current. The third channel directly feeds into the data acquisition

system and is used to create timestamps for each detected photon, to correlate them to the electron beam energy.
The data acquisition system facilitates multiple ADCs (analog-to-digital-converters) in several modes of operation. The amplified signal coming from the SDD is fed into an ADC operating in pulse-height-analysis (PHA) mode, digitizing the maximum value of an incoming signal, which corresponds to the energy of the photons impinging on the SDD. The signals coming from the MCP pass a gate and delay generator, creating a time signal independent of the incoming signal shape and amplitude for accurate and consistent time delay measurements. These time delays are fed into two time-delay-converters (TDCs), where the time delays are digitized and relaid to the control software. From those delays the location of the event on the detector is recovered. The signals from both the detectors are gated by the time signal coming from the function generator in order to coincide the time during the measurement cycle with the photon events to create two-dimensional spectra. All of the signals from the different ADCs are fed into the MPA-3 system, where the data can be visualized using the MPANT software during the experiment. For the subsequent analysis, each event is saved in a binary .lst-file, for full availability of the data.

Chapter 4

Preparatory Measurements

Before taking the spectra of highly charged tin and determining the contributions of multiply excited states to the EUV-spectra of the charge states from Sn^{11+} to Sn^{15+}, first some preparatory measurements have to be conducted. To extract the correct EUV spectra of the highest possible resolution, the MCP data has to be rotated and projected in the correct way and errors in the imaging system need to be digitally corrected. To correctly control the beam current, a correlation has to be made between the focus voltage as a controlling element and the current itself. Lastly a calibration spectrum using oxygen is taken and the space charge experimentally determined to know both the photon as well as the electron energy for each event during the main measurements. After all those preparatory steps are undertaken, the data analysis on the tin spectra will be conducted in the following chapters 5 and 6.

4.1 MCP Image Rotation and Projection

Before starting to take calibration spectra of oxygen and the actual measurements on the highly charged tin, in a first step the detector setup has to be optimized to yield the best possible resolution for the spectral lines.
First of all, the MCP, which is used to collect the photons reflected by the spectral grating, is not placed exactly orthogonal to the dispersive axis of the grating due to mechanical limitations when installing the detector.
Instead, the MCP is tilted slightly against this axis. This tilt needs to be digitally corrected. Otherwise projections along the MCP axis would not coincide with projections along the dispersive axis of the grating and yield an increased apparent width of the recorded spectral lines. To find the tilt between these two axes, an arbitrary spectrum with strong spectral features has been taken and several image rotations were tested.
For each applied rotation, the resulting data set has been split in two halves, according to whether the photon hits the left or the right side of the MCP, as can be seen in Figure 4.1. Then a projection along the y-axis of the MCP for both of the split data sets has been done.

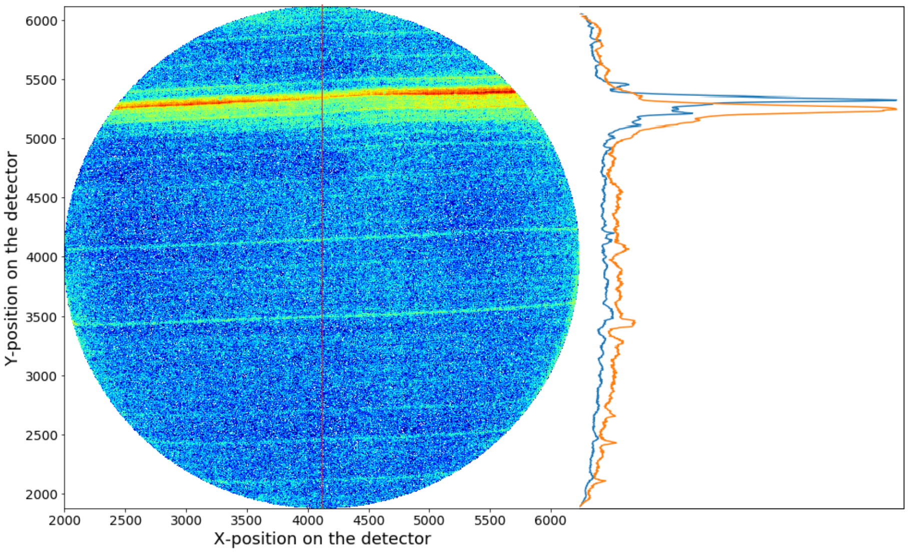

Figure 4.1: Example raw data set without applied rotation. The data set is split in the middle, according to the depicted line, into a left and a right set. Both sides are separately projected onto the y-axis on the right side (blue curve: right side, orange curve: left side). The dissimilarity of these two projections is supposed to be minimized in the following to find the optimal angle of rotation.

These two projections are then compared by giving a squared difference for each bin of the projection and summing all of the differences:

$$\chi^2 = \sum_n (l_n - r_n)^2 \tag{4.1}$$

with n denoting the y-coordinate of the projected data, l_n the projected events on the left part of the MCP for the row n and r_n the projected events for the right half respectively. Thus, the value of χ^2 gives a measure of how similar the recorded spectra on both sides of the MCP are and has to be minimal at the perfect angle of rotation, as then systematic shifts between these two projections vanish.

The values for χ^2 for the tested angles of rotation are shown in Figure 4.2. As can be seen there, the value for χ^2 gets minimal for an angle of $-2.12°$. Therefore, any collected data sets were first rotated by this angle before analyzing them further.

Additionally, when projecting data onto the dispersive axis, one has to take into account the circular shape of the detector. A raw two-dimensional histogram of recorded events after just correcting the angle of rotation can be seen in the left panel of Figure 4.3.

One can see that there are several irregularities near the edge of the detector, often leading to increased count rates, independently of the recorded spectral lines. Furthermore, events are recorded outside of the actual detector area. These events can be assumed to be artefacts. To avoid counting all of these aberrations, a circular region of interest is defined, as marked in red in Figure

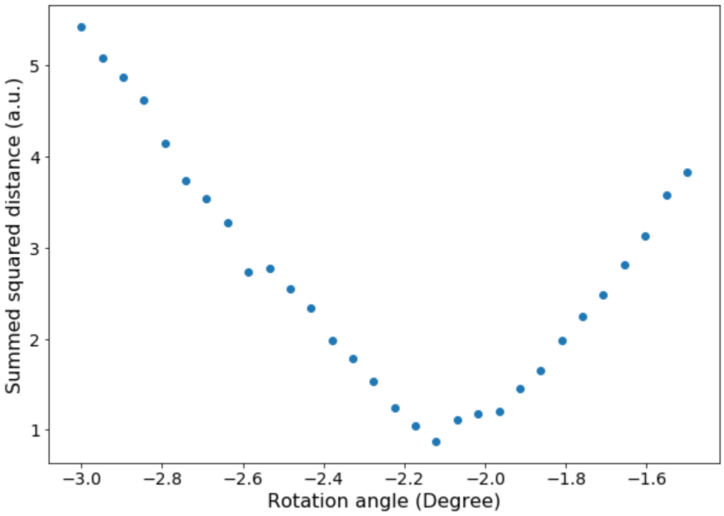

Figure 4.2: The summed squared distances according to equation 4.1 and the method mentioned in the text. The resulting best angle of rotation is −2.12°.

4.3, slightly smaller than the detector, with every event outside of that region of interest being discarded.

When then projecting data onto the dispersive axis of the MCP, one has to additionally weigh the signal in each row, depending on the width of the circular region of interest at that height. Otherwise, spectral lines recorded at the edges of the region of interest would appear systematically weaker than lines of the same intensity at the center. The weighting function is shown in the right panel of Figure 4.3 with a comparison of a weighted and an unweighted data set in Figure 4.4. In order to avoid extreme weighting at the upper and lower edges of the circular region of interest due to the small width of the rows, narrow slices at the top and the bottom of the MCP are left out of the projections. The data excluded this way corresponds to about 5 % of the recorded wavelength region and contains only very few events due to the small width of the MCP there. Therefore, little information is lost by this treatment of the raw data.
Every one-dimensional wavelength spectrum in the analysis is produced using such a circular region of interest and weighting function.

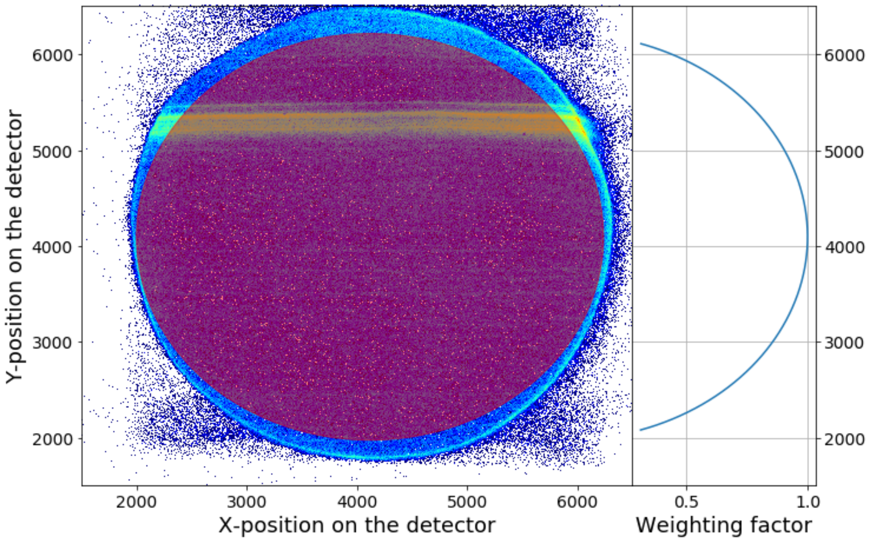

Figure 4.3: Left: The rotated image of the MCP with the selected region of interest in red. The events near the edges of the MCP have been discarded, as these were prone to artifacts and noise. **Right:** The weighting function when projecting events onto the dispersive axis. The raw spectrum gets divided by this function, representing the width of each row in the circular region of interest.

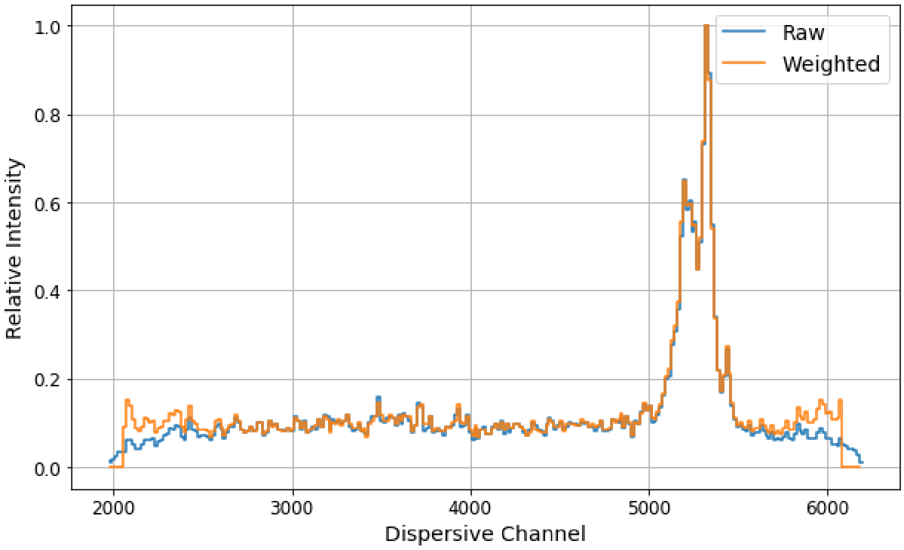

Figure 4.4: Two spectra from the same measurement, one with employing the weighting function shown in Figure 4.3 and one without weighting.

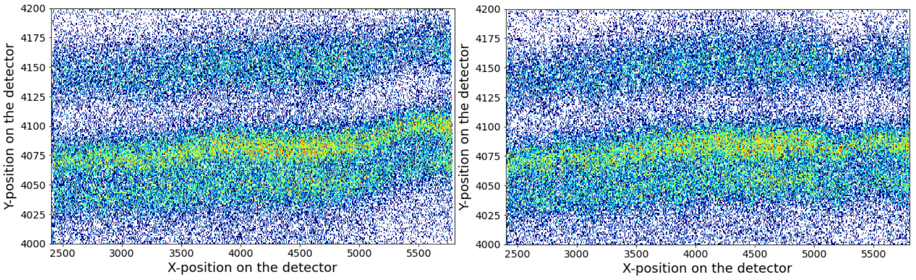

Figure 4.5: Zoom in on one of the spectral lines on the MCP. A deformation of the delay line wires causes an apparent deformation of the spectral lines, which are straight in reality. This deformation needs to be corrected in the following. **Left:** Before correction. **Right:** After correction as described in this section.

4.2 MCP Linearization

Apart from a necessary rotation, there is another correction of the data, which has to be done before the actual analysis of the tin measurements. The delay line used to obtain x- and y-positions of the photons detected by the used MCP is susceptible to small deformations. These deformations of the delay lines lead to an error in the extracted position of the events, as the recorded time delays between the signals propagating on the wires don't correspond to the expected position anymore. An example for an uncorrected MCP image is given in the left panel of Figure 4.5. The spectral lines projected onto the MCP by the reflective grating should be straight in reality but are displayed as tilted and curved due to this bending of the delay line wires.

In order to correlate the actual position of an incident photon and the apparent position in the data, a full map of the MCP needs to be constructed, displaying the deformation at any point on the detector.

To construct this map, first a series of measurements of a strong spectral line are taken. For each measurement, the height of the MCP in the setup is changed. Due to this change in height, the apparent line position moves across the detector in vertical direction as well. This apparent height difference between each measurement can be compared to the actual change of the height, which was set manually at the spectrometer by hand by turning a screw. As the vertical position of the detector is changed by the same distance in each step, the apparent height of the spectral feature on the MCP should move the same distance in each step as well. Deviations from this even spacing point towards delay line deformations in the y-direction of the detector.

Additionally, in reality the taken line is assumed to be perfectly straight, but will appear deformed in the data. This deformation indicates unintentional bending of the delay-line wires along the x-axis.

By comparing the assumed real and recorded apparent position in these measurements, the delay-line-deformation can be extracted along these spectral lines. By interpolating the extracted deformation in a last step, a full map spanning the whole MCP area can be constructed.

The data set consisting of the different measurements at different detector heights which was used to construct the map can be seen in Figure 4.6.

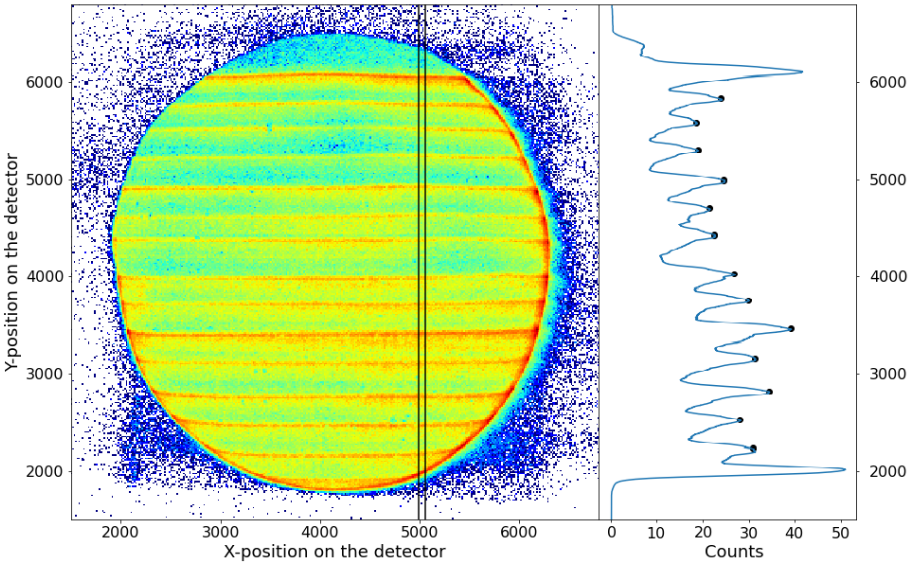

Figure 4.6: Left: Data set used for the construction of the shift matrix. Each of the strong visible lines stems from a measurement at a different MCP height, where the strong 13.5 nm light of tin is captured. Afterwards all these data sets are combined. **Right:** Projection of one data slice, as marked in the left panel. To each row, marked with a dot on the right, a gaussian fit is applied to determine the peak position.

This compiled dataset is then sliced into several strips according to the x-position of the data. Each slice is then projected onto the y-axis. One of these projections can be seen in the right panel of Figure 4.6. For each of those slices, a series of maxima is determined by applying several gaussian fits. These maxima then correspond to the apparent position of the spectral line in the different measurements at the specific x-position of the data slice.
By having detected a peak position for every line for several slices, overall a 2D matrix of maxima are obtained. This result can be seen in the left panel of Figure 4.7, with every spectral line recovered as a series of maxima in the individual slices. There you can see the slight variations of the line position with column due to the deformations.

For the construction of the correction template now one assumes, that the peaks in the final image shall be all part of evenly spaced, horizontal lines. Using this assumption first a correction for each of the peaks is found, by shifting the y-position of each peak to a position on the nearest straight line. The heights of those straight lines are given by the average height of each spectral line seen in the compiled data set in Figure 4.6. However, one needs a corrective value for each position on the detector, not only for the points recovered by the fits to the spectral line. Thus, one has to employ an interpolation method.
For this work, the choice for this interpolation was the Delauney triangulation [63], as this method has already been employed successfully for a different delay line MCP [10] to perform the same correction.
The locations of the maxima found in the prior step are now defined as a group of points in 2D-space. The MCP area is then divided into triangles, each span-

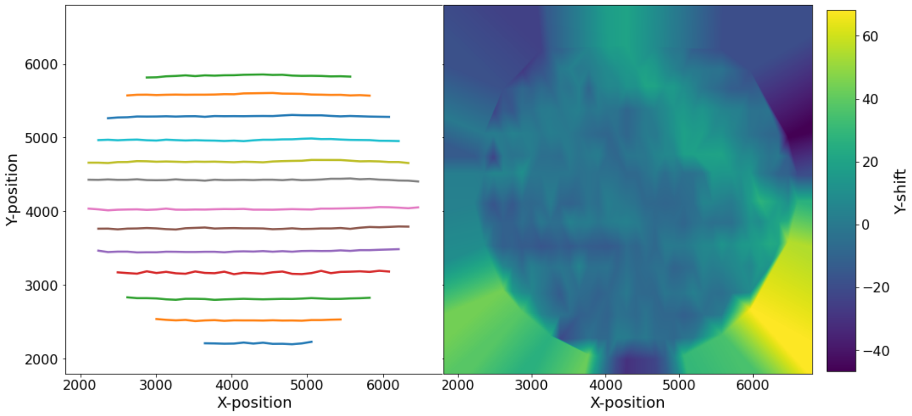

Figure 4.7: Left: Resulting peak matrix from applying gaussian fits to the slices as mentioned in the text. Each line describes a downsampled version of the spectral line in each of the measurements at specific MCP height. **Right**: Resulting shiftmatrix to correct for the MCP imperfections. The underlying Delaunay interpolation method is described in the main text.

ning three of those points. For each of them a correction value is already known, i.e. a shift in positive or negative y-direction to bring the maximum to the nearest straight line.
Without going into detail on how the triangles are chosen, the algorithm makes sure that there is never a fourth point inside the circumcircle of each of the triangles (pictured in Figure 4.8) and the largest angle of each triangle is to be minimized. These conditions make sure that the area gets divided into triangles of a compact shape and that there are never areas which get assigned to two triangles at the same time. Now one wants to determine the y-correction value of the arbitrary point (x, y), lying in a triangle spanned by three of the original points, P_0,P_1 and P_2 with the known y-correction values c_0, c_1 and c_2. The original detector-coordinates of the point, x and y, get transformed to be dependant on the location within the triangle. The new coordinate system assumes the origin to be one of the anchor points, say P_0 and the two adjacent triangle edges as the basis, whose length is set to 1 without loss of generality. Thus two new coordinates are assigned, (x_Δ, y_Δ). With these new coordinates, the correction is then calculated with

$$c(x_\Delta, y_\Delta) = c_0 + x_\Delta \cdot (c_1 - c_0) + y_\Delta \cdot (c_2 - c_0) \tag{4.2}$$

Thus, now over the whole area of the MCP, a correction value for every channel is defined. A final result of the correction map is displayed on the right side of Figure 4.7. Before analyzing data in the subsequent sections, each event had its y-position corrected using this template.

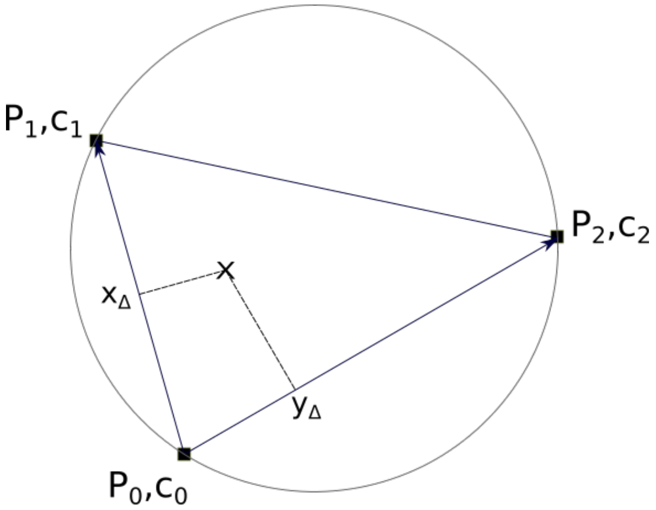

Figure 4.8: Example for the calculation of the interpolated shift. For an arbitrary point inside the triangle spanned by the anchor points P_1, P_2 and P_3, new coordinates x_Δ and y_Δ are assigned. Using equation 4.2 and the known correction values at the anchor points, c_1, c_2 and c_3, the arbitrary point can be corrected.

4.3 Correlation of Focus Voltage and Beam Current

As discussed in section 3.4, keeping the space charge inside the trap constant improves ion confinement and thus count rates during the experiment. As the space charge and electron density depend on both the electron energy and the beam current simultaneously, both are varied at the same time during each measurement cycle.

However, in the experimental setup, a control of the beam current is only possible by setting the voltage of the focus electrode in front of the dispenser cathode. This voltage is not directly proportional to the beam current, and thus the correlation between these two quantities needs to be determined.

A common relation, combining the focus electrode voltage and the electron beam current, was already shown in section 3.1.1 in equation 3.1, the perveance relation [61]:

$$I = kV^{\frac{3}{2}}$$

where k is a constant specific to the experimental setup at hand.

To determine the electron beam current as a function of the focus voltage, a measurement was conducted, in which the focus voltage was continuously varied while recording the electron beam current arriving at the collector. This was done with a cathode voltage of 90 V and heater settings of 8 V and 1.2 A as used in the main measurements on tin. Changing the heater settings would also change the constant k in equation 3.1, making the fit invalid for the main experiment. The data resulting from this measurement can be seen in Figure 3.1.

Applying the fit using equation 4.9 to this measurement, one gets the result

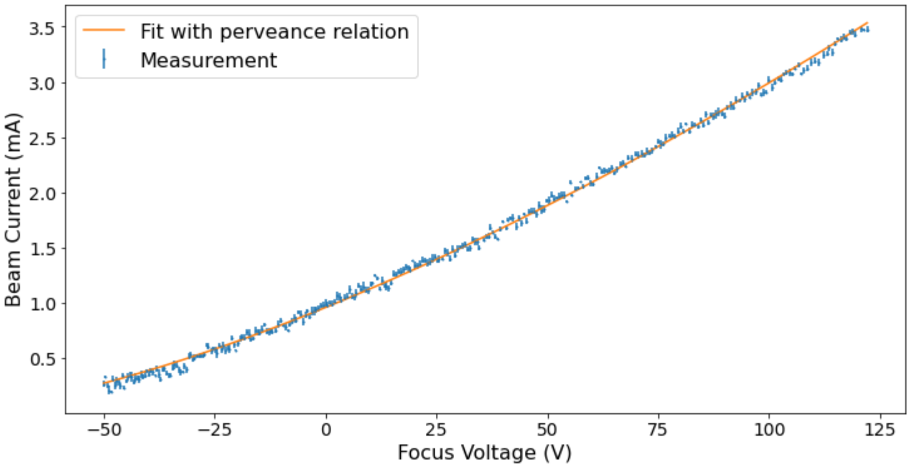

Figure 4.9: Fit to the results of the measurements of the beam current depending on the focus voltage using the perveance relation 3.1. The resulting constant for the given experiment results in $k = 1.1668 \cdot 10^{-2} \pm 5 \cdot 10^{-6} \frac{mA}{V^{\frac{3}{2}}}$.

shown in Figure 4.9 and a constant

$$k = 1.1668(5) \cdot 10^{-2} \, \frac{\mathrm{mA}}{\mathrm{V}^{\frac{3}{2}}} \tag{4.3}$$

Each data point was measured 5 times to get an estimation of the current fluctuation. For the fit the resulting average for each data point was used with the standard error of the average as a measure of uncertainty.

4.4 Oxygen Calibration

After optimizing the resolution of the EUV spectrometer in the previous sections, a calibration needs to be performed still, relating the dispersive channels of the MCP to an actual photon wavelength.
A natural choice for such a calibration spectrum for the observed EUV-region of 12 nm to 18 nm is oxygen, specifically O^{4+}. To produce high amounts of O^{4+} an electron beam energy of 210 eV and an electron beam current of 18.5 mA have been chosen. Overall two measurements at different cathode heater settings have been conducted. One with a very high heating, in order to inject additional barium into the trap, and one with a minimal heater setting to have as little barium as possible in the trap.
Due to the cathode being made up of a barium-tungsten matrix, there is always some emission of barium present, which correlates to the temperature of the cathode.
Thus a contamination of the trap with barium cannot be excluded with any settings and as there is a suspicion that highly charged barium has lines in the observed wavelength range, a variation of the barium concentration has to be done, to identify whether a line is emitted by barium or by oxygen. The two

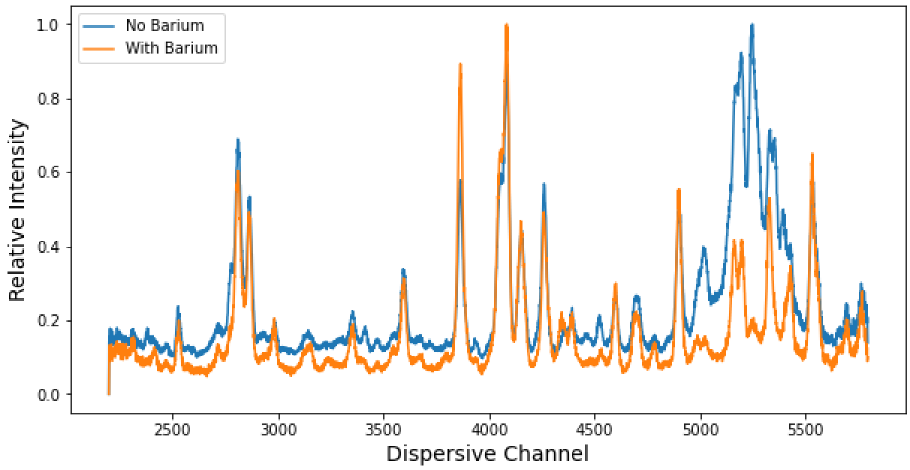

Figure 4.10: One dimensional oxygen calibration spectra, one with a high heater setting and one with a low heater setting. High heater settings lead to a strong contamination with barium, thus the resulting spectra are termed ”With Barium” and ”Without Barium”, for the respective heating.

recorded spectra can be seen in Figure 4.10.
By using spectral data of O^{4+} and several charge states of Barium, readily available on the atomic spectra database (ASD) of the National Institute for Science and Technology (NIST) [84], a line identification for a lot of the displayed lines is conducted. The experimental position of the lines given in dispersive channels is determined as the centroid of a gaussian least-square fit with a region of interest around the suspected line position. Uncertainties as given out as fit errors for the centroids of the gaussian fits are extremely low. Considering the shape of the lines on the MCP, as seen in Figure 4.5, even after conducting the linearization, the standard deviation of the lines as found with the gaussian fit is assumed as a more realistic uncertainty for the line position.
A couple of recorded lines, assumed to be from other charge states or emitted via transitions missing in the ASD, couldn't be identified. The used lines and their identifications are listed in Table 4.1. In cases where there are multiple tightly spaced lines, which aren't resolvable with the spectrometer in use, the wavelength error is assumed to stem from the distance between the line centroids of such blends.

With these line identifications, the calibration is being performed using a linear fit, as seen in Figure 4.11. The residuals depicted beneath are the result of quadratic addition of the experimental linewidth as given in the Table 4.1 converted to a wavelength uncertainty using the result for the linear dispersion coefficient a of the fit, given below, and the uncertainty denoted in the NIST database for the reference line:

$$\Delta\lambda = \sqrt{(a \cdot \sigma)^2 + (\Delta\lambda_{\mathrm{NIST}})^2} \tag{4.4}$$

Table 4.1: Identified lines in the calibration spectrum from Figure 4.10, with the line positions given in the first column. The wavelength data is taken from the atomic spectra database of NIST, with the primary source given in the respective column. Several identified lines are blended from multiple isolated lines, which can't be individually resolved. There the wavelength error is assumed to be the distance between the isolated lines.

Dispersive Channel	σ (Channel)	λ_{NIST} (nm)	$\Delta\lambda_{\mathrm{NIST}}$ (nm)	Charge State	Source
5533.3	11.8	13.0117	0.0005	Ba X	[16]
5427.1	9.6	13.180	0.003	O V	[110]
5327.34	9.4	13.3525	0.0025	O V	[110]
5195.5	13.5	13.5523	0.0001	O V	[12]
5162.57	13.8	27.2441	0.0009	O VI	[80]
5020.2	19.0	13.8109	0.0001	O V	[12]
4899.33	11.9	14.006	0.004	O V	[12]
4781.2	11.3	14.2122	0.0001	O V	[110]
4598.90	10.0	14.484	0.005	O V	[110]
4462.3	9.1	14.7263	0.0001	O V	[110]
4260.89	12.1	15.01	0.02	O V	[80]
4150.65	14.5	30.4507	0.0005	Ba VIII	[17]
4081.40	12.5	30.6407	0.0005	Ba VIII	[17]
4052.8	15.5	15.3952	0.0001	O V	[110]
3863.28	10.7	15.657	0.010	Ba V/ Ba VI	[76]
3351.8	12.4	16.6235	0.0001	O V	[12]
2979.0	11.8	17.0219	0.0001	O V	[12]
2862.69	10.7	17.2169	0.0001	O IV	[12]
2809.50	10.0	17.302	0.008	O VI	[80]

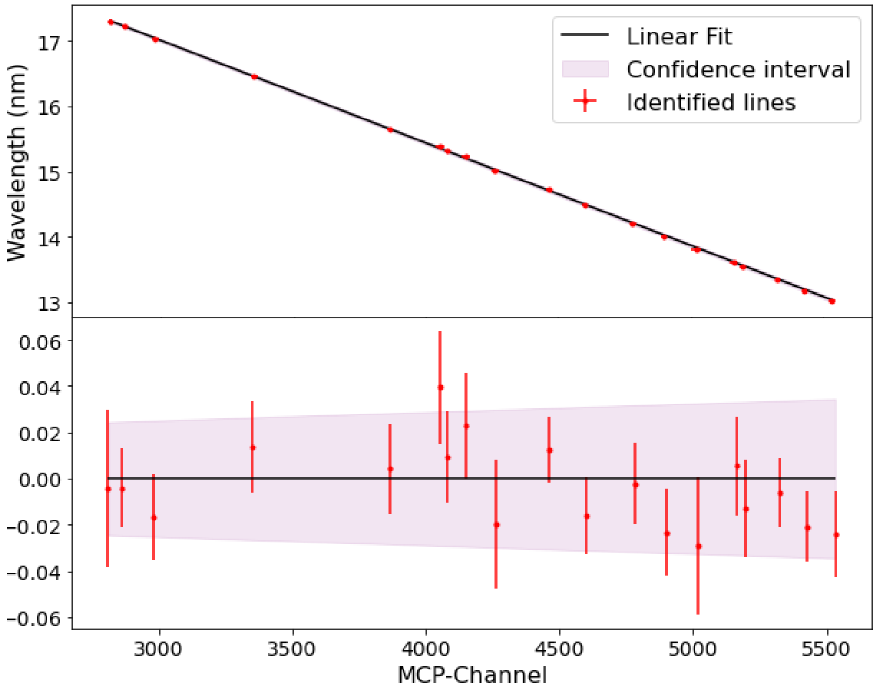

Figure 4.11: **Top:** Linear fit to relate the dispersive MCP channel to the wavelengths taken from NIST using the line identifications from Table 4.1. **Bottom:** Residuals of the fit.

In the residuals, displayed in the same Figure, a variation of the agreement of the fit to the experimental line position over large regions of the wavelength range can be seen. This variation is believed to still come from the imperfections of the used MCP, which weren't completely eliminated in the performed linearization explained in section 4.2.

Calibration fits of higher order were performed, as well as a calibration employing a sinusoidal function to take these long range variations into account. However there was no significant improvement in the agreement. Thus the linear fit is kept in the further analysis.
The results of this fit, relating dispersive channel n and wavelength λ used from here on out is:

$$\lambda(n) = -1.567(4) \cdot 10^{-3} \, \frac{\mathrm{nm}}{\mathrm{Channel}} \cdot n + 21.707(14) \, \mathrm{nm} \tag{4.5}$$

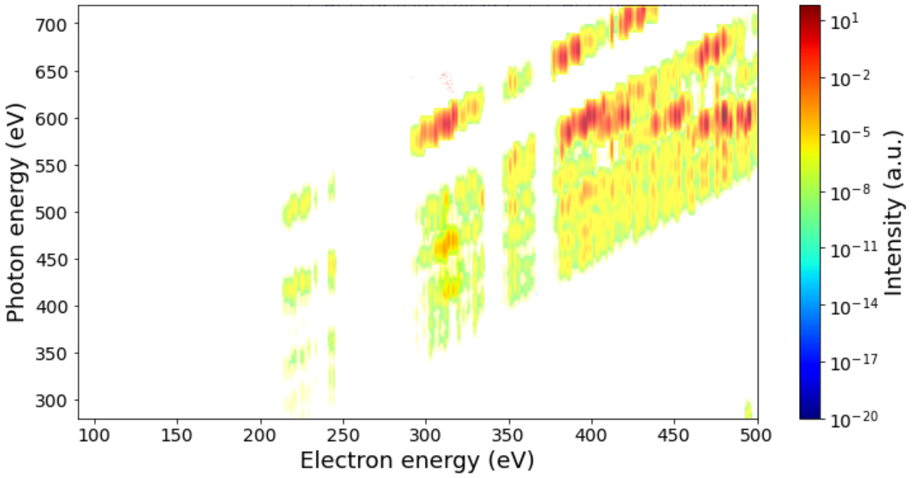

Figure 4.12: Two-dimensional spectrum relating electron-energy and photon-energy to the intensity of dielectronic recombinations. M-Nn resonances with $4 \leq n \leq 7$ of Sn^{14+} are shown. The found resonances are interpolated to a two-dimensional spectrum using a gaussian interpolation. Resonance positions and strengths calculated by Filipe Grilo.

4.5 Space Charge Determination

During the experiment, the kinetic energy of the electrons is set via the acceleration voltage between the cathode and the central drift tube, where the target ions reside, according to equation 3.2. The set energy must be corrected because of the space charge of the electron beam itself. As discussed in section 3.2, this space charge potential is proportional to $\frac{I}{\sqrt{E_e}}$. By varying this ratio, different space charges can be set up and the effect on the electron energy can be observed. Then the space charge can be extrapolated to the $\frac{I}{\sqrt{E_e}}$-value used in the main experiments and its effect corrected.

Ideal for such a study of the space charge is the observation of dielectronic recombination. As discussed in section 2.3, dielectronic recombination occurs only at a specific electron energy for each individual resonance, making it a perfect probe for the real electron energy inside the EBIT.

To find a feasible dielectronic resonance for this study, calculations using FAC are performed. The found resonances for the prominent tin charge states during the experiment have photon emissions outside the range of the EUV spectrometer, as their emission features have much lower wavelengths. A two-dimensional map for dielectronic resonances of Sn^{14+} found via FAC-calculations can be seen in Figure 4.12. The shown resonances are M-Nn resonances with $4 \leq n \leq 7$, meaning an electron is excited from the $n = 3$-shell to the $n = 4$-shell upon the recombination of an electron into the $4 \leq n \leq 7$-shell.

With these calculated dielectronic resonances in mind, the silicon drift detector set up at the EBIT is used to record an electron energy resolved X-ray spectrum. Multiple measurements on the position of the dielectronic resonances are conducted, each with a different current-energy-ratio (again, beam current and

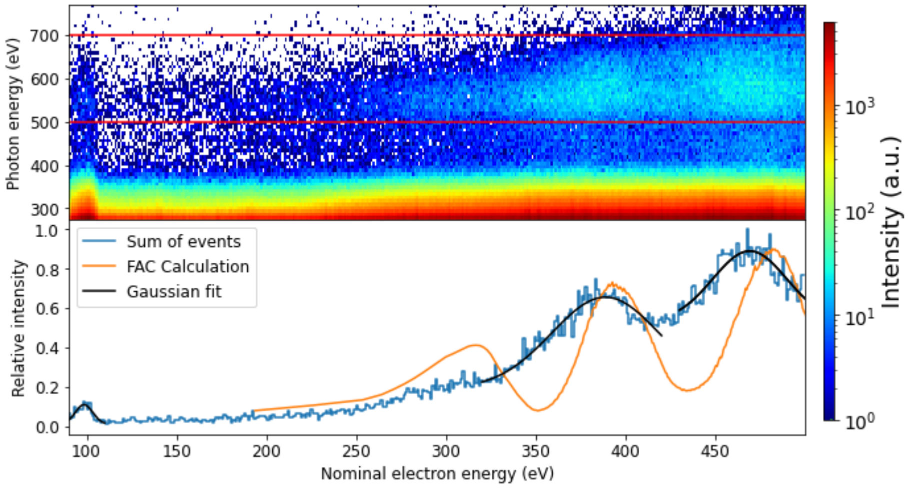

Figure 4.13: X-ray spectrum depicting the dielectronic resonances found to determine the space charge potential. The electron energy and photon energy ranges of the spectrum are the same as in the calculated spectrum in Figure 4.12. The region outlined in red is projected onto the electron energy axis to fit a gaussian profile to the dielectronic resonances and determine their resonance energy. A projection of the theoretical spectrum for the same photon energy slice is depicted as well, folded with a gaussian to take the experimental uncertainty of the electron energy into account.

electron energy are varied simultaneously as discussed in 3.4).
By comparing the apparent electron energy where the resonances occur for different ratios, one can construct a linear fit, according to equation 3.8, to find the constant of proportionality between the space charge and this ratio. Using this fit result, the beam energy in other measurements can be corrected depending on the beam current and energy applied there. As in the further measurements quantities like the drift tube settings, dump frequency of the trap and injection pressure are largely kept constant, the fit results are also valid there. If those settings would be changed drastically, the space charge compensating effect of the positive ions in the trap might also change, resulting in a different constant of proportionality, which would invalidate the fit done here.

The result of the analysis of a single of those DR-measurements can be seen in Figure 4.13. In that case the current-energy-ratio is $\frac{1.5\,\mathrm{mA}}{\sqrt{340\,\mathrm{eV}}}$.
The complete 2D spectrum with the photon energy in electronvolts on the y-axis and the nominal electron beam energy, as given as a readout value for the voltages supplied to the electrodes in the EBIT, on the x-axis, is displayed. The calibration of the photon energy is done using three lines from He-like oxygen and highly charged barium and applying a linear fit between the photon energies in channels as found with the detector and values as taken from NIST as before. Due to the low resolution of the SDD a precise calibration is not critical here.
A specific slice of the data, limiting the photon energy of the events, is selected, as can be seen in Figure 4.13, containing the dielectronic resonances to be investigated. The data in this slice is then projected onto the electron beam energy. For this projection several regions of interest for the electron beam energy are

defined, each containing one resonance. A gaussian fit is then applied to these regions to extract the central electron energy position of the resonances.
Overall, three prominent dielectronic resonances are found, to which those fits are applied. The different width of the three resonances is immediately apparent. While the resonance at an electron energy of 100 eV on the left side of the plot can be described by a gaussian with a standard deviation of

$$\sigma \approx 5\,\mathrm{eV}$$

the other two recorded resonances are much broader at round

$$\sigma \approx 15\,\mathrm{eV}$$

As the energy uncertainty of the electron beam is largely constant for different kinetic energies, this difference in apparent resonance widths suggests that the broader features are comprised of multiple tightly spaced resonances which can't be resolved individually. This makes it difficult to exactly define a center for the resonance, whose shift is to be observed for different current-energy-ratios.
The comparison to the calculated spectrum in Figure 4.12 shows that the two identified features at the higher electron energies are indeed comprised of many different MNN-resonances, even when only taking one charge state into account. Projecting the same photon energy region from the two-dimensional theoretical spectrum and folding the result with a gaussian to take the electron energy uncertainty in the experiment into account, shows the agreement between experiment and theory, except for a shift in electron energy.
Additionally, upon varying the electron density, the shape of the two peaks at higher electron energy changes. The reason for this might be, that these two features are comprised of resonances stemming from different charge states, not only Sn^{14+}, for which the dielectronic resonance positions were calculated. The change in electron density due to different current-energy-ratios then could be changing the charge state balance in the EBIT and thus the relative strengths of the blended resonances.
These two facts make both peaks at the higher electron energies unsuitable for a precise determination of the space charge. Therefore only the shift of the leftmost resonance is used to determine the space charge. Even though, this resonance could not be identified clearly, its linear shift in apparent position under varying the energy-current-ratio reveals, that it is indeed a DR-resonance.
The obtained resonance position of the left resonance at different current-energy settings can be seen in Figure 4.14. The position is determined as the centroid of the least square gaussian fit, with the error coming from the uncertainty of the fit result. The final linear fit to these resonance positions yields a slope of

$$5.7(3)\,\frac{\mathrm{eV}}{\mathrm{mA}} \cdot \sqrt{340\,\mathrm{eV}} \tag{4.6}$$

In the experiments discussed in the following sections 5 and 6, the ratio of set current and electron energy is

$$\frac{I}{\sqrt{E}} = \frac{4.5\,\mathrm{mA}}{\sqrt{340\,\mathrm{eV}}}$$

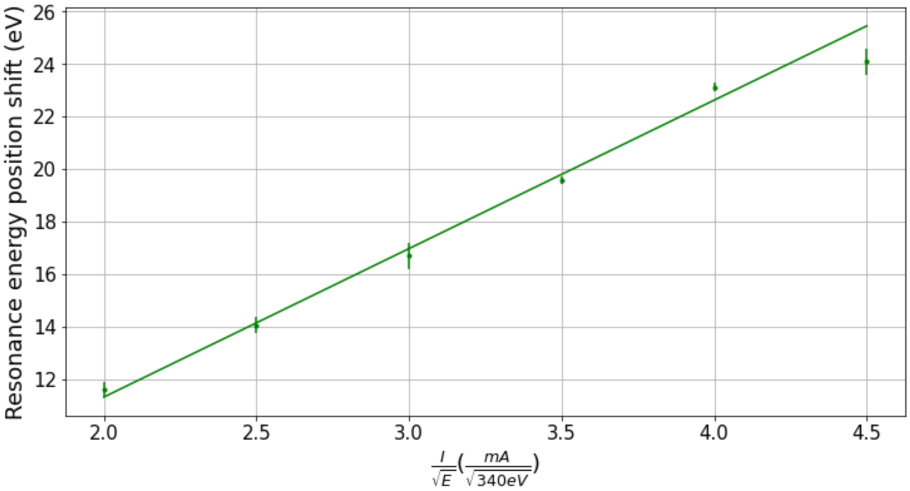

Figure 4.14: Shift of the leftmost observed dielectronic recombination resonance in terms of nominal electron energy depending on the electron beam current setting. The resonance position was determined as the centroid of a gaussian least square fit.

therefore the nominal electron energy during each of those measurements is corrected by

$$\Phi = 25.7(14)\,\mathrm{eV}$$

This subtraction will be done for all following data sets shown.
Similar fits have also been conducted for the other two resonances. However a linear fit didn't work as well for those resonance shifts, due to the changing shape at different electron densities. The observed shifts for these resonances were in the same order as for the left peak however, even if they could not be quantified quite as well. This hints at the fact, that the simultaneous variation of electron energy and current indeed keeps the electron density roughly constant.

Chapter 5

Slow Measurement

After optimizing the resolution of the EUV-spectrometer, determining the response of the beam current to the focus voltage and calibrating the wavelength as well as the electron energy, the measurements of highly charged tin can finally be analyzed. Two different types of measurements are presented. First a measurement without a breeding phase and with a slow energy variation is shown. Due to the slow variation, the ion population is constantly varied with the electron energy. From this, a spectrum of the pure ion charge states as well as ideal conditions for their production can be extracted. The second set of measurements is conducted according to the scheme described in section 3.4 in order to extract the contribution of multiply excited states to the EUV-spectrum of highly charged tin and will be presented afterwards. These measurements make use of the working points for the ion production determined in the slower measurement.

A practical way of determining the ideal electron energy settings for the production of each individual charge state, would be to employ an extraction beamline as used in [99]. By extracting the ions from the trap and separating them according to their charge to mass ratio, $\frac{q}{m}$, the relative populations can directly be ascertained and the spectrum decomposed for each energy setting.
As the used FLASH-EBIT isn't equipped with such an extraction beamline at the current time, a method needs to be employed, which yields the abundances of the individual charge states at the different energy settings by accessing only the recorded photon spectrum.
Similar to a previous measurement with FLASH-EBIT [92], the method of choice is non-negative matrix factorization (NMF) [78]. NMF is a popular method to reduce the dimensionality of data and identify underlying concepts of complex results.

The basis for this data reduction should be a two-dimensional spectrum, containing many different tin charge states, for which breeding settings and pure spectra are to be found. Thus a measurement is taken with a slowly varying electron energy and continuous recording of the EUV-spectrum. The rate for the variation is chosen to be 500 eV over 50 s, long enough to expect a steady state charge state distribution at every energy with a continuous shift in the dominant tin charge states in the trap. The complete set of EBIT settings can

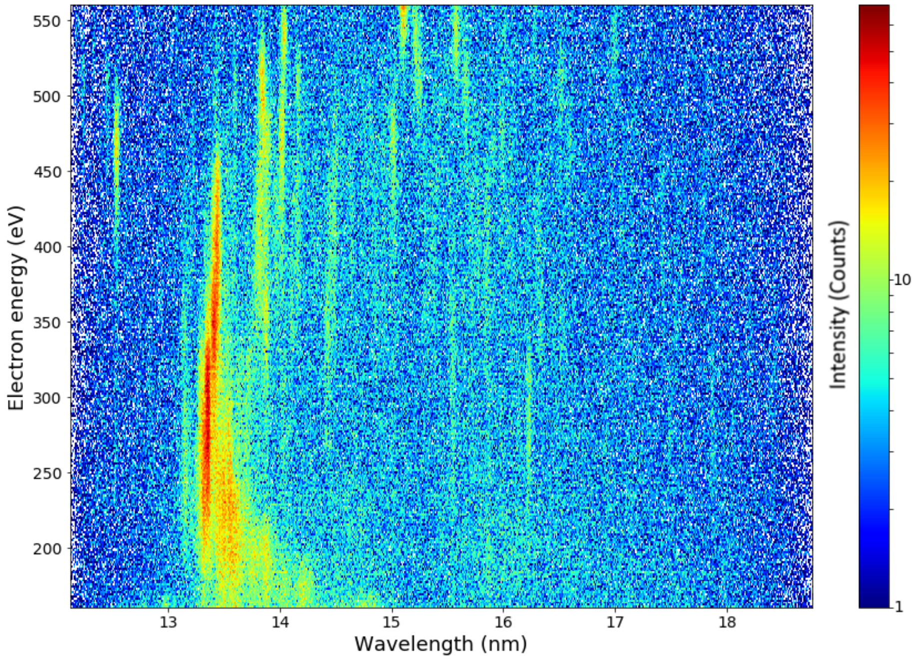

Figure 5.1: EUV spectrum of highly charged tin at different electron beam energies. The energy is varied slowly over 50 s to vary the charge states present in the trap during the measurement. The different spectral lines appearing at different electron beam energies reveal the shifting charge state distribution during the scan.

be seen in Table 5.1.

This slow scan with a variation of the charge state distribution is shown in Figure 5.1 with the photon wavelength on the x-axis and the electron beam energy on the y-axis. One can clearly make out several spectral lines appearing at different electron beam energies and fading out again at even higher energies. The spectral lines visible at each electron beam energy are governed by the charge state balance inside the trap at this energy. As the energy increases, ionization thresholds for higher and higher charge states are being met, as discussed in section 2.3.1 and the charge state distribution thus changes; more highly charged tin is produced. This means the recorded spectrum changes, as each charge state has a different characteristic atomic structure and therefore different spectral emissions. Let's assume, that for each electron energy E, the recorded EUV spectrum is the result of a linear combination of the spectrum of a set of c pure charge states. Then the intensity I in the a specific wavelength bin λ at a specific energy E can be reconstructed as

$$I(E, \lambda) = \sum_{i}^{c} a_i(E) I_i^{\text{pure}}(\lambda) \tag{5.1}$$

with the individual abundance $a_i(E)$ at electron beam energy E and the intensity of spectral emissions of charge state i at the wavelength bin $I_i^{\text{pure}}(\lambda)$. To recover this behavior for every electron energy and wavelength bin, the decom-

Table 5.1: EBIT settings used for the slow, charge state distribution varying, scan.

Quantity	Setting
Cathode Voltage	90 eV
Drift tube bias	10 eV - 500 eV
Energy ramp time	50 s
Current-energy-ratio	$0.242\,\frac{\text{mA}}{\sqrt{\text{eV}}}$
Trap depth	10 eV
Heater Settings	8.0 V, 1.2 A
Injection Pressure	$4.0 \cdot 10^{-6}$ mbar
Measurement time	270 000 s

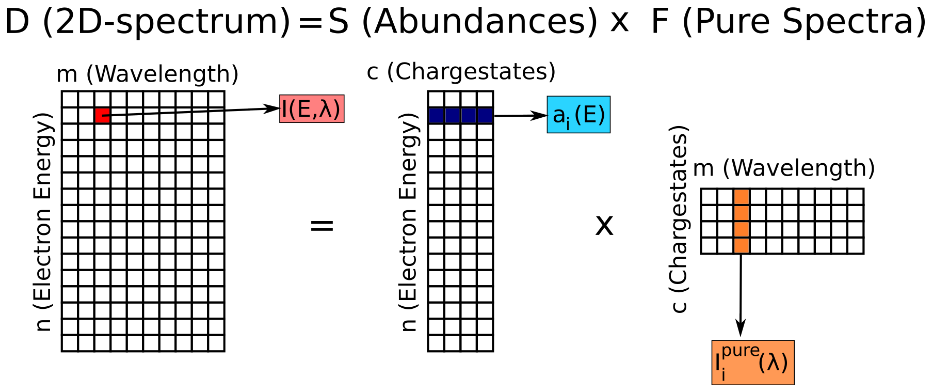

Figure 5.2: Visualization of the principle of the employed NMF. To represent the intensity at a specific electron energy and photon wavelength in the two-dimensional spectrum as a linear combination of pure spectra of the different charge states contained in the trap, the two-dimensional spectrum displayed in Figure 5.1 is treated as a matrix. This matrix can be split into two partial matrices, while asserting a specific number of charge states (c) to be present in the data. One of those matrices contains the electron energy dependant abundance for each of those charge states, the other one the pure spectra for each of them. Multiplication of these matrices recovers the original data, as then each entry represents one of those linear combinations.

position of the two-dimensional data into two partial matrices via NMF can be conducted.

The matrix D, representing the two-dimensional spectrum, with n rows of different electron energy and m columns of different wavelength, can be decomposed into the two matrices S and F, connected via the relation

$$D = S \times F \tag{5.2}$$

where then S must be of dimension $n \times c$ and F of dimension $c \times m$. By putting the additional constraint on the matrices D,S and F, that each entry shall be non-negative, the method of NMF is described. An efficient numerical algorithm then has to be employed, to calculate a possible pair of matrices S and F.

In the application to the two-dimensional spectral data of the experiment, the free parameter c is to be chosen in such a way, that it reflects the amount of different charge states produced during the experiment. Then each column of the matrix S describes for each of those c charge states the relative abundance inside the EBIT at each electron energy. Each row of matrix F describes the pure spectrum of those charge states. Non-negativity of the elements is a sensible constraint in this case, as negative abundances as well as emissions would be unphysical.

During the energy scan, the current is again varied to keep the electron density constant. As the selected minimum nominal electron energy during the fast measurements is chosen to be 90 eV as a compromise between event rate and extension of the spectra to lower energies, the electron density is set to be as high as possible at that cathode voltage of 90 eV while still having a beam pass through the trap. The highest reachable current for that cathode setting is 2.3 mA, which corresponds to a current-energy-ratio of $\frac{I}{\sqrt{E}} = 0.242 \frac{\mathrm{mA}}{\sqrt{\mathrm{eV}}}$. Setting higher focus voltages in favor of a higher current would lead to the beam hitting the focus electrode itself instead of passing it and is hence not possible.

The results of the NMF applied to this data can be seen in Figure 5.5, Figure 5.3 and Figure 5.4, displaying both the relative amount of ions being attributed to different charge states for every energy step during the measurement as well as the pure photon spectrum of these isolated charge states.

Overall the NMF yields the best results when imposing the condition $c = 14$ on the rank of the matrices, meaning traces of 14 different charge states are found in the measurement. Comparing the expected ionization thresholds for the different tin charge states as given in Table 2.3.1 to the electron energies during the scan suggests these 14 present charge states to be Sn^{7+} to Sn^{20+}.

To check the results of the performed matrix factorization, and verify the identification of the different charge states to the different entries of the matrices S and F, the extracted individual photon spectra are compared to measurements performed and published in [92]. This comparison is presented in Figure 5.3 and 5.4. Later on, FAC-CRM calulations are performed as well to determine the pure spectra of the different tin charge states and to give another comparison to the experimentally determined spectra, especially for charge states not observed in [92]. These theoretical results and the comparison to the pure charge states are given in the later section 7.

The comparison presented in Figure 5.3 and Figure 5.4 shows some significant differences in the deduced spectra to the published results, especially for the lower charge states. Additional lines are present in the deconvoluted spectra extracted in this work. One possible origin of these lines could be highly charged oxygen, as oxygen was introduced into the trap as it was contained in the used tin compounds. Still, the lines present in the experimental results of [92] are also found in this work. This circumstance supports the attribution of the different charge states to the individual entries of the NMF.

Another notable feature in the two-dimensional spectrum is the appearance of several strong lines in the wavelength range of 14 nm to 16 nm, which weren't as prominent in the prior measurements [92]. Using data from NIST, it is likely, that these lines again originate from oxygen, specifically O V, polluting the tin spectrum.

Apart from the pure spectra, the NMF also yields abundances for the charge

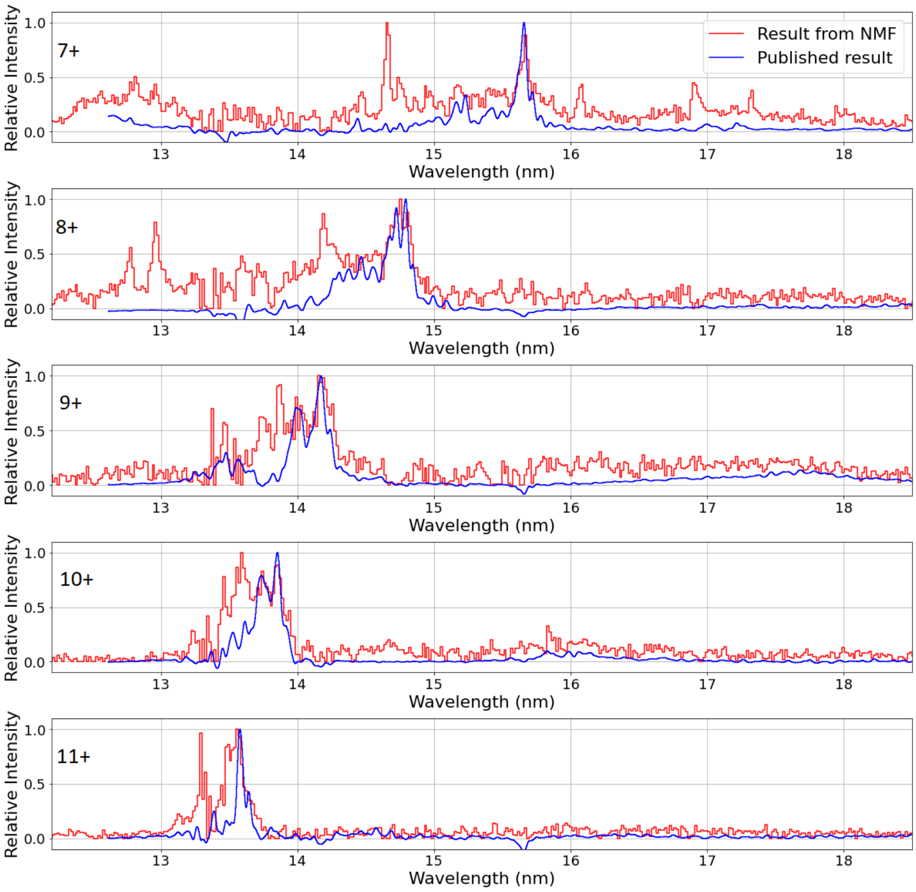

Figure 5.3: The pure spectra of the observed tin charge states between Sn^{7+} and Sn^{11+} during the slow energy scan. For comparison and identification of the charge states the results from the work in [92] are displayed as well.

states depending on the electron beam energy, as shown in 5.5. By evaluating these abundances, one can find the optimal working points for the breeding phase of the different charge states for the fast scans presented in the following section 6. Therefore, in Table 5.2, the maxima for the production of the individual charge states are given, as well as the corresponding production threshold for the charge state as given in [87]. These production thresholds are defined as the binding energies of the most weakly bound valence electron of the previous charge state in its ground state.

For several charge states the maximum population, as obtained via the performed NMF, is attained before the energy of the beam electrons reach the ionization energy to produce the next charge state from the atomic ground state. A possible explanation for this would be a significant contribution of long lived metastable states to the electronic state balance of the ions. If there are metastable states with an energy above the atomic ground state, the next charge state can be produced by ionization from those metastable states, decreasing

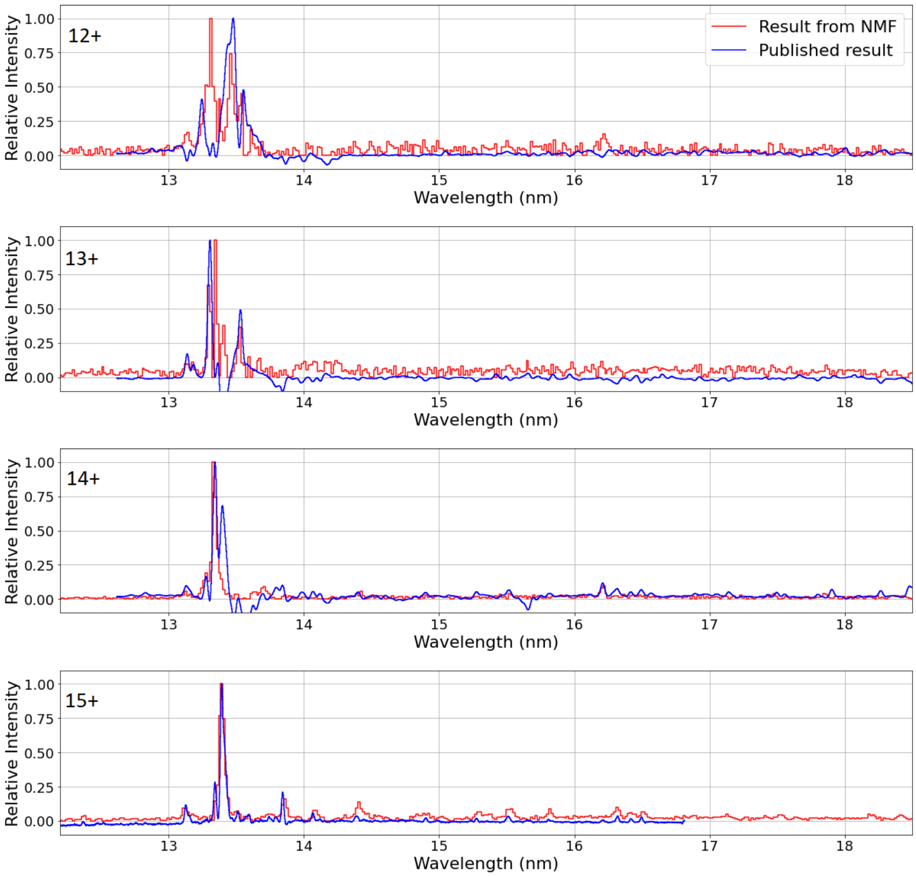

Figure 5.4: The pure spectra of the observed tin charge states Sn^{12+} and Sn^{15+} during the slow energy scan. For comparison and identification of the charge states the results from the work in [92] are displayed as well.

the needed electron kinetic energy by their energy level.
To confirm this suspicion, the collisional radiative model of FAC is used to calculate the relative populations of the different electronic states at the conditions during the slow scan. For each charge state, an individual calculation is performed. As an input for the electron energy for the calculation, the electron energy of the maximum yield for the respective ion, given in Table 5.2, is used. The results of these calculations are shown in Figure 5.5, as additional production thresholds, resulting from production via metastable states of the previous charge state. Several states at roughly the same energy values are grouped together and their respective populations added up. The relative populations are displayed by the opacity of the marker.
An overview of the calculated metastable states with their corresponding populations is given in Table 5.3.

There, only metastable states with a relative population of at least 10 % or high energies have been listed. For the other charge states not listed here, notable metastable populations are found with level energies of only up to 10 eV, some-

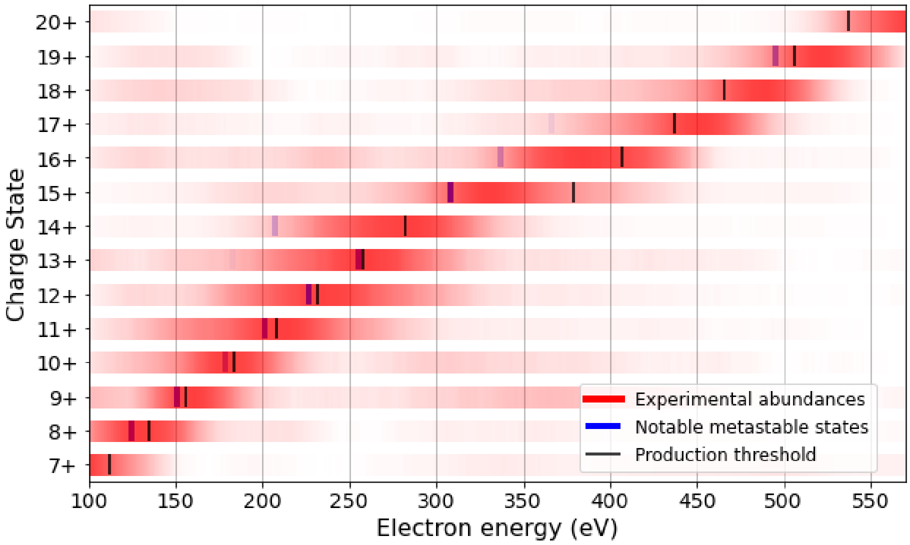

Figure 5.5: Relative abundance of the different identified charge states depending on the electron beam energy, displayed by the opacity of the corresponding line. The production thresholds as given in the NIST database [87] are displayed. Additionally the production thresholds including notable metastable states from the previous charge state are displayed, with the opacity of the marker stating the relative population of those metastable states.

times though with significant populations, even higher than the ground state. They might be responsible for shifting the abundance maximum slightly below the expected production threshold.

Apart from the maximum abundances for several charge states being lower than expected from the ionization potentials given in the literature, there is another peculiar feature visible in Figure 5.5. For several charge states, additional traces are found at much different electron energies than where the maximum abundance is found. For example, in the case of Sn^{9+}, the population seems to increase at higher energies again, long after the maximum abundance has been reached and the population was already depleted. As there is no sensible explanation for such a behavior, and such a feature occurs for several different charge states, it has to be assumed, that those features come about due to spectral lines from different charge states being so close to each other, that they become indifferentiable in the experiment. Then spectral markers from one charge state could be misinterpreted in the deconvolution as markers from another charge state. This problem of the method has to be kept in mind in the further analysis.

In the following fast measurement cycles, designed to find the contributions of multiply excited states to the spectrum of highly charged tin and explained in section 3.4, the energies given in Table 5.2 as the energies of maximum abundance are used for the breeding phase of the measurements to produce the desired charge states.

Table 5.2: Found settings for the highest yield of the specific tin charge states via the results of the applied NMF.

Charge State	Electron energy (eV)	Expected production threshold (eV)
7+	< 100	112.9
8+	126	135.0
9+	160	156.0
10+	179	184.0
11+	213	208.0
12+	233	232.0
13+	259	258
14+	285	282
15+	332	379
16+	384	407
17+	468	437
18+	488	466
19+	521	506
20+	570	537

Table 5.3: Notable calculated metastable states, from which premature ionization at lower electron energies than expected can take place. For each charge state for which such metastables are found, the ground state as well as the metastable states are given with their respective populations, energies compared to the ground state and level symbols in jj-coupling as defined in 2.2.3. Only metastable states with an energy of at least 10 eV or a population of at least 10 % are listed.

Charge State	Energy (eV)	Population	State
13+	0.0 eV	33.6 %	$([4d-]^{1}_{\frac{3}{2}})_{\frac{3}{2}}$
	1.6 eV	54.5 %	$([4d+]^{1}_{\frac{5}{2}})_{\frac{5}{2}}$
	72.2 eV	3.6 %	$([4p+]^{3}_{\frac{3}{2}}[4d+]^{2}_{4})_{\frac{11}{2}}$
	76.2 eV	3.3 %	$([4p+]^{3}_{\frac{3}{2}}[4d-]^{1}_{\frac{3}{2}}[4d+]^{1}_{\frac{5}{2}})_{\frac{11}{2}}$
14+	0.0 eV	31.6 %	$([4p+]^{4}_{0})_{0}$
	69.5 eV	29.2 %	$([4p+]^{3}_{\frac{3}{2}}[4d+]^{1}_{\frac{5}{2}})_{4}$
	69.3 eV	14.5 %	$([4p+]^{3}_{\frac{3}{2}}[4d-]^{1}_{\frac{3}{2}})_{3}$
	73.2 eV	8.7 %	$([4p+]^{3}_{\frac{3}{2}}[4d+]^{1}_{\frac{5}{2}})_{3}$
15+	0.0 eV	84.8 %	$([4p+]^{3}_{\frac{3}{2}})_{\frac{3}{2}}$
	71.7 eV	7.0 %	$([4p+]^{2}_{2}[4d+]^{1}_{\frac{5}{2}})_{\frac{9}{2}}$
	69.0 eV	3.4 %	$([4p+]^{2}_{2}[4d+]^{1}_{\frac{5}{2}})_{\frac{7}{2}}$
	72.0 eV	3.2 %	$([4p+]^{2}_{2}[4d-]^{1}_{\frac{3}{2}})_{\frac{7}{2}}$
18+	0.0 eV	71.4 %	$([4p-]^{2}_{0})_{0}$
	10.6 eV	26.3 %	$([4p-]^{1}_{\frac{1}{2}}[4p+]^{1}_{\frac{3}{2}})_{2}$

Chapter 6

Fast Measurements

With the best settings for the production of each tin chargestate now known, the measurements to extract the contributions of multiply excited states to the EUV-spectrum of highly charged tin could be conducted, charge state by charge state.

Instead of the slow energy variation like in the measurement discussed in the prior chapter, now the measurement cycle is divided into two parts as described in section 3.4. First, a constant electron beam energy is set to produce the wanted ions, according to the working points found in the previous slow measurement. Then a fast energy sweep is conducted on a short enough timescale to keep the charge state balance approximately constant. During this fast sweep, the EUV spectrum is recorded at every energy step. At each different electron energy, only energetic levels may be populated which can be reached through the means of electron collisional excitation by the beam electrons. These excited states can then radiate via spontaneous photon emission. Therefore, changes in the spectra at specific energies hint at the presence of levels with those energies. Specifically, these changes would consist of new spectral lines appearing or existing line strengths being amplified, as discussed in section 2.3.2. The relative intensity of the spectral lines at different electron energies would then also give a measure of the relative transition strengths of the radiative decays from the different excited states found this way. This way the relative contributions of multiply excited states to the EUV spectrum of highly charged tin shall be found.

Overall, several measurements employing this method are taken. The difference each time is the energy during the breeding phase, with the goal of producing and investigating different tin charge states with each measurement. The breeding energies for the production of the desired charge states were determined in the previous section 5 with the energies where maximum abundances were detected, taken as the breeding energies now.
In line of this reasoning, measurements for the analysis of Sn^{11+}, Sn^{12+}, Sn^{13+}, Sn^{14+} and Sn^{15+} are performed, with breeding energies of 213 eV, 233 eV, 259 eV, 285 eV and 332 eV, respectively.
Details on these fast measurements can be taken from the Tables 6.1 and 6.2.
Here the method for the data analysis is first described for the measurement

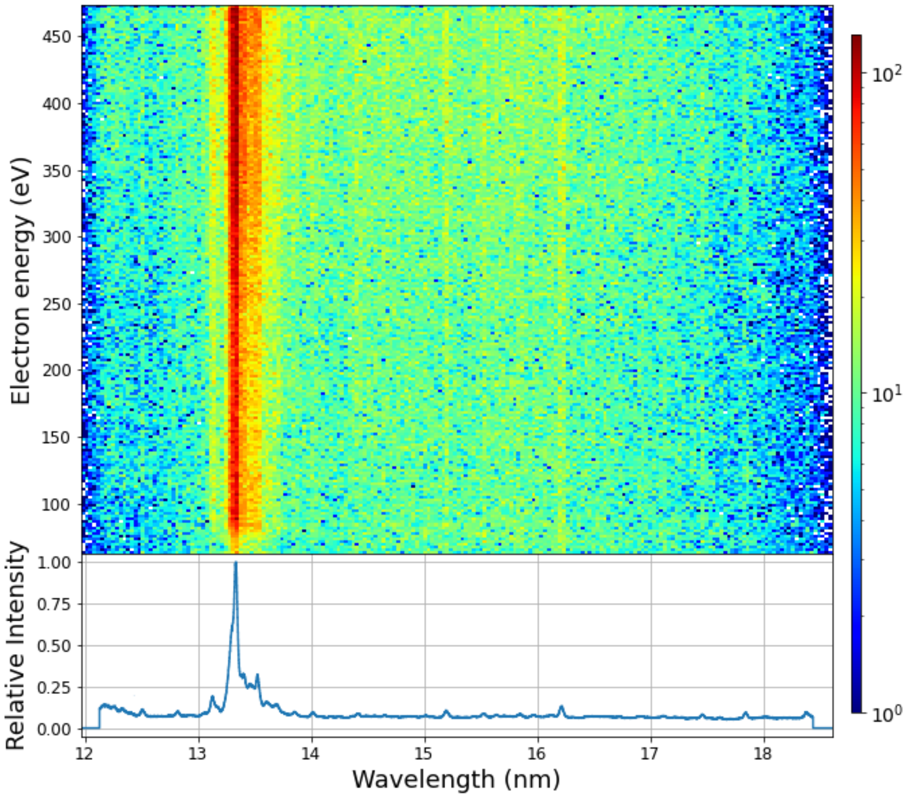

Figure 6.1: Two-dimensional spectrum of the measurement focused on Sn^{14+} with the projection onto the photon wavelength below. The color scale represents the detected events for each wavelength-electron energy-combination.

focused on Sn^{14+} (breeding energy of 285 eV). For the other charge states only results will be discussed afterwards in less detail, as the procedure of analyzing the data is analogous for each measurement.
First of all, to have an overview of the conducted scan, a two-dimensional spectrum for that measurement is shown in Figure 5.1, relating the electron energy and photon wavelength to the intensity of the recorded radiation. Additionally, a projection of all events onto the photon wavelength axis is performed, to see the location of the spectral lines recorded during the measurement.
There the difference in recorded spectrum between this measurement scheme with a fast energy sweep and the slow energy variation presented before is immediately apparent. In the two-dimensional spectrum recorded during the slow measurement shown in Figure 5.1, one clearly sees spectral lines appearing at

Table 6.1: Common EBIT settings during the five conducted fast measurements.

Current-Energy-Ratio	0.242 $\frac{\text{mA}}{\sqrt{\text{eV}}}$
Drift tube voltages	3—5—5—10—0—10—5—0
Ion Dumping	Every 20.3 s for 1 s @ 200 eV central DT voltage

Table 6.2: EBIT settings varied between the fast measurements.

E_{breed}	Duration	Breeding cycle time	Scanning cycle time	Energy range	Injection Pressure
213 eV	143 h	0.8 s	0.2 s	65 eV - 475 eV	$3.2 \cdot 10^{-6}$ mbar
233 eV	339 h	1.9 s	0.1 s	65 eV - 475 eV	$3.0 \cdot 10^{-6}$ mbar
259 eV	308 h	0.8 s	0.2 s	65 eV - 275 eV	$3.5 \cdot 10^{-6}$ mbar
285 eV	457 h	1.9 s	0.1 s	65 eV - 475 eV	$4.0 \cdot 10^{-6}$ mbar
332 eV	186 h	0.8 s	0.2 s	65 eV - 475 eV	$3.2 \cdot 10^{-6}$ mbar

certain energies and fading out again at higher energies, marking the change in the charge state distribution inside the trap during the measurement cycle. Now, due to the short time durations in the measurement scheme, the charge state distribution should be constant, which is checked in the next section. Therefore the lines are much more persistent throughout the different electron energies and mostly just vary in their intensity slightly. On the other hand, this already hints at the contributions of multiply excited states observed in this work being pretty weak.
In the following projections of events in different regions of interest onto the photon wavelength and electron beam energy are conducted to extract the charge state distribution during the measurement, produce a catalogue of contained spectral lines and ultimately find the contributions of multiply excited states to the EUV spectrum of highly charged tin via an analysis of the electron collisional excitation cross section.

6.1 Charge State Distribution Determination

As a first step in the analysis of the fast measurements, the two different sides of the scanning phase (see section 3.4), the upwards energy scan and the downwards energy scan are compared. The idea of the fast measurement cycles employed here is to keep the charge state balance in the trap constant with the one charge state in question dominating. However, if the energy ramps turn out to be to slow, the charge state balance will shift, as seen in the slower measurement. An indicator for such a charge state shift would be an asymmetry in the recorded spectrum during the two energy ramps. If during the first ramp the ions produced in the breeding phase would be lost to recombination processes, they would be missing in the second half of the scan, resulting in a different spectrum. Such a shift in recorded spectra between the scanning phases is also an indicator for the presence of long-lived metastable states, produced during the breeding phase and decaying over the course of the scanning phase. As discussed in 2.3.3, the intensity of radiation, emitted via a decaying metastable state, should be describing an exponential decrease if the state isn't populated anymore during the scanning phase. Thus such lines would also be much more prominent during the first half of the scan.

One example for a comparison of the two halves can be seen in Figure 6.2. There a projection of all events contained in the region of the main line for the measurement focusing on Sn^{14+} as a function of time in the measurement

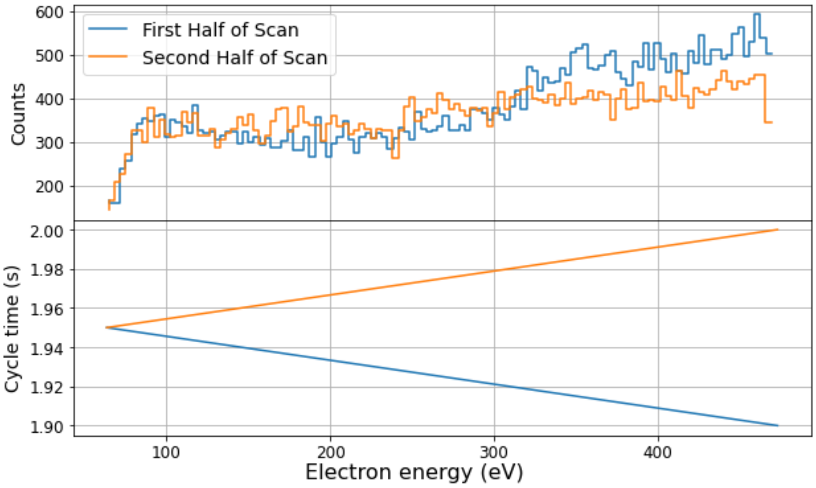

Figure 6.2: Comparison of the two halves of the scanning phase of the measurement focused on Sn^{14+}. The breeding time in this case is 1.9 s and each energy ramp duration 50 ms. **Top:** Projection of the events contained in the main line around 13.4 nm (13.2 nm - 13.6 nm). **Bottom:** Electron energy to time relation during the two phases of the scan.

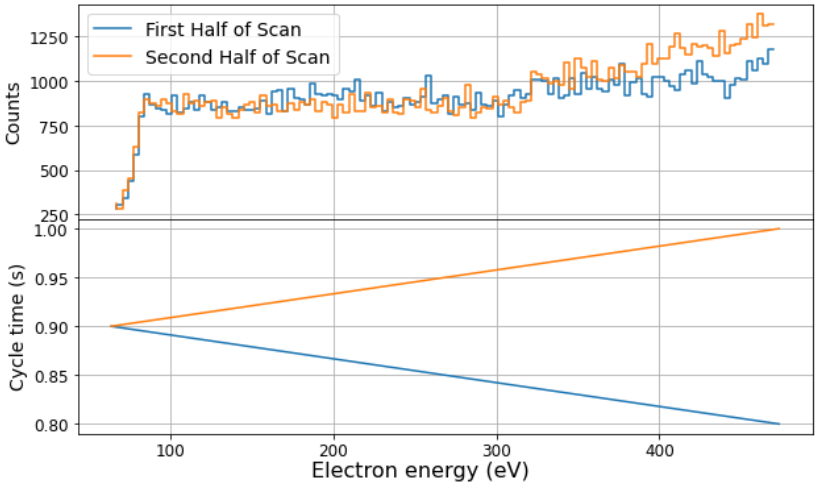

Figure 6.3: Comparison of the two halves of the scanning phase of the measurement focused on Sn^{11+}. The breeding time is 0.8 s and each energy ramp duration 100 ms. **Top:** Projection of the events contained in the main line around 13.4 nm (13.2 nm - 13.6 nm). **Bottom:** Electron energy to time relation during the two phases of the scan.

cycle is displayed. The emissions recorded during the two halves of the scan are indeed not completely identical. Instead, at higher electron energies, the second scanning phase has a slightly lower countrate. As the high energy regions of both scans occur at the very beginning and the very end of the scanning phase, respectively, effects changing the ion population or the population of long-lived metastable states during the energy sweep show their biggest effect there.

To avoid this population change, even shorter scanning phases may be implemented. However, in the case presented here, the scanning phase already only attributes to 5 % of the measurement time. This leads to very long measurement times being needed to collect significant signal during the scanning phase. Hence this slight asymmetry is accepted. The asymmetry is also highly dependent on the measurement. The measurements at different breeding energies and therefore different charge state distributions showed different degrees of signal asymmetries, with the found asymmetries in the other four measurements being similar to the one in the presented measurement, or even lower. Another example of this check for asymmetry is given in Figure 6.3, where the time dependant intensity of radiation in the main line region between 13.2 nm and 13.6 nm in the measurement focusing on Sn^{11+} is shown. There the second half of the scan actually shows higher line intensities, with the relative difference in intensity being in a similar range to the other shown example. Overall the found asymmetries for the different measurements are between the two cases shown.

This difference in charge states over time might hint at strong dielectronic resonances with resonances in the scanned electron energy region. Then, even a short duration at that energy would lead to many ions recombining, due to the high transition rates discussed in section 2.3, significantly altering the charge state balance down the line.

After examining the changes to the charge state distribution over time, the actual charge state balance during each of the measurements is of interest. Setting the breeding energy to the values found in section 5 of course doesn't leave only the desired charge state in the trap. At the very least lower charge states will also populate the EBIT. Their presence is a prerequisite for the appearance of the wanted charge state, as the charge breeding inside the EBIT is based on the successive electron impact ionization of those lower ionization stages.

To quantify this charge state mixture in each of the measurements, a comparison of the complete spectrum of each fast measurement, such as the projection given in the lower panel of Figure 6.1, with the pure spectra obtained via the NMF in section 5 is performed.

A weighted sum of the individual pure spectra X_i is produced:

$$X_{total} = \sum_i a_i X_i \tag{6.1}$$

with the individual abundances a_i. Many possible total spectra are generated by varying the individual abundances. Here the pure spectra of Sn^{9+} to Sn^{15+} are taken into account. Higher charge states are discarded, as the breeding energy isn't sufficient in any of the fast measurements to produce those. Lower charge states should also not play an important role, as their maximum production as found by the NMF in section 5 is reached at much lower energies, and thus their populations should be pretty low here.

The most fitting composite curve is then obtained by finding the sample spectrum with the minimum squared distance to the spectrum of the fast scan. Again, the squared distance being defined analogous to equation 4.1 as

$$\chi^2 = \sum_i^n \left| X^i_{\text{exp}} - X^i_{\text{total}} \right|^2 \tag{6.2}$$

where one sums over the n recorded wavelength bins in the measurement and the total generated spectrum.

Initially, the weights for the individual contributions are completely randomized, between values of 0 and 1. Then, for each iteration, χ^2 is calculated, and the iteration with the weights, minimizing this value is taken as a basis for the generation of successive composite spectra. For the successive iterations a new set of weights is randomly drawn from a normal distribution around the optimal values as found in the previous trials. If this new trial again minimizes χ^2, the used weights in that trial would become the new basis. This way this fit method converges for a high amount of trials.

After generating 10^5 trial spectra, the relative abundances minimizing χ^2 are recorded for each measurement as an estimation of the charge state balance. To attribute for uncertainties in this fitting method, the method was conducted ten times for each fast measurement, with the results being averaged over and the error of the mean given as an uncertainty. The charge state contents found this way are compiled in Table 6.3.

Table 6.3: Found charge state balance for the measurements with different breeding energies employing the method described in the main text. All values in the table are given as percentages.

E_{breed}	Sn^{9+}	Sn^{10+}	Sn^{11+}	Sn^{12+}	Sn^{13+}	Sn^{14+}	Sn^{15+}
213 eV	6.3(4)	6.4(3)	22.5(9)	26.8(7)	12.9(9)	5.0(11)	19.9(9)
233 eV	4.6(3)	4.5(6)	23.8(16)	24.4(15)	21.8(14)	9.7(13)	11.1(16)
259 eV	2.2(3)	1.5(4)	19.9(22)	34.4(23)	14.9(20)	7.6(17)	9.5(16)
285 eV	5.1(5)	1.9(4)	8.4(7)	26.2(18)	14.8(27)	35.8(11)	7.8(10)
332 eV	4.9(4)	2.1(5)	7.0(9)	26.2(11)	14.1(16)	30.1(11)	15.6(7)

The ideal combined spectra are overlaid with the spectra measured during the fast scans in Figure 6.4 with the corresponding charge state populations as given in Table 6.3 as insets.

The results of this charge state balance analysis show that the mixture of charge states still seems to be quite large. Deconvolving the spectrum this way to reach a final conclusion is difficult however because of the multitude of spectral lines appearing close to each other in different tin charge states. Therefore, it is also likely that the mixture is being overestimated here, and the actual relative contributions of the desired charge states are much higher. This problem of the method is especially clear for the case of the spectrum taken with a breeding energy of 213 eV. There a large contribution of Sn^{15+} is found, even though the actual production maximum estimated with the NMF of that charge state is around 332 eV, more than 100 eV more. This misidentification probably stems from a misinterpretation of lines emitted by Sn^{9+} as lines emitted from Sn^{15+}.

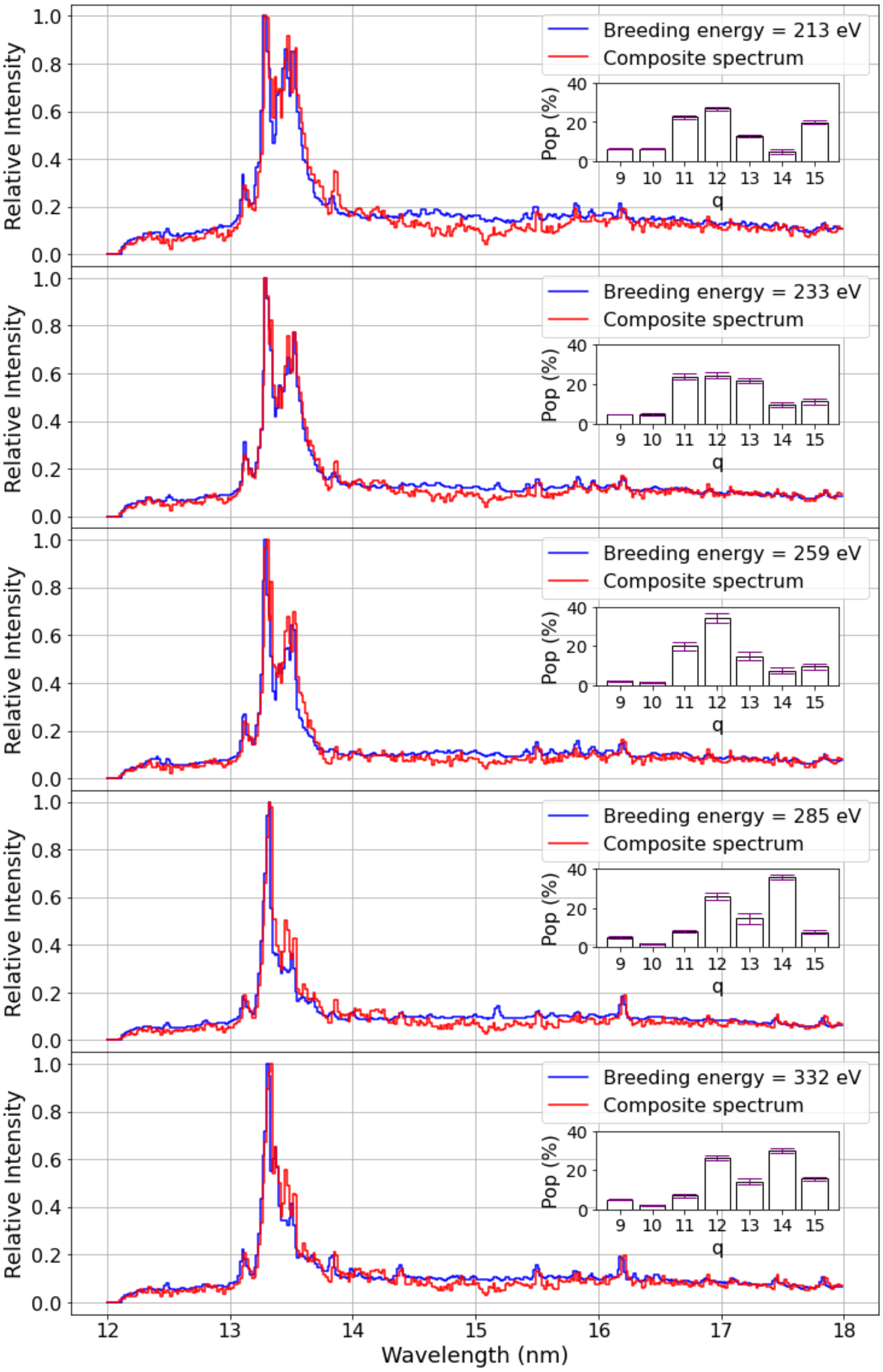

Figure 6.4: Complete spectra of the fast measurements with different breeding energies. The composite spectrum generated as discussed in the main text, yielding the best fit to the measured spectrum, is overlaid. The resulting ion populations found with this fit are displayed as an inset in the five different panels.

Already in the prior section, in Figure 5.5, one can see the experimentally determined abundance of Sn^{15+} rising in parallel to that of Sn^{9+}, even when the energy is still far to low to produce Sn^{15+}.
To alleviate this problem, the method is employed an additional time, only including the spectral data between 14 nm and 18 nm. The idea behind limiting the wavelength range taken into account is, that the lines of different charge states overlap especially in the main line region between 13 nm and 14 nm. This line blend makes attributing the wrong charge state to the found lines more likely. On the other hand the spectral lines in the higher wavelength region are more separated and resolved individually and thus it should be easier to attribute them to the right charge state.
The problem with cutting the main line region out of this determination, however, is that some charge states lack significant features for their identification outside of that main region. Additionally, the overall statistical significance for spectral lines is lower in those regions as a result of lower count rates there.
In the end this second try does not yield a fundamentally different result from the first try with the complete spectrum. There is still a presence of Sn^{15+} extracted for the measurements with low breeding energy. For a comparison the populations extracted with the smaller spectral region are given in Table 6.4.

Table 6.4: Found charge state balance for the measurements with different breeding energies employing the method described in the main text. Here only events between 14 nm and 18 nm are used for the fit.

E_{breed}	Sn^{9+}	Sn^{10+}	Sn^{11+}	Sn^{12+}	Sn^{13+}	Sn^{14+}	Sn^{15+}
213 eV	3.9(3)	11.9(6)	28.4(5)	23.7(12)	10.7(13)	8.6(12)	12.8(19)
233 eV	3.3(3)	11.6(5)	27.1(11)	24.7(9)	12.7(11)	6.4(15)	14.3(15)
259 eV	1.9(2)	11.1(9)	24.8(10)	25.9(16)	18.3(13)	5.9(10)	12.1(14)
285 eV	1.0(2)	7.1(3)	17.7(9)	23.9(10)	19.2(15)	21.9(7)	9.3(16)
332 eV	1.6(1)	6.7(5)	13.0(5)	21.6(10)	18.1(9)	22.8(10)	16.3(11)

Still, independent of the selected wavelength region, a shift in the contained charge states is observed between the measurements. This shift behaving as expected, as a higher breeding energy will lead to a higher average charge state. This means, that the investigation of the different charge states can still be done by looking at the difference between the observed spectra during the different measurements. In the end making statements about the combined prevalence of the contributions of multiply excited states for the charge states from Sn^{11+} to Sn^{15+} can also still be made.

6.2 Spectral Line Catalogue

Now that the approximate charge state distribution for each of the measurements is known, the analysis of the recorded spectra to extract the contributions of multiply excited states can start. Here again, the analysis is discussed in detail for the measurement with a breeding energy of 285 eV, focusing on Sn^{14+} with the overview over the two-dimensional spectrum presented at the

beginning of the chapter in Figure 6.1.
The central idea behind the fast measurements is the extraction of the behavior of the recorded lines' intensity with increasing electron beam energy, as a direct probe of the underlying atomic level structure and transition strengths. Therefore in a first step the lines contained in each scan, which are to be investigated, are catalogued.
For this purpose of identifying the spectral lines, the total projection seen at the top of Figure 6.5 is sliced into several wavelength regions. In these slices, a sum of gaussian functions and a constant background is fitted to the experimental data using a least squares fit. A slicing of the data into several regions is necessary due to computational limitations and accuracy of the fits. As there are in total around 50 identifieable lines in each spectrum, fitting all of them simultaneously results in computation times which are to long. Fitting the data with gaussian functions instead of voigt profiles [45] is sufficient, as the extracted width of the spectral lines is far greater than the expected natural linewidth. For the observed spectral lines, the highest calculated transition rate is about $f = 10^{12}\,\frac{1}{\mathrm{s}}$, which leads to a linewidth of

$$\Delta E = \frac{\hbar}{\tau} = f\hbar = 4\,\mathrm{meV} \Rightarrow \frac{\Delta E}{E} = \frac{\Delta\lambda}{\lambda} \approx 4.34 \cdot 10^{-5} \tag{6.3}$$

for a line at $\lambda = 13\,\mathrm{nm}$ this would correspond to a wavelength uncertainty of

$$\Delta\lambda_{\mathrm{nat}}(\mathrm{FWHM}) = 0.0005\,\mathrm{nm}$$

Meanwhile the observed linewidth is around

$$\sigma = 0.015\,\mathrm{nm} \rightarrow \Delta\lambda(\mathrm{FWHM}) = 2\sqrt{2\ln(2)}\sigma = 0.035\,\mathrm{nm}$$

So even for the strongest lines, which are to be expected, the natural linewidth is still far smaller than the observed linewidth. Therefore a gaussian fit is justified.

One example of such a data slice with the corresponding fit can be seen in the lower part of Figure 6.5, where the region around the main line of Sn^{14+} is selected. There the individual gaussians, as well as the sum of the gaussian curves are displayed. The overlap between the different spectral lines is apparent, facilitating the need for a fitting algorithm with many gaussian functions.
As the width of the indivdual gaussian functions is determined by the experimental apparatus and plasma conditions, the width is fixed for all of the fits to the spectral lines, after being determined once for an isolated spectral line. For the measurement discussed here this width is fixed at

$$\sigma = 0.015\,\mathrm{nm} \tag{6.4}$$

to obtain the best possible fit. This spectral width corresponds to a resolving power of around

$$R = \frac{\lambda}{\Delta\lambda} \approx 400 \tag{6.5}$$

in the wavelength region of 12 nm to 18 nm, with $\Delta\lambda$ being the full-width-at-half-maximum.

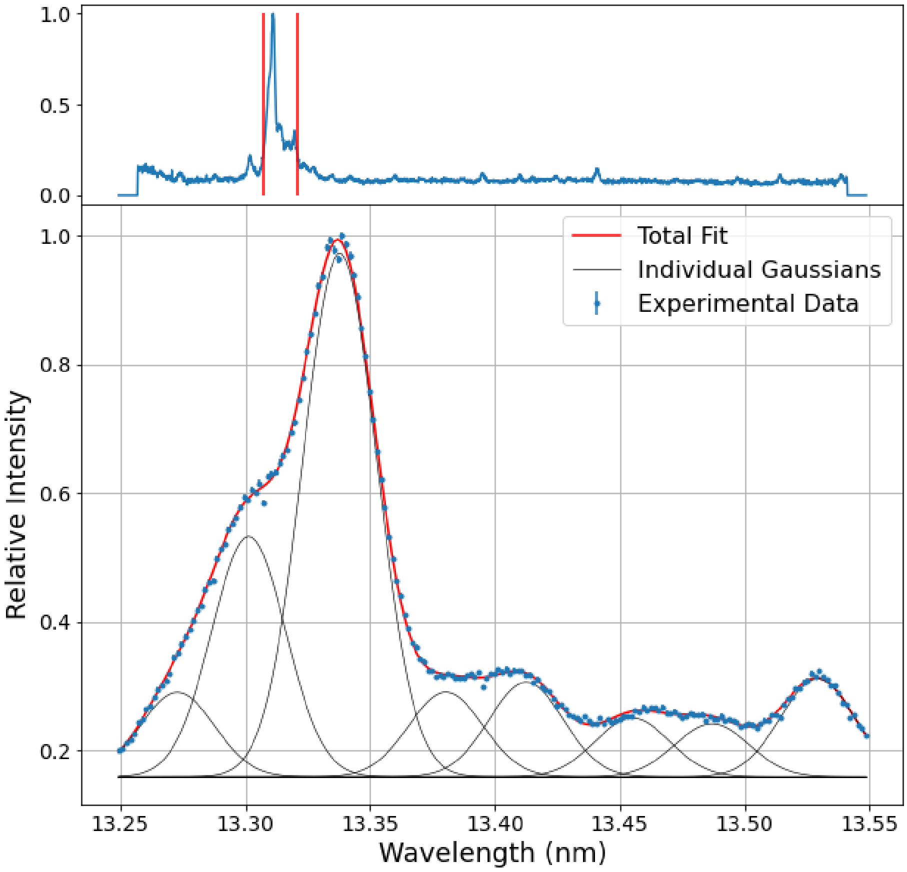

Figure 6.5: Example of the performed line identification. The total spectrum (top) was sliced into several regions where the individual lines overlapped. Then a sum of gaussians was fitted to these slices, including a constant background. The width of the gaussian profiles was given by the apparatus and experimental conditions and thus constant for all curves.

The complete results from these line catalogues can be looked up in the appendix. Overall hundreds of spectral lines are found, but the line identification proves extremely difficult due to many different overlaid charge states and relatively large uncertainties in line positions due to the systematic uncertainties as a result of the uncertainty in the conducted calibration.
The statistical errors presented in the appendix are the uncertainties for the line centroids from the gaussian fits. Additional systematic wavelength errors come from the uncertainty of the wavelength calibration given in section 4.4. These systematic errors are relatively high at

$$\Delta\lambda_{\mathrm{sys}} \approx 0.04\,\mathrm{nm} \tag{6.6}$$

on average, presumedly due to the imperfections of the MCP in the used spectrometer. These imperfections could not be completely eliminated with the linearization in section 4.2. They outweigh the statistical errors originating from

the fit uncertainties by far and are in an order of magnitude of the linewidth.
As expected after the charge state analysis done before, many lines appear in all three fast scans, due to same ionic species being present in each of the three measurements. However, the lines are present in different intensities, due to differences in the relative abundances between the measurements. Some lines far removed from the main region show a very strong dependence on the breeding energy and thus the produced charge state.
A concrete line identification to specific transitions is not conducted in the scope of this thesis, as the uncertainties of the line positions and obtainable accuracy of the corresponding calculations, combined with the immense number of closely spaced energy states makes that very difficult

6.3 Electron Collision Excitation Cross Section Determination

After analyzing the integrated photon spectrum and extracting all the line positions, the changes in the spectrum under the varying electron beam energy in the scanning phase, as a probe for the contribution of multiply excited states, are now to be discussed.

At any point during the fast scans, only excited states should be populated, for which the electron beam energy is sufficient for a production via collisional excitation. At the production thresholds, where the electron beam energy reaches the energy of an excited state, the observed spectrum should change, as new excitation and deexcitation pathways are opened up. Keeping in mind the density of states shown in Figure 2.4, there should be certain electron energies, where the spectrum changes drastically.

In a first step, to check for such drastic changes, depending on the energy of the electrons exciting the ions, the spectra recorded for three different electron energy regimes are presented. These regimes are chosen according to the density of states shown in 2.4. One projection includes all events recorded at electron energies up to 120 eV, supposedly only containing spectral lines from transitions between singly excited states and the ground state. The second projection contains all events between 120 eV and 180 eV, which should consist of transitions initiated from singly, as well as from doubly excited states. The last projection contains all events recorded at an electron energy of at least 180 eV, which should contain transitions involving triply excited states as well. The corresponding density of states can be seen in Figures 2.4 and 7.1. The three spectra are shown in Figure 6.6 in the case of the measurement focusing on Sn^{14+}.

At a glance, differences are not apparent between those three spectra. Intensities of the different lines only change slightly. This already shows, that if contributions of multiply excited states appear in the present experiment, they must be rather weak. As no strong new lines can be made out appearing at higher electron energies, their influence would also mostly manifest in the amplification of existing lines. Thus the intensity as a function of the electron energy is being considered in a next step.

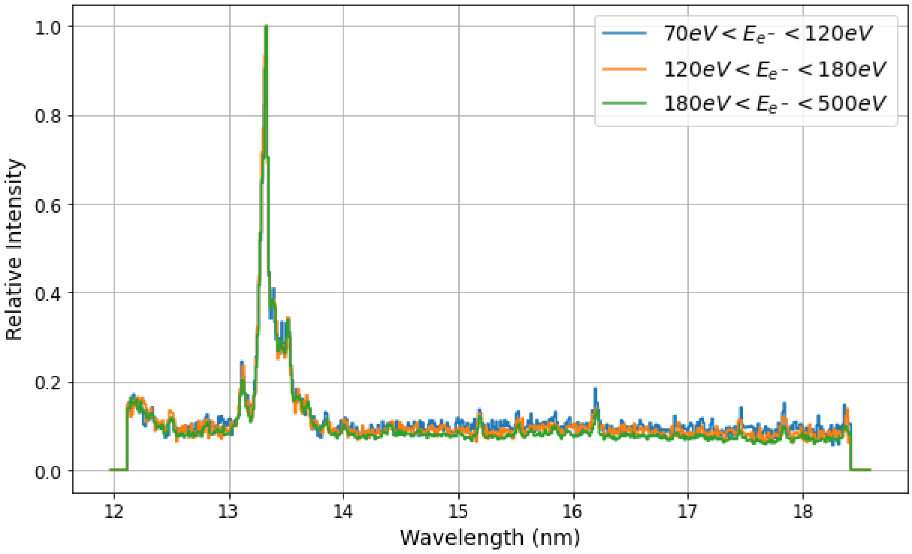

Figure 6.6: The EUV-spectrum during the measurement focusing on Sn^{14+} for three different electron beam energy windows. Those energy windows are selected in a way, that they each include one additional energy block displayed in Figure 2.4, namely singly, doubly and triply excited states. Differences between these spectra could then point towards lines originating from transitions initiated by those energy blocks.

Note that the relative intensities depending on the electron energy presented in the following are divided by the varying electron current at the different electron beam energies, to get a quantity, which is proportional to the electron impact excitation cross section, as the excitation rates, on which the intensities depend on, will always be proportional to the electron flux, see 10. Thus the relative intensities, which are proportional to the collision excitation rates, should now also be proportional to the collision excitation cross sections.

To give an overview of the evolution of the relative intensity, depending on the electron beam energy, first a projection of all events onto the electron beam energy axis is shown in Figure 6.8.
As was outlined in section 3.4, the relative intensity of the recorded radiation during the fast scan should be proportional to the populating rate of all radiatively decaying upper levels if those upper levels decay sufficiently quickly and in the recorded wavelength range. All those different excitation channels should have populating rates defined by the collisional excitation cross section approximated by the Van Regemorter relation 2.43, which is electron energy dependent. These assumptions would result in electron energy dependant relative intensities as depicted in Figure 6.7, where three upper states are assumed, which are visible via radiative decays.

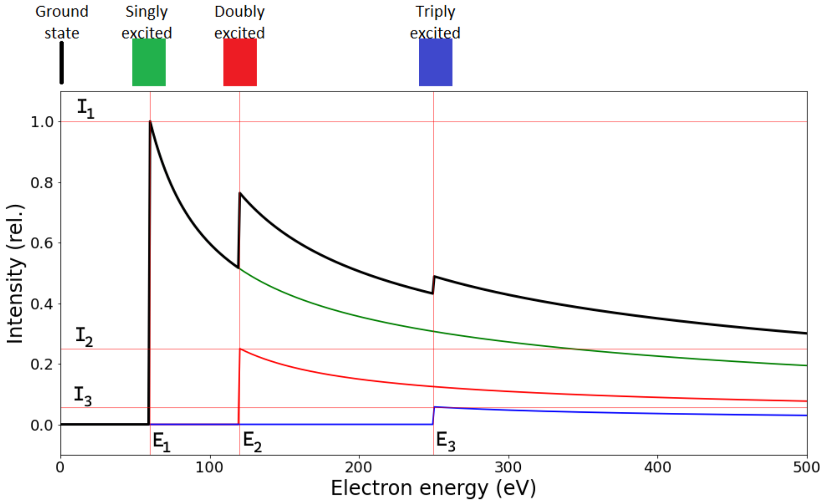

Figure 6.7: The relative intensity in a certain wavelength region during the fast scan is expected to vary according to the population rate of the upper states, which radiate in that region, due to electron impact excitation. If several upper states contribute in that region, then the relative intensity depending on the electron energy can be displayed as a sum of Van Regemorter curves (three in this example), defined in equation 2.43. Due to the different energies of the upper states, these curves will have different energy thresholds (E_1, E_2, E_3). Furthermore they will lead to different contributions to the recorded intensity (I_1, I_2, I_3), from which a quantity can be extracted, that is proportional to the oscillator strength f_{if} of the excitation channel as seen in equation 6.10 later. Such functions are used to fit the experimental intensity variations, to extract energies and radiative contributions of the multiply excited states.

One can immediately identify some of these predicted features of the relative intensity. At low energies, there is a steep rise in the relative intensity, due to quickly more states being available via collisional excitation as upper states for photon transitions. Due to the location of this initial onset of the intensity, these upper states can already be presumed to be the previously termed singly excited states. From the maximum intensity at around 90 eV, the intensity drops with increasing electron beam energy, in agreement with the empirical results of the Van Regemorter formula 2.43 for the behavior of the electron impact excitation cross section introduced previously. There are multiple slight plateaus in this decrease of the intensity, for example at 125 eV and 180 eV. These humps hint at new upper states being available at these electron energies, therefore increasing the excitation rates, and thus the relative intensity again. Due to the electron energies at which these plateaus are observed, these upper states might be the sought after multiply excited states. At even higher energies, starting around 250 eV, the relative intensity isn't decreasing anymore. Instead it fluctuates around a constant value, with several apparent peaks. This could also hint at further upper states being available for collisional excitations at these upper energies.

The errorbars for the electron energy projections introduced here, as seen for example in Figure 6.8 are assumed to come from poissonian statistics [60]. As for each channel on the detector and for each electron energy setting individual

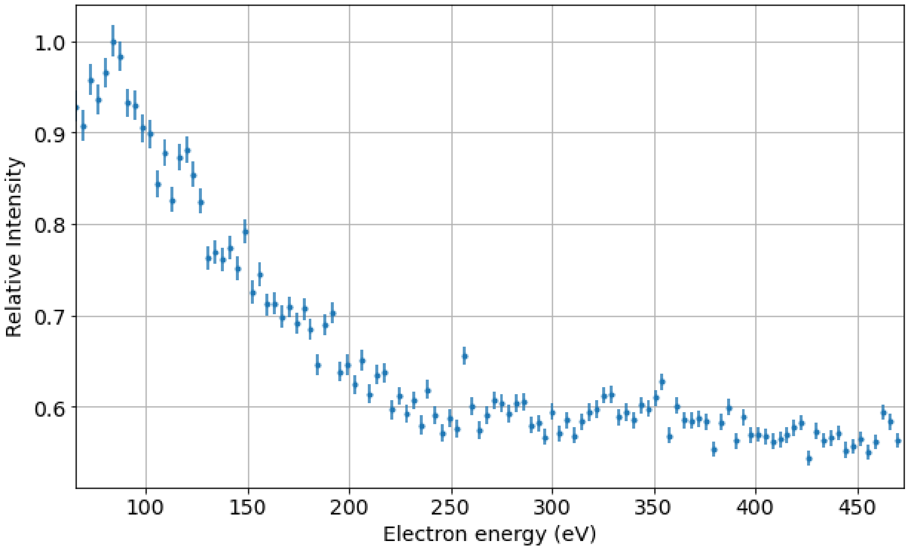

Figure 6.8: Projection of all recorded events onto the electron energy axis. The data has been weighted according to the current at each electron energy bin to obtain a signal proportional to the collisional excitation cross section.

photon events are counted, the uncertainty of the sum of counted events N can be assumed as

$$\Delta N = \sqrt{N} \tag{6.7}$$

for the raw experimental data. When later on weighting this data, adding or subtracting signals, gaussian error propagation [86] is performed throughout the analysis to preserve this error estimation.

So far, from the shape of the shown overview, it is not directly clear, at which exact energies multiply excited states might start to contribute to the spectrum and to which degree. This is due to many different upper states radiating in the observed wavelength region. As each of them have different energy levels, any sharp thresholds for radiation production, which might signal their presence are smeared out.
As different excited states are expected to radiate at different wavelengths, to better understand the contributions of the different state ensembles, the complete two dimensional spectrum in Figure 6.1 is sliced into many smaller wavelength regions. For each of those smaller regions, the projection of all events onto the electron beam energy is conducted to obtain the electron energy dependent relative intensity, which is assumed to be proportional to electron impact excitation rates. These regions themselves are chosen in such a way, that ideally they only contain one previously observed spectral line from the compiled line catalogues. However, for many very weak lines, the resulting projection shows no sufficient signal to conduct the fit. Hence also several lines are grouped together in those cases.

To determine the energy levels and relative contributions to the spectrum for

the different excited states now quantitatively from these relative intensities, a specific fitting algorithm is constructed. This algorithm is applied to the individual projections.
The basis for this fitting algorithm is the assumed connection between the populating rates of the different excited states, which can radiatively decay in the observed wavelength range, and the recorded intensity. Therefore, as a fit function, a sum of Van Regemorter relations is taken, each one with a different onset and maximum value. A resulting example fit function with pre-determined parameters is shown in Figure 3.11 in the prior section 2.3 and in Figure 6.7 here. As an input, the amount of Van Regemorter curves making up the fit are given, as well as a range of relative intensities and energy thresholds as initial parameters. The number of Van Regemorter curves should then correspond to the number of different excited states radiating in the observed wavelength region, assuming the individual radiation onsets can be individually resolved. The thresholds will be corresponding to the energy level of the excited state and the relative intensity will be proportional to the oscillator strength of the excitation process as seen later on in equation 6.10.
The singular Van Regemorter curves are summed up, to lead to a combined fit. Each energy bin is folded with a gaussian of a predefined width of at least 5 eV. This assumed width comes from the experimental data as given in section 4.5, as this was the minimal width of the observed dielectronic resonances and can thus be taken as an estimate for the uncertainty of the electron beam energy in the experiment. The width of the individual thresholds may be larger, as several tightly spaced energy levels are expected to contribute at the same time and the individual threshold of each isolated level can not be expected to always be resolved.

The methodology, which is employed to find the number of Van Regemorter relations and the initial parameters for the fit for each of the slices is explained for the example of the wavelength region from 13.32 nm to 13.37 nm from the measurement focusing on Sn^{14+}. First, the selection of the wavelength region in this specific case is made, as can be seen Figure 6.9, to contain one strong spectral line. The events in this wavelength region are then projected onto the electron energy axis and can be seen in each of the panels of Figure 6.10.
Due to the multitude of starting parameters, whose choice is crucial for a functioning fit, and the number of contained thresholds being unclear a priori, the fit was built up threshold by threshold.
Each of the panels in Figure 6.10 contains the experimental data, as well as a fit with multiple Van Regemorter relations, with the residuals displayed below each time. As can be easily seen there, adding additional curves with a different onset to the fit, changes the behavior of the fit function for all energies above the onset. Hence the modeling starts at the lowest threshold each time.
Each of the panels, which include the residuals, also include

$$\chi^2_{red} = \sum_i \frac{(y_{exp} - y_{fit})^2}{\Delta y \cdot n} \tag{6.8}$$

as a measure of the goodness of the performed fit. A value near one indicates a good fit, a value below one indicates an overestimation of errors and a value above one hints at an insufficient fitting model or underestimation of the errors.

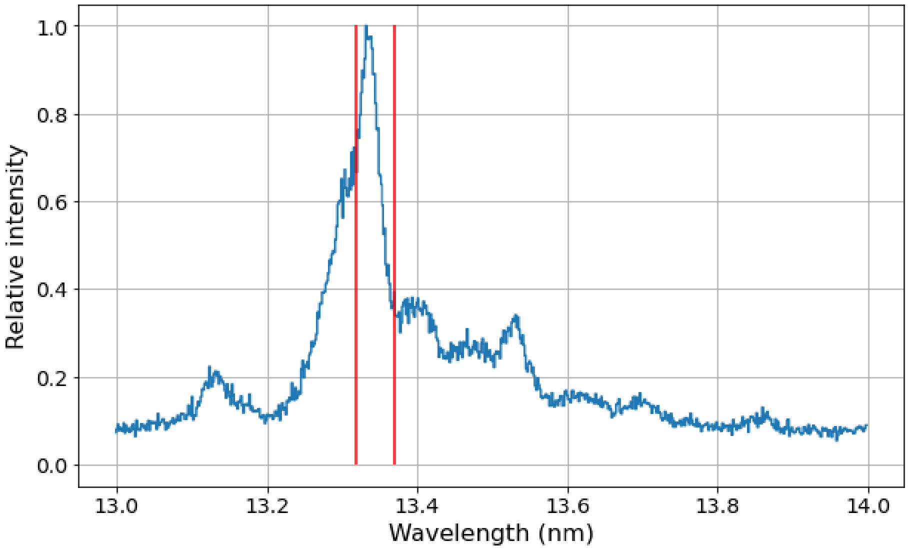

Figure 6.9: Zoom-in on the wavelength region containing the main line in the Sn^{14+}. The wavelength region containing the events for the sample electron beam energy projection is marked with red lines.

As can be seen, the value of χ^2_{red} improves drastically with the introduction of additional thresholds from a value of

$$\chi^2_{red} = 5.89$$

to a value of

$$\chi^2_{red} = 1.63$$

Hence, it can be safely assumed, that the description of the extracted relative electron collision excitation cross section by only the initial threshold is insufficient and additional contributions are really needed to describe the intensity variation of the spectral line with the change of the supplied electron energy.

When choosing the number of thresholds for the fit, a good indicator for the introduction of an additional Van Regemorter curve is the shape of the residuals. As mentioned before, the contributions of higher lying states will only affect the shape of the intensity curve above their threshold. Therefore, if the residuals are increased beyond a certain energy value, compared to their value at lower energies, this might signal the presence of a threshold at the energy, where this step occurs. In addition to the multiple Van Regemorter-curves, the fit function also consisted of a constant, attributing for electron energy-independent background radiation.

Upon introducing the needed amount of Van Regemorter curves for the fit, their energy thresholds can be extracted, as well as the relative amplitudes. In this example, for Sn^{14+} in the region of 13.32 nm to 13.37 nm, the fit results are listed in Table 6.5. The intensity obtained by this fit is defined by the amplitude of the singular Van Regemorter relation at its maximum, which occurs for an electron energy exactly at the threshold, which can be seen in Figure 6.7. For

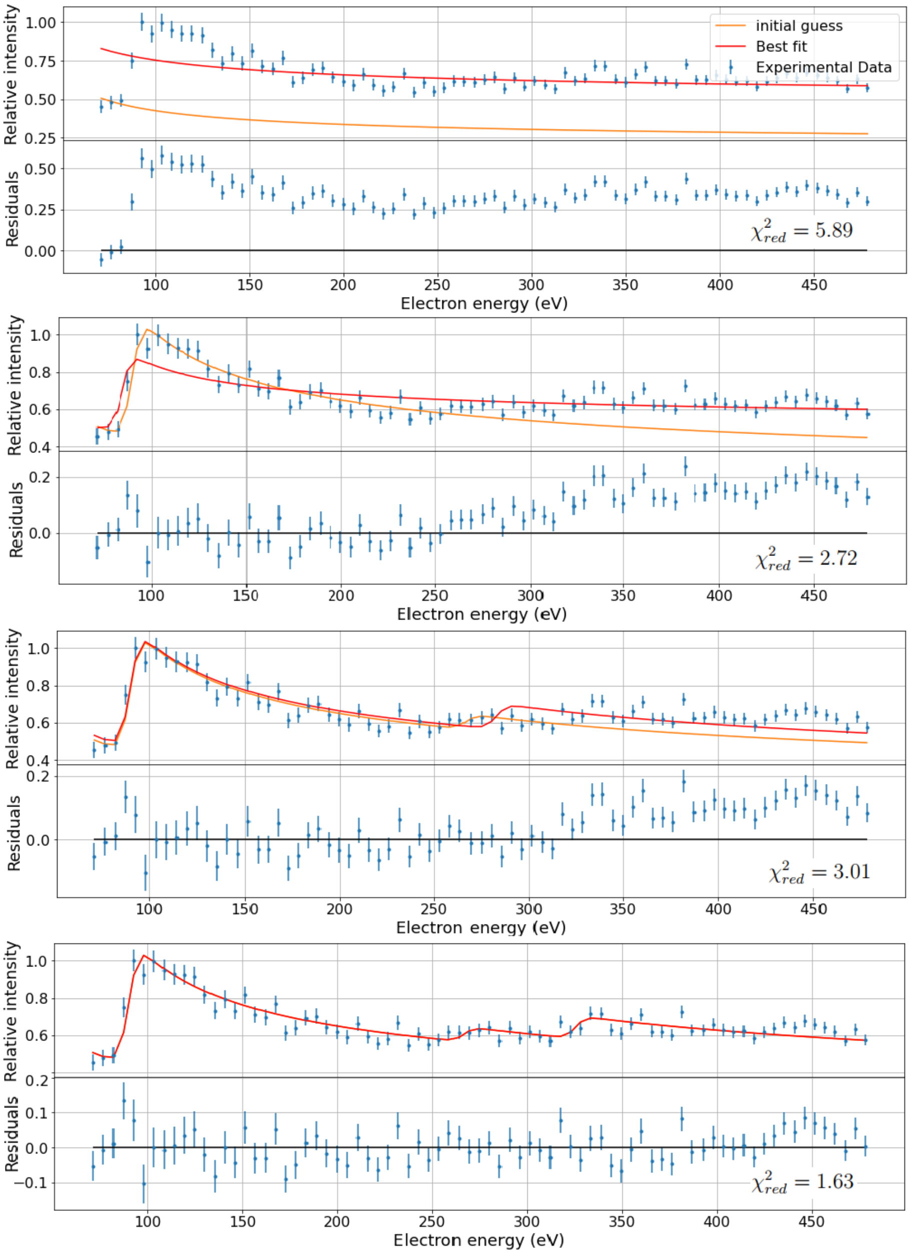

Figure 6.10: Example projection with increasing number of fitted Van-Regemorter relations. When the performed fit is insufficient, another threshold is added at higher electron energies. For each fit the difference between the experimental values and the fit function with the initial parameters are given as residuals below the data. A good indicator for additional thresholds is a systematic increase of these residuals with the electron beam energy. As an inset the value of χ^2_{red} is given for every fit, which improves upon adding the additional thresholds significantly.

Table 6.5: Fit results for the example projection displayed in Figure 6.10. To find relative oscillator strengths, the fit results for the maximum of the singular Van Regemorter curve are weighted by $E^2_{\text{threshold}}$ of the corresponding excitation process.

$E_{\text{threshold}}$	Relative intensity	Relative oscillator strengths $(I(E_{\text{threshold}})E^2_{\text{threshold}})$
50 eV	0.35	0.05
92 eV	0.50	0.22
267 eV	0.06	0.23
326 eV	0.09	0.50

a better comparison with theoretical results presented later on, these intensities can be related to the oscillator strength f_{if} of the involved transition via the Van Regemorter relation from equation 2.43:

$$I(E_{\text{kin}}) \propto Q_{if}(E_{\text{kin}}) = \frac{8\pi}{\sqrt{3}} \frac{1}{k_i(E_{\text{kin}})^2} \frac{f_{if}}{E_{\text{threshold}}} \overline{g}(E_{\text{kin}}) \pi a_0^2 \tag{6.9}$$

$$\Rightarrow I(E_{\text{threshold}}) \propto \frac{f_{if}}{E^2_{\text{threshold}}} \tag{6.10}$$

$$\Rightarrow f_{if} \propto I(E_{\text{threshold}}) \cdot E^2_{\text{threshold}} \tag{6.11}$$

where the effective gaunt factor $\overline{g}$ defined in equation 2.44 becomes

$$\overline{g}(E_{\text{kin}} = E_{\text{threshold}}) = 0.05538 \tag{6.12}$$

when the energy of the colliding electron is exactly the threshold energy for the excitation. In the case presented here, where many tightly spaced energy levels are expected at each threshold, due to the level structure of the investigated tin ions, the intensity, or amplitude of the fitted Van Regemorter relation, will then be proportional to the sum of the oscillator strengths of all transitions at the same energy between the initial states of the collisional excitations and the final states, from which then the spontaneous emissions are observed.

There are several approximations necessary for this proportionality of the intensity extracted in the fit and the oscillator strength of the collision process to hold.

For the individual electron collision excitation channel, also the population of the lower state, from which the excitation is initiated, will determine the strength of the observed signal.

These relative populations of each lower state can not be experimentally determined here, and as each threshold is likely to stem from many different transitions, which can't be resolved individually, originating from multiple different lower states, it is assumed that the same set of strongly populated lower states are involved for each denoted threshold, mostly dominated by the ground state or other low-lying states, averaging out this population effect. Therefore, in absence of a better assumption, the dependence on the lower state population is neglected in the displayed results.

Additionally it is possible due to cascade effects, that a singular excitation process could lead to two or more recorded photons, also lifting the proportionality

given in equation 6.10.
Furthermore, the intensity of radiation emitted by a specific excited state in the projected wavelength region λ will also be dependant on the unknown branching ratio Br:

$$\mathrm{Br} = \frac{\mathrm{Tr}_\lambda}{\mathrm{Tr}_{\mathrm{tot}} + \mathrm{Ai}_{\mathrm{tot}}} \tag{6.13}$$

with Tr_λ being the total radiative transition rate from the upper level, for transitions with emissions in the observed wavelength region λ, $\mathrm{Tr}_{\mathrm{tot}}$ the total radiative decay rate and $\mathrm{Ai}_{\mathrm{tot}}$ the total autoionization rate for the upper level. If the assumption is made, that autoionization does not play an important role here, when compared to radiative decays, and that each excited state only decays via few selected strong channels, then these branching ratios can also be assumed to be roughly one. Generally, autoionization will only occur for excited states above the ionization potential [105]. This means, that here the collisional excitation rates for excited states of very high energy may be underestimated.

The dependence of the extracted intensities on quantities in addition to the summed oscillator strengths of the transitions, means the relative oscillator strengths for the different thresholds given here can only be thought of as approximate values. Still, the weighting with $E^2_{\mathrm{threshold}}$ has the merit of allowing for a better comparison to theoretical result presented later on in chapter 7. Additionally, just accounting for the intensity at threshold as obtained by the fit without rescaling it, would underestimate the contributions of states of high energies. As every excitation cross section gets reduced with the electron kinetic energy, the higher thresholds naturally yield smaller fit intensities. The rescaled intensities on the other hand give an estimation of the relative excitation rates for two possible excitation processes at the same electron energy.
Hence, using the proportionality given in equation 6.10, the intensity results from all following fits have been re-scaled to such relative compound oscillator strengths.

The values in Table 6.5 as well as the results obtained by the other fits performed with the same method are given without errors, as the multitude of input parameters, relatively large errors of the individual data points and the folding of the whole function with a gaussian, make the errors for the fit parameters as given by the fit algorithm extraordinarily large.
In this manner, fits are performed for electron energy projections from regions of interest each containing a small part of the observed wavelength spectrum. An additional selection of projections with the corresponding fit employing the multiple Van Regemorter relations is depicted in Figure 6.11. Those projections come from the measurement with the breeding energy of 259 eV focusing on Sn^{13+}. These fits show, that for different wavelength regions the contributions of additional thresholds to the relative intensities are noticeably different, eliminating the possibility, that the observed intensity variations come from a systematic variation of the intensity over the whole spectrum as a result of e.g. ion population variations during the measurement cycles.

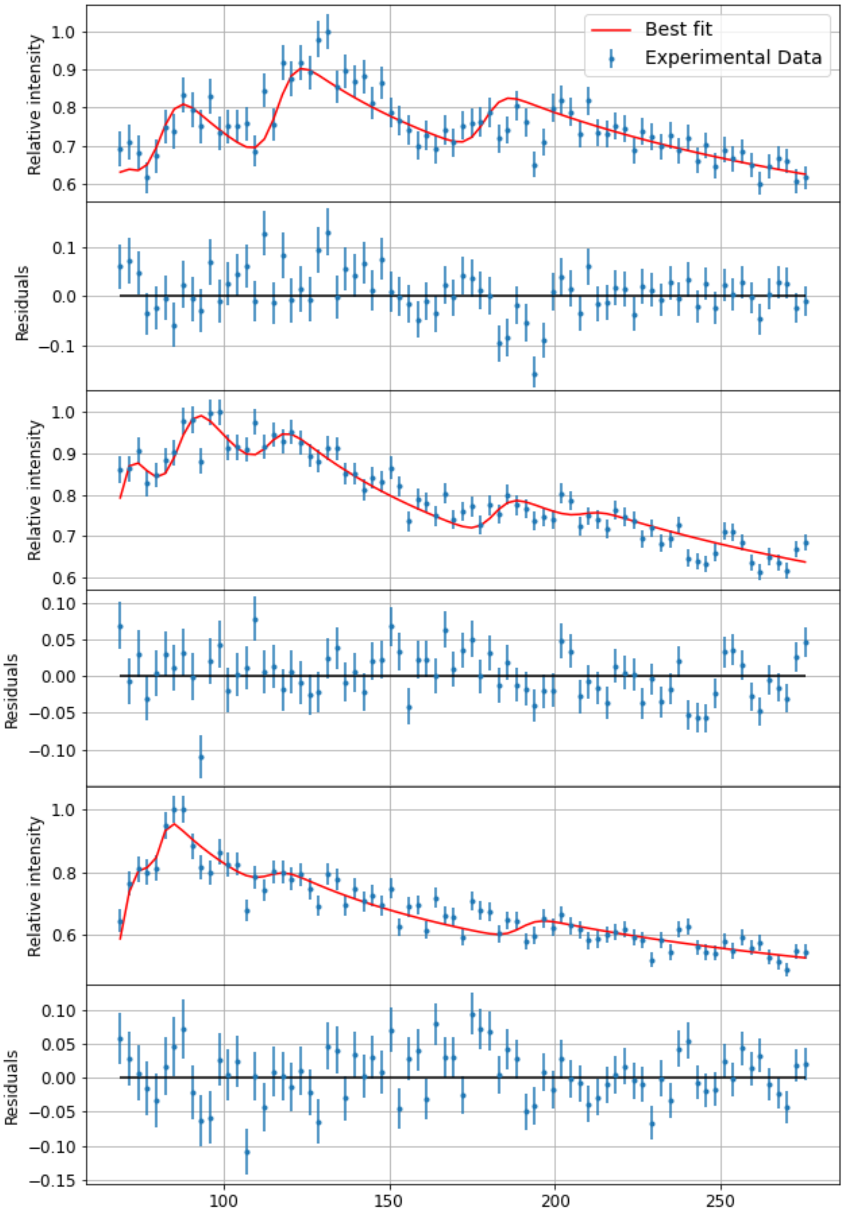

Figure 6.11: Three line projections from the Sn^{13+}-measurement, with the corresponding excitation cross section fit and residuals below. **Top:** 12.1 nm - 12.3 nm; **Middle:** 12.6 nm - 13.05 nm; **Bottom:** 14.95 nm - 15.1 nm

Overall, the whole spectrum for each of the fast ramping measurements is covered. The complete fit results for the measurement focusing on Sn^{14+} are given in Table 6.6. The results for the other measurements are moved to the appendix.

Table 6.6: Fit results for the electron energy projections produced from the data of the Sn^{14+}-measurement. The denoted relative oscillator strengths f_{rel} add up to 100 for each fit. Again, they are obtained by weighting the intensity of the individual Van Regemorter curves at threshold by the square of the threshold energy ΔE^2. In the second to last column the total photon counts in the denoted wavelength range are given. These are used to compare the contributions of the different thresholds between wavelength ranges and measurements.

λ (nm)	Thresholds (eV)	f_{rel}	Counts	χ^2_{red}
12.15 - 12.6	51/116/277/352	9/19/20/60	14366	1.42
12.6 - 13.0	33/315	26/74	17128	1.27
13.0 - 13.2	78/140/330	90/1/9	14895	1.78
13.2 - 13.4	84/160/259/335	22/4/16/58	56198	4.86
13.4 - 13.8	60/84/110/160/250/310/350	8/12/3/8/20/36/13	53135	3.02
13.8 - 14.6	72	100	51233	1.88
14.6 - 15.6	68	100	67235	1.38
15.6 - 16.0	71	100	35380	0.98
16.0 - 16.3	71/130/268	48/7/45	15365	3.57
16.3 - 17.0	68/115/251/329/450	18/6/13/22/41	42841	1.62
17.0 - 17.4	70/124/255	42/12/46	21330	1.60
17.4 - 17.6	76/121/150/341	31/7/9/54	9997	1.15
17.6 - 18.0	71/113/260/345	28/8/23/41	17252	1.17
18.0 - 18.4	63	100	13982	1.16

The relative oscillator strengths f_{rel} given here are again obtained by weighting the amplitude of the individual Van Regemorter curves in the fit by the square of their threshold energy, as explained above and can only be treated as approximate values due to the outlined reasons. When comparing these contributions between different wavelength regions or measurements, they are multiplied with the total photon counts in the denoted wavelength range.

The fits for some regions have a significantly worse χ^2_{red} than the other fits, for example the one for the wavelength region of 13.2 nm - 13.4 nm denoted in Table 6.6. The relative intensities in those regions seemed to include many more variations with small amplitudes than in other regions. Fitting those individually proves difficult, hence only the clearly identifiable contributions as outlined are considered, found as outlined above.

When analyzing the results of these fits for the different measurements, one has to keep in mind, that in the measurement focused on Sn^{13+} the electron energy was only ramped up to 300 eV. Therefore, the amount of radiation coming from triply excited states or states of even higher energy is underestimated there, when compared to the other measurements.

All the determined thresholds are compiled into a histogram, each threshold weighted with the respective determined oscillator strength and total counts in the wavelength range of the corresponding fit. This histogram is shown in

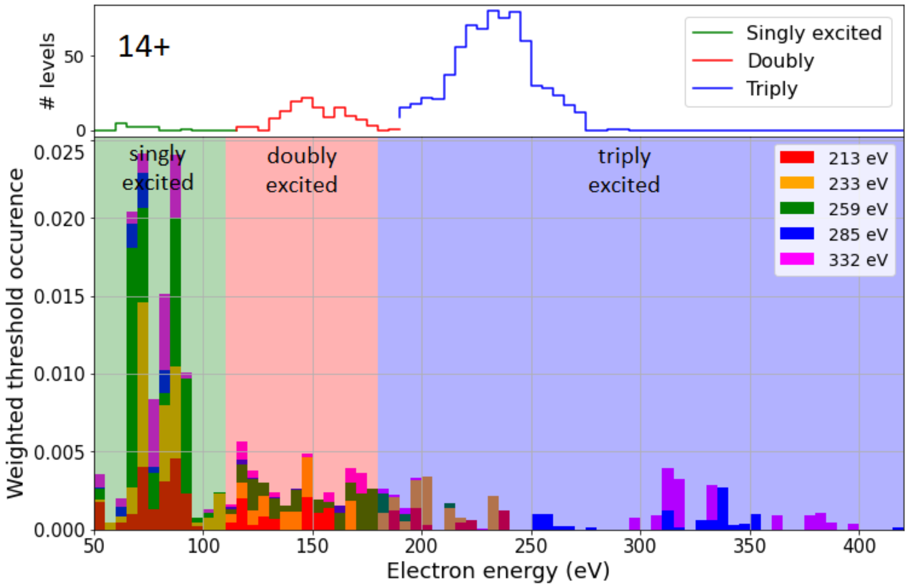

Figure 6.12: Compiled fit results from the fast measurements. Each bin of the histogram consists of the sum of all thresholds found in a 5 eV wide energy window, each weighted by its respective relative oscillator strength as found with the multiple Van Regemorter fit. The energy is divided into three regions according to the calculated density of states for the tin ions as presented in the Figures 2.4 and 7.1 into regions occupied by singly, doubly and triply excited states as defined in section 2.5. The calculated density of states for Sn^{14+} is given on top for reference.

Figure 6.12.
The distribution of those production thresholds should coincide with the density of states as shown in Figure 2.4 or the top panel of Figure 6.12. This correspondence of the distribution of found thresholds and the density of states, is only valid, if the assumption is made, that the collisional excitation processes only originate from the electronic ground state or other low lying states, as the observed thresholds are determined by the energy difference between the lower and upper level of the collisionally induced transition. This does not necessarily need to be the case. As was already shown in section 5, certain charge states had a significant part of their populations in metastable states with high energies. If then, for example, the collisional excitation takes place between a metastable singly excited state and a doubly excited state, the resulting threshold will appear to be in the same range as the threshold of an excitation process from the ground state to a singly excited state. The misinterpretation of excitation pathways would then correspond to the relative populations in the metastable states, which was determined in section 5 to be highest for Sn^{14+} at approximately 50 %. For the other charge states populations in high lying metastable states were consistently much lower. For them the attribution of the thresholds to the different degrees of excitation should hold.

Figure 6.12 reveals, that the found thresholds can be indeed grouped similarly to the level structure presented in the beginning in Figure 2.4. A first block, where many of the found thresholds are located, can be made out between an

Table 6.7: Overall contributions in terms of relative oscillator strengths found from the different excited states blocks in the different fast measurements. The values are found by summing up the found oscillator strengths from the fitted Van Regemorter relations and weighting them with the overall counts in the respective wavelength region. Note that for the third measurement the highest energy during the scanning phase is 300 eV and therefore the found contributions of highly excited states are lower than for the other measurements.

Breeding energy	Singly excited	Doubly excited	Triply excited and above
213 eV	59.5 %	27.9 %	12.6 %
233 eV	57.2 %	25.6 %	17.2 %
259 eV	73.2 %	24.1 %	2.8 %
285 eV	54.2 %	4.3 %	41.4 %
332 eV	57.8 %	12.3 %	29.9 %

energy of 50 eV and 100 eV. Beyond that first block, fewer thresholds with overall smaller relative oscillator strengths are found.

As a first result, this threshold distribution shows that the transitions towards states termed as singly excited states earlier are dominant in this experiment. Excitations towards multiply excited states with subsequent photon emission seem a lot less prevalent, although significant contributions of them are still found. Without them, the intensity of the recorded radiation as a function of the electron energy could not be explained.

Overall, the integrated relative oscillator strengths found for the three different state ensembles are given in Table 6.7, obtained by adding all weighted thresholds in each of the three energy regions (up to 110 eV for singly excited states, 110 eV to 180 eV for doubly excited states and higher than 180 eV for triply excited states and higher lying states). This analysis further reveals trends between the measurements with different breeding energies and thus different charge state distributions. For the measurements with lower breeding energies, lower overall contributions of triply excited states and states of even higher energies are found, compared to the measurements with higher breeding energies. This might be a result of either different level structures and transitions strengths for the different ionic species or a result of different level populations produced in the breeding phases, which then have an effect on the collisions induced in the scanning phase.

To further show how this radiation, attributed to the different energy blocks, is distributed across the recorded wavelength range, another analysis step has been taken. After the initial projection of all events in the three predefined energy windows in Figure 6.6 gave no conclusive insight on this distribution, the results from the electron collisional excitation cross section fits are now recompiled to find an answer.

To produce spectra from the results of the collisional excitation cross section fits, each individually fitted wavelength region defined before and given in the respective result table (Table 10.6, 10.7, 10.8, 6.6 and 10.9) is represented by one bin in the new spectra. For each of those wavelength bins, the found oscillator strengths of the different Van Regemorter curves are attributed to one of the three level ensembles, singly, doubly or triply excited states according to the threshold energy of the curve. Taking the densities of states in Figure 2.4 as a

basis, the amplitudes of all contributions fitted to thresholds below 110 eV are attributed to singly excited states, thresholds between 110 eV and 180 eV are attributed to doubly excited states and every threshold at even higher energies is attributed to triply excited states. Then the relative oscillator strengths of the grouped thresholds are summed up and presented as the height of one bin in the generated spectrum. Lastly the relative oscillator strengths are multiplied by the total amount of photons detected in the wavelength region, to give a comparison between wavelength regions and recover a spectrum again.
The resulting spectra for the different fast measurements are shown in Figure 6.13.

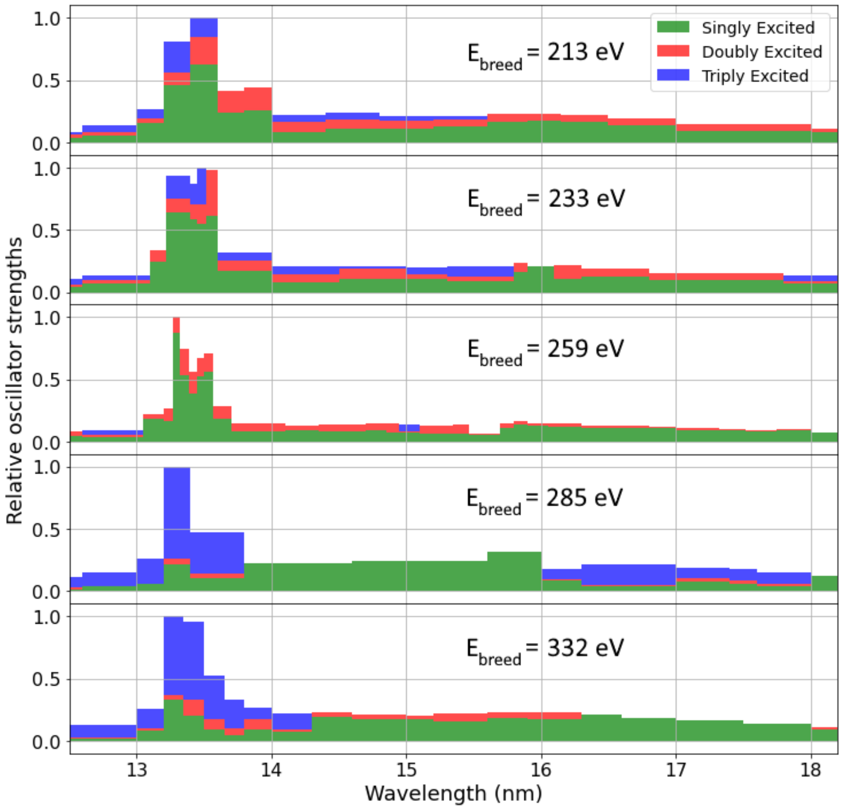

Figure 6.13: Spectra generated from the results of the electron collisional excitation cross section fits for all conducted fast measurements. Each bin contains the summed relative oscillator strengths as attributed to the three different excited state ensembles, multiplied by the total signal detected in the wavelength region. The contributions of the different state ensembles are stacked on top of each other. Note that for the third measurement the highest electron energy during the scanning phase was 300 eV and therefore little contributions from triply excited states and higher lying states could be made out. Therefore visible contributions of triply excited states are systematically lower in that measurement.

From these generated spectra the conclusion can be drawn, that the transitions from multiply excited states seem to mainly play a role in the region of the main line around 13.5 nm and at lower wavelengths. Meanwhile at higher wavelengths, fewer contributions are found. As you see here, the compound oscillator strength of all transitions towards singly excited states is highest in every conducted measurement. Notable is further the small amount of triply excited transitions found in the measurement using the breeding energy of 259 eV. This is due to the electron energy there being only scanned up to 300 eV, in contrast to the other measurements, where the scans reach up to 500 eV. Therefore in the other measurements the effects of populating triply excited states and states with even higher energies are more obvious, as the behavior of the intensity at higher electron energies is very indicative of those contributions, as seen in Figure 6.10.
With this analysis done, calculations based on FAC are going to be presented, in order to find an explanation for the distribution of the found radiation thresholds.

Chapter 7

Comparison to Calculations

As a comparison to the experimental data, calculations using FAC, whose functionality has been described in section 2.4, are performed.

7.1 Calculation of Spectra at Static Electron Beam Energy

As outlined there, a starting point for the theoretical modeling are the atomic structure calculations, which yield the energy levels of the different electronic states. In this first step the electronic configurations, which are to be included in the configuration interaction performed here, are being defined. Inclusion of all configurations is not possible due to exponential scaling of computation times, as mentioned in section 2.4, which is why a careful selection needs to be done. The configurations included for Sn^{13+} and Sn^{14+} are listed in Table 7.1. The used configurations for the remaining charge states are listed in Table 10.10 in the appendix.

As mentioned throughout this thesis, the electronic states in highly charged tin can be grouped into several level ensembles, termed here singly, doubly and triply excited states. Both, calculations taking all listed states into account, as well as calculations only including transitions between specific ensembles have been conducted, in order to see at which wavelengths spectral lines originating from decays of these energy blocks might manifest. The correspondence of the configurations to the different ensembles of states is noted in Table 7.1.

The results of the atomic structure calculations using these configurations can be seen in the left panels of Figure 7.1. The energy states corresponding to the different ensembles are presented in different colors. Using this atomic structure calculation, the possible transitions between the electronic states are calculated, resulting in many lines in the observed EUV-region, where for each transitions the wavelength and the transition rate are obtained.

Table 7.1: States included in the configuration interaction for Sn^{13+} (**left**) and Sn^{14+} (**right**). The configurations used for the calculations of the other charge states are listed in the appendix. In any calculations, the shells up to M-shell are always treated as closed.

State ensemble	Configuration	State ensemble	Configuration
Ground state	4s2 4p6 4d1	Ground state	4s2 4p6
Singly excited	4s2 4p5 4d2	Singly excited	4s2 4p5 4d1
	4s2 4p6 4f1	Doubly excited	4s2 4p5 4f1
Doubly excited	4s2 4p5 4d1 4f1		4s2 4p4 4d2
	4s2 4p4 4d3		4s1 4p6 4d1
	4s1 4p6 4d2	Triply excited	4s2 4p4 4d1 4f1
Triply excited	4s2 4p4 4d2 4f1		4s2 4p3 4d3
	4s2 4p3 4d4		4s1 4p6 4f1
	4s1 4p6 4d1 4f1		4s1 4p5 4d2
	4s1 4p5 4d3		

The transitions resulting from the calculation are each weighted with the corresponding transition strength and inserted into histograms in the right panels of Figure 7.1. The contributions of the different excitation blocks are stacked on top of each other.

The calculated list of transitions is not yet comparable to experimentally observed spectra. To obtain such spectra, each individual transition still needs to be weighted with the population of the involved upper state.

The calculation of this population distribution is done with the collisional radiative model (CRM) introduced in section 2.4. To execute any calculation in the model, the electron kinetic energy distribution, as well as the electron density in the radiating plasma are necessary. The reason for that is, that those two parameters significantly change the collisional excitation rates in the plasma, as well as the available excitation energies. These two quantities are central to the population distribution, which is to be found via the CRM, to obtain the spectra.

The electron kinetic energy distribution is assumed to be gaussian. To give an estimate of the width of this gaussian distribution, the width of the dielecronic resonance, which was used for the determination of the space charge in section 4.5 can be used. There a gaussian fit to the resonance yielded a width of about

$$\sigma = 5\,\mathrm{eV}$$

The electron density in units of $\frac{1}{cm^3}$ is chosen to be

$$n_e = 5 \cdot 10^{-10}\,\frac{1}{\mathrm{cm}^3}$$

Such a value is a typical electron density for an EBIT [64] and a sufficient approximation here. The determination of the exact electron density is difficult and a determination of the space charge in the previous section 4.5 is not enough to accomplish that, as the space charge compensation by the positive ions remains unknown here.

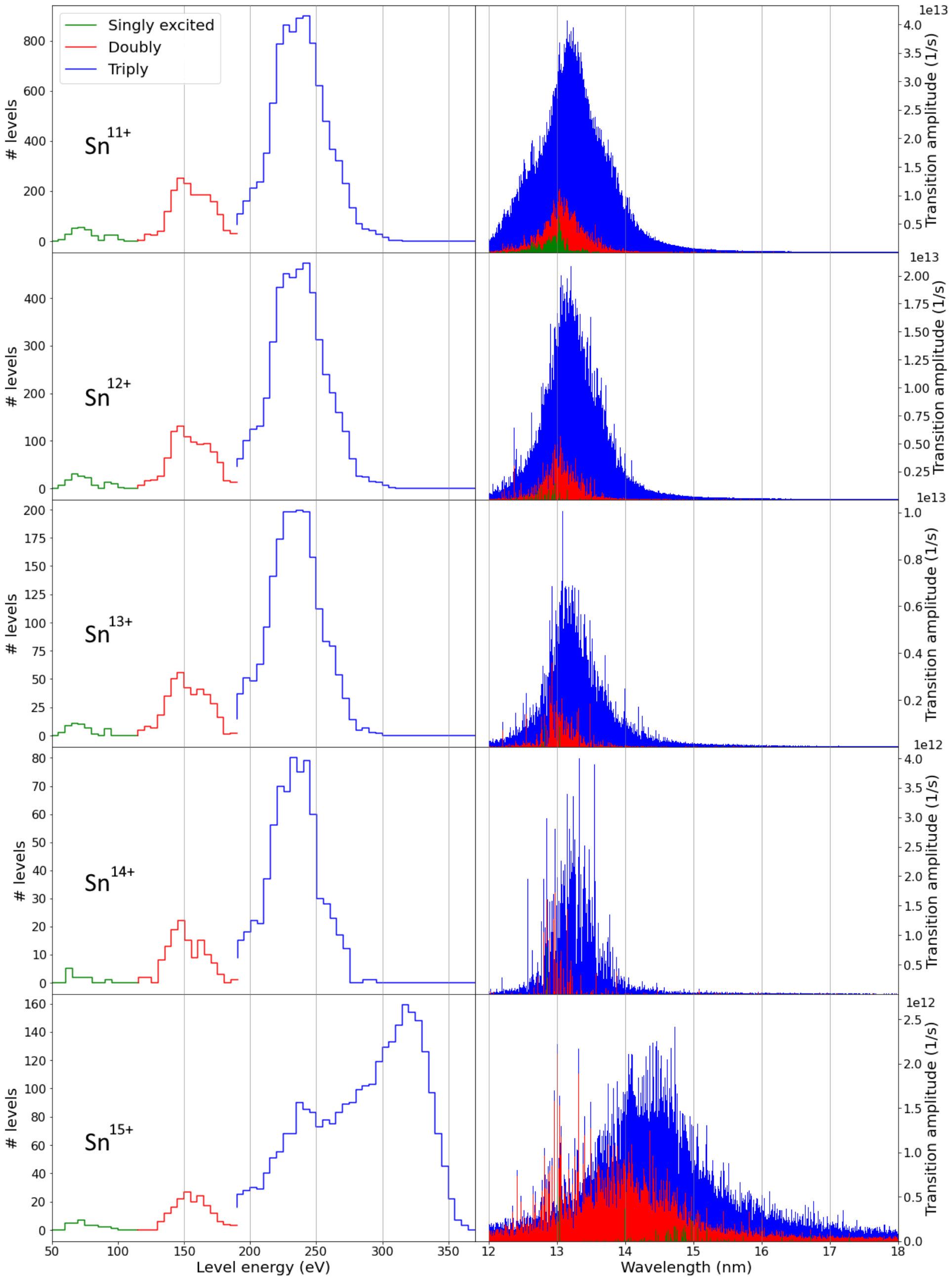

Figure 7.1: Results of the FAC calculations for the different observed charge states using the configurations listed in Table 7.1 and 10.10. The left panels each show the calculated density of states, which is grouped into three ensembles, singly, doubly and triply excited states, according to the level energies. The right panels each show a histogram of the transitions originating from the three defined ensembles, with each individual transition being weighted by its transition strength. Every weighted transition within a width of 0.006 nm is added to form one bin of the histogram. The contributions of the different ensembles are stacked on top of each other.

As the main driver of population of upper states in the plasma is electron collision excitation, the electron collision cross sections between the different electronic states are calculated as well, as an input for the CRM. These cross sections are calculated for 32 different, evenly spaced electron energy values between 50 eV and 500 eV for each transition, to get sensible values for the level populations at different electron energies later on.

Using the calculated atomic structure, transition rates and collisional excitation cross sections and the values for the electron energy distribution and the electron density, the CRM is performed for the different tin charge states, to obtain the state populations and thus weightings of the transitions from the various upper states to calculate a spectrum. In a last step the individual spectral lines are folded with a gaussian with a width of $\sigma = 0.01\,\mathrm{nm}$ to get a spectrum comparable to the one measured in the experiment.

Apart from the charge states ranging from Sn^{11+} to Sn^{15+} investigated in detail during the fast measurements, also the photon spectrum of the other charge states between Sn^{7+} and Sn^{20+} are calculated as a comparison to the NMF performed in section 5.

The electron energy set for all of these theoretical spectra, calculated using the collisional radiative model, are the electron energies of maximum abundances as determined in section 5 and tabulated in Table 5.2, for a best comparison to the experimental results.

Note, when displaying the total photon spectrum as calculated with this approach, one has to account for a total shift of the spectrum against the experimental result. More sophisticated methods than the calculation using the configuration interaction with the limited amount of included states performed here, such as relativistic many-body-perturbation-theory [54], could get rid of such a needed empirical shift. However, such methods are very costly in the needed computing power and complicated to implement and thus not feasible in the context of this thesis. A comparison to the experimental spectrum allows for the shift, which is fixed at a different value for each charge state to reach the best agreement. The shifts in the order of the charge states from Sn^{7+} to Sn^{20+} are as follows: 0.28 nm, 1.25 nm, 1.2 nm, 1.2 nm, 1.13 nm, 1.1 nm, 1.09 nm, 0.2 nm, 0.63 nm, 0.28 nm, −0.3 nm, −0.22 nm, −0.12 nm, −1.1 nm.

As can be seen in Figure 7.2, agreement varies over the range of the different charge states. One reason for that is the suspected pollution of the trap with oxygen, leading to strong additional lines at low and high electron energies, which partly outshine the lines originating from the highly charged tin. Therefore the disagreement gets especially large for the lowest and highest charge states for which the spectra were calculated. For the intermediate charge states the agreement is better. Especially line positions fit well for many of the charge states, with some exceptions for which some individual calculated line positions seem to be again shifted against the experimental positions. One example for that is the distinct line at around 16.2 nm for Sn^{14+}. The main feature around 13.5 nm of each of those charge states is recovered nicely. This main feature is comprised of 4p-4d-transitions. One can also observe the shift of this main feature towards shorter wavelengths with higher charge states up until Sn^{14+}. For higher charge states the 4p-shell is not filled anymore, hence also 4s-4p transitions become important, significantly altering the shape of the spectrum, as

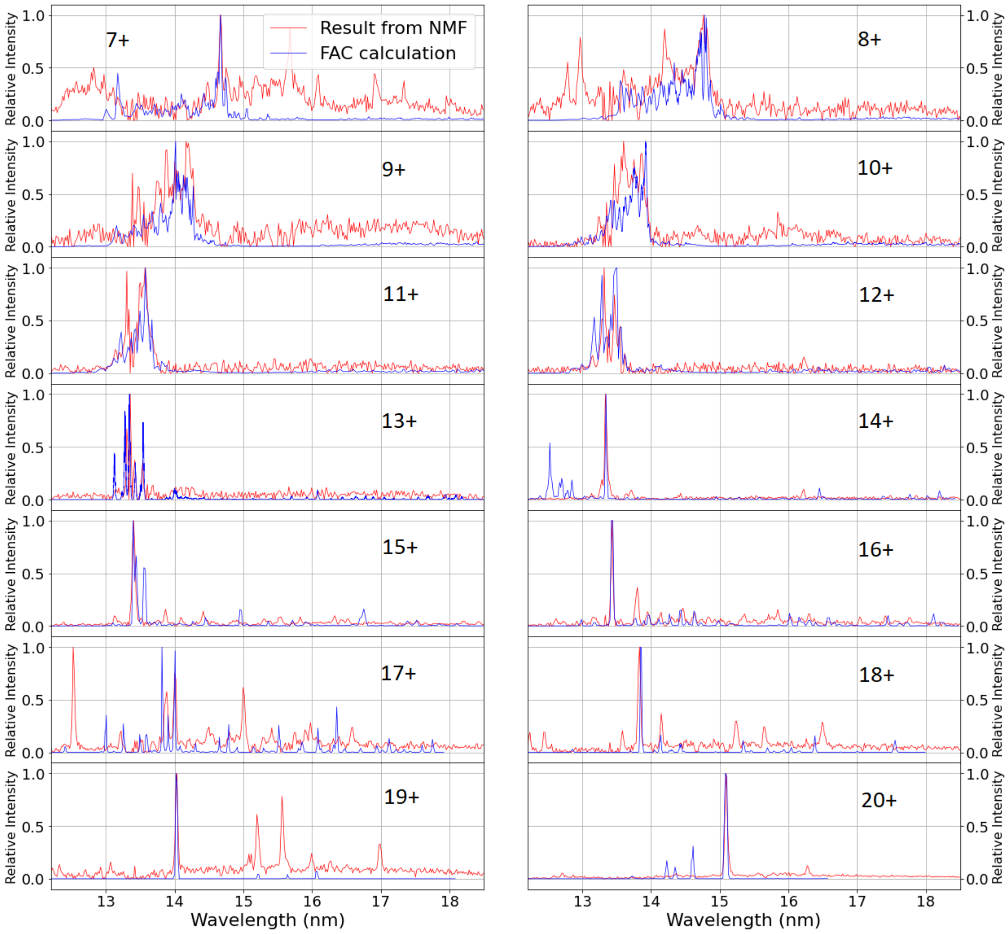

Figure 7.2: Pure spectra from the NMF performed in section 5. Each extracted spectrum is overlaid with the result of the performed FAC-calculation. The total spectra for each charge state are shifted to fit the experimental spectrum. The shifts in the order of the charge states are as follows: 0.28 nm, 1.25 nm, 1.2 nm, 1.2 nm, 1.13 nm, 1.1 nm, 1.09 nm, 0.2 nm, 0.63 nm, 0.28 nm, −0.3 nm, −0.22 nm, −0.12 nm, −1.1 nm

compared to the charge states with a filled 4p-shell.

Line intensities on the other hand are often not reproduced well by the calculations. This is due to them being heavily reliant on the energy level populations determined via the CRM. This determination in turn is very sensitive to the calculated transition rates and the used input parameters. Thus any errors in those compound in the final intensity results.
Additionally, especially in the case of charge states below Sn^{14+}, the electronic structure gets much more complex due to electrons being present in the 4p-subshell. This leads to hugely increasing computation times and number of lines calculated. Therefore there the selection of levels to be included in the configuration interaction becomes even more critical, and fewer overall configurations could be reasonably included.

7.2 Modeling of the Electron Energy Dependent Spectra

7.2.1 Varying State Populations

Apart from the pure photon spectrum for a given set of parameters (electron energy, energy width and density), another important calculation is done in order to answer the question which levels contribute dominantly to the EUV-spectrum in highly charged tin. Calculations are to be performed, which explain the behavior of the recorded intensities in dependence of the electron beam energy in the fast measurements. Therefore, for the charge states from Sn^{11+} to Sn^{15+}, CRM calculations are repeated for a wealth of different input electron energies. By setting different electron energies for the CRM, different state populations are obtained in each calculation. This is due to the collisional excitation rates being dependant on the electron energy (see section 2.3), which in turn makes the excited state populations, and therefore the calculated spectrum, electron energy dependant. For the example of Sn^{14+}, the individual spectra with different electron kinetic energies as inputs, calculated using the CRM, can be seen in the lower panel of Figure 7.3. Similar to the experimental method of recording the line strengths at varying electron beam energies, one now can obtain a theoretical prediction of the relative line strengths at different electron energies.

By stacking the individually calculated spectra on top of each other, again a two-dimensional spectrum for each charge state as seen in the fast measurements is recovered. This spectrum is shown in Figure 7.3 for the case of Sn^{14+}. One can indeed see a similar structure to the experimentally determined two-dimensional spectra. Different spectral lines appear at different electron energies, once the production threshold for the upper state is reached. Those lines then persist through higher electron energies, with just the intensity varying slightly.
Investigating the intensity of each line or wavelength region now, as a function of the electron beam energy yields projections analogous to the prior experimental results. This way it can be checked, whether the changes in line intensities which were attributed to additional thresholds for the production of multiply excited states via collisional excitation are also expected theoretically.

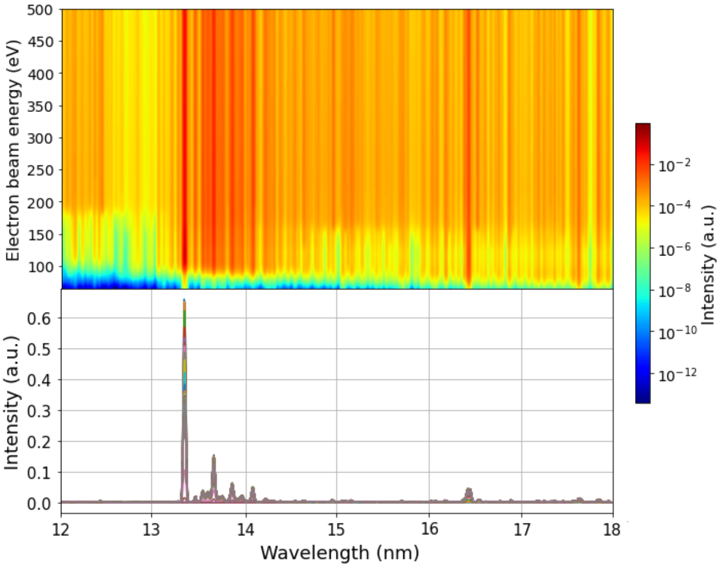

Figure 7.3: **Top:** Theoretical two-dimensional spectrum resulting from spectra of Sn^{14+} calculated via the CRM of FAC for many different electron energies. The result has the same form as the two dimensional map shown in Figure 6.1. **Bottom:** Individual CRM-spectra of Sn^{14+} at different electron energies in different colors. Each of those spectra represents one line in the two-dimensional spectrum above.

One such pair of experimental data and corresponding calculation can be seen in Figure 7.4, displaying the wavelength region of 13.2 nm to 13.4 nm, comparing the measurement focused on Sn^{14+} to the CRM-calculation of the Sn^{14+}-spectrum in that same wavelength range. The position of the initial onset is shifted in the displayed calculation when compared to the experimental result. Even when shifting the complete theoretical projection by 18 eV to fit to the initial onset of the experimental line intensity, differences between this model calculation and the experimental results are apparent. With the first peak and the subsequent plateau described sufficiently in the calculation, at higher energies, the differences between the theoretical prediction and the experimental data become more and more pronounced. For example at around 150 eV the experimental line intensity stagnates at a much higher value than in the calculation, which hints at an additional threshold being met there, which aren't included in the CRM. At even higher energies, the theoretical values even out at a value significantly below the experimental ones. Again, additional transitions might come into play in the experiment, which contribute to the intensity at high energies, which aren't included in the calculation.

Another example for a comparison of the CRM-prediction to the experimental result is given in Figure 7.5, showing the observed and calculated intensities for Sn^{14+} between 14 nm and 15 nm. There the agreement between the CRM-calculation and the experimental results are even worse. The line intensities in the CRM-calculations are highest at 200 eV with several stepwise increases at lower energies. Meanwhile in the projection from the experiment, the line inten-

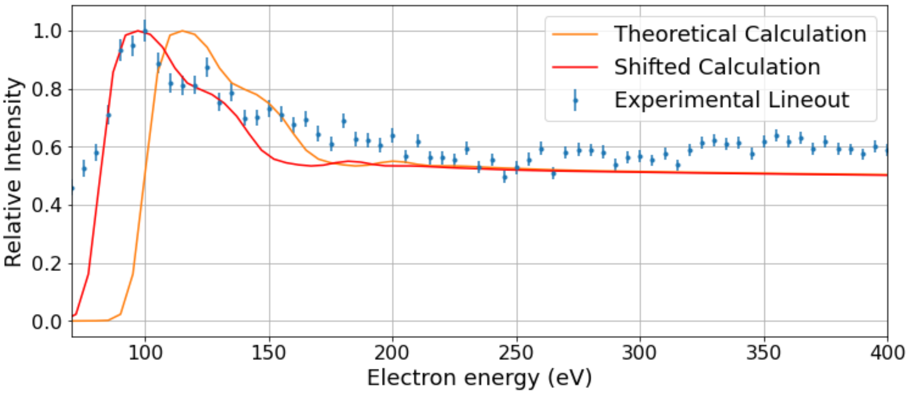

Figure 7.4: Projection of the line strength of the main line of Sn^{14+} for different values of the electron energy, as calculated with the CRM. As a comparison, the electron energy projection of the intensity in the main-line region for the fast measurement focusing on Sn^{14+} is given. Additionally, the calculation is displayed again, shifted by 18 eV to reproduce the experimental results.

sities are strongest at the low energies with an essentially monotonous decrease towards higher energies. This discrepancy between the theoretically predicted and experimentally found line intensities, with the behavior at low energies not being reproduced, holds true for many projections and isn't exclusive to the case of Sn^{14+}.

One reason for the discrepancies can be, that the states included in the FAC-calculations are insufficient. Then especially at high electron energies, where more and more highly excited states can start radiating, the experimental line intensities should be amplified compared to the theoretical prediction.

Another problem with the comparison is the remaining uncertainty in the charge state distribution inside the EBIT during the measurement. Even though, steps were undertaken to have a charge state balance dominated by the ion in question, one can not exclude the contributions of other ionic species completely, as was shown in section 6.1. Therefore the experimental two-dimensional spectra should indeed be a mixture of the calculated two-dimensional spectra, which each contain only one charge state.

One might also include the behavior of contaminants inside of the trap in the calculations. Especially traces of oxygen were still observed in the EUV spectra shown before. Strong contributions of the trapped oxygen ions could explain the experimentally amplified intensities at low electron energies, when comparing the experimental projections to the theoretical predictions. However, these oxygen lines, if they were only, or primarily, contributing to the spectrum at lower electron energies, would lead to large differences in the observed shape of the spectrum at different electron energies. However, the shape of the spectrum changed barely at different electron energies as shown in Figure 6.6, ruling out large contributions of oxygen as an explanation for the difference between experimental projections and the theoretical model at low electron energies.

Therefore these refinements of the calculations should hardly be enough to explain the fundamental mismatch between many of the experimental and theo-

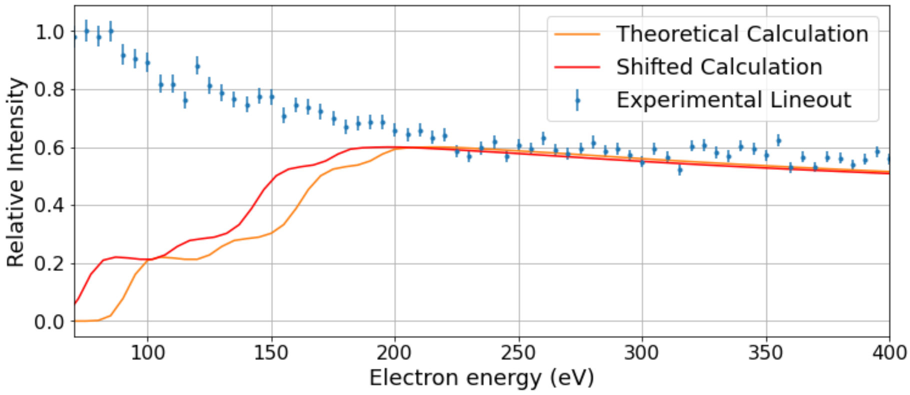

Figure 7.5: Projection of the intensity in the region between 14 nm and 15 nm of the spectrum of Sn^{14+} for different values of the electron energy, as calculated with the CRM. As a comparison, the electron energy projection of the intensity in the same wavelength region for the fast measurement focusing on Sn^{14+} is given. Additionally, the calculation is displayed again, shifted by 18 eV, which reproduced the experimental results in the prior comparison displayed in Figure 7.4.

retical projections, especially at low electron energies. Rather, the calculation method needs to be reevaluated and overhauled completely. As outlined in section 2.4, the employed collisional radiative model assumes a steady state energy level population distribution, where for each electronic state, populating transitions balance out the depopulating mechanisms. In the experiment however, such a steady state distribution may not be present. As during the measurement cycles, the electron energy gets ramped quickly, there may not be enough time to arrive at a steady-state distribution. Instead, long-lived, metastable states will still roughly retain their population accrued during the breeding phase, while short-lived energy states will change their populations quickly, due to collisional excitation and radiative decay, as the electron energy is varied. This more complex population distribution means, that the conducted CRM-calculations are only valid to obtain values for the static spectra, found during the breeding phases of the fast scans or the spectra contained in the slow measurement, as depicted in Figure 7.2. A more refined method, to get a theoretical prediction of the time- and electron energy-dependant spectra observed during the scanning phase of the fast scans thus needs to be used.

7.2.2 Fixed State Populations

A second model was developed and applied to find theoretical intensity functions correlating to the fast scanning measurements. This time, the populations during the breeding phase, as determined via the CRM are taken as the energy level population distribution for all energies. Again, the electron collisional excitation rate σ^{exc} between all levels is calculated for 32 different electron energy values E_{e^-}. Then the assumption is made, that each excited electron decays in the same time-/energystep via spontaneous decay, to keep the energy level populations constant. Each of those decay channels is calculated with the corresponding transition rate and photon wavelength. One can then again filter for the wavelength and sum up all contributions in the chosen wavelength region λ, where the intensity at an electron energy E_{e^-} is then recovered from the following quantities:

$$I(E_{\mathrm{e}^-},\lambda) = \sum_u \left(\sum_l n_l(E_{\mathrm{breed}}) \sigma^{exc}_{l \leftarrow u}(E_{\mathrm{e}^-}) \right) \frac{\mathrm{Tr}_u(\lambda)}{\mathrm{Tr}_{u,tot}} \tag{7.1}$$

where the index l denotes lower levels, where the electron excitation processes originate from and u upper levels, from where the radiative transitions are initiated and are recorded in the wavelength region λ.

A visualization of the model can be seen in Figure 7.6. There an example system with one lower level n_{lower} populated in the breeding phase is given. From this level, two upper levels, $n_{\mathrm{upper,1}}$ and $n_{\mathrm{upper,2}}$ are produced by significant electron impact excitation. These upper states may decay via several radiative transitions, which could be observed by the detector, where each transition has a different transition rate Tr and emits photons in one of the two example wavelength regions λ_1 or λ_2.

When then calculating the intensity in the wavelength region λ_1 at the electron energy E, the collisional excitation rates for the different upper levels multiplied with the radiative branching ratios give the result for the relative intensity:

$$I(E,\lambda_1) = \sigma_1(E) \frac{\mathrm{Tr}_{1\to\mathrm{a}} + \mathrm{Tr}_{1\to\mathrm{b}}}{\mathrm{Tr}_{1\to\mathrm{a}} + \mathrm{Tr}_{1\to\mathrm{b}} + \mathrm{Tr}_{1\to\mathrm{l}}} + \sigma_2(E) \frac{\mathrm{Tr}_{2\to1}}{\mathrm{Tr}_{2\to1} + \mathrm{Tr}_{2\to\mathrm{a}}} \tag{7.2}$$

As the calculations quickly scaled in complexity, configuration averaging is used here [41]. Many different, tightly spaced energy levels are compiled into one "superlevel" with an average energy. This reduces the computation time needed, at the detriment of exact results. However, the new model already contains many approximations, meaning such additional approximations are justifiable. Configuration averaging allows including many more states, also of higher excitation, than before, due to the reduced complexity.

In the end the resulting intensity curves are again folded with a gaussian to attribute for the experimental uncertainty of the electron beam energy. When comparing to the experimental spectrum, a constant background is added to the theoretical intensity curve.

Again, also for this model, the results don't agree with the experiment, when choosing tight wavelength windows for the projections. However, when looking at the complete spectral range, which is recorded in the experimental setup,

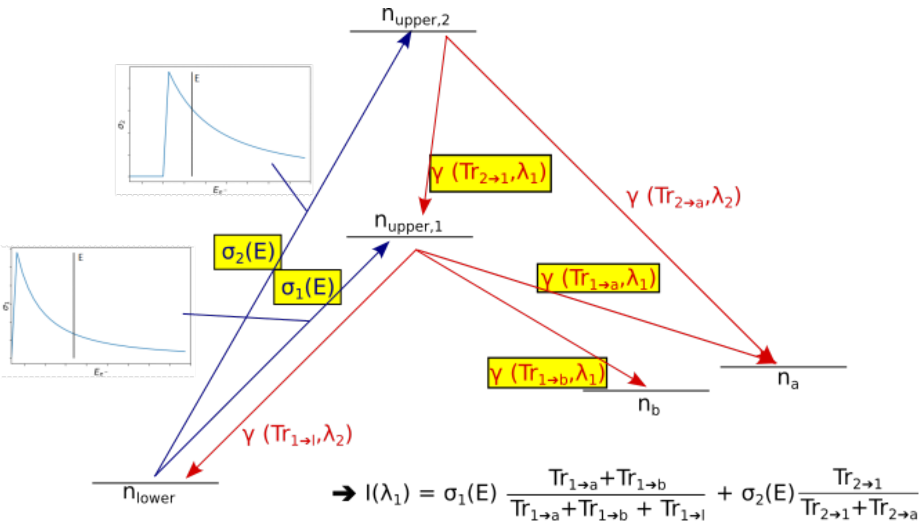

Figure 7.6: Schematic depiction of the second model used to obtain theoretical values for the electron dependant line intensities observed in the experiment. In this simple example, all ions are initially in the electronic configuration n_{lower}. From there two excitation pathways are shown, with the electron energy dependant cross sections $\sigma_1(E)$ and $\sigma_2(E)$ given as insets, ending in the upper states $n_{\text{upper},1}$ and $n_{\text{upper},2}$. Several radiative transitions originating from those states are shown. When evaluating the spectral intensity at the electron energy E, also marked in the inset, in the wavelength region λ_1, the result shown at the bottom is recovered.

the initial energy-onset of the intensity, as well as the behavior of the intensity with increasing electron energy is recovered well. The result of the model calculation for Sn^{14+} and comparison to the complete spectrum in the case of the measurement focusing on Sn^{14+} is shown in the upper panel of Figure 7.7. The lower panel in the same Figure shows the comparison for the wavelength window from 12 nm to 13 nm. At higher energies again, there is an increasing discrepancy between the model and the experimental projection observed again. The continued assumption is, that more higher lying states would need to be included, especially in the 5-shell or 6-shell, to reproduce those increases in the experimental spectral intensity.

The fact, that the agreement is best for the complete projection of the whole spectrum and much worse for small wavelength regions, may be attributed to the missing inclusion of cascades in this simple model. For example, when a sufficient electron energy is reached to produce the upper states which radiate brightly in the main line region, the decays of those excited states will populate other states, which could then radiate preferably in different wavelength regions. Then the assumed model breaks down when selecting a wavelength region excluding the main line, to only look at the behavior in different wavelength regions. An improvement would therefore be to include cascade effects. This in turn would again introduce a time dependant evolution as a complete path through the cascade all the way to the ground state can not at all be assumed to be instantaneous. During the cascade, the electron energy will change again, changing the available excitation channels. This energy-time-dependence will greatly complicate the model and still needs to be implemented, together with

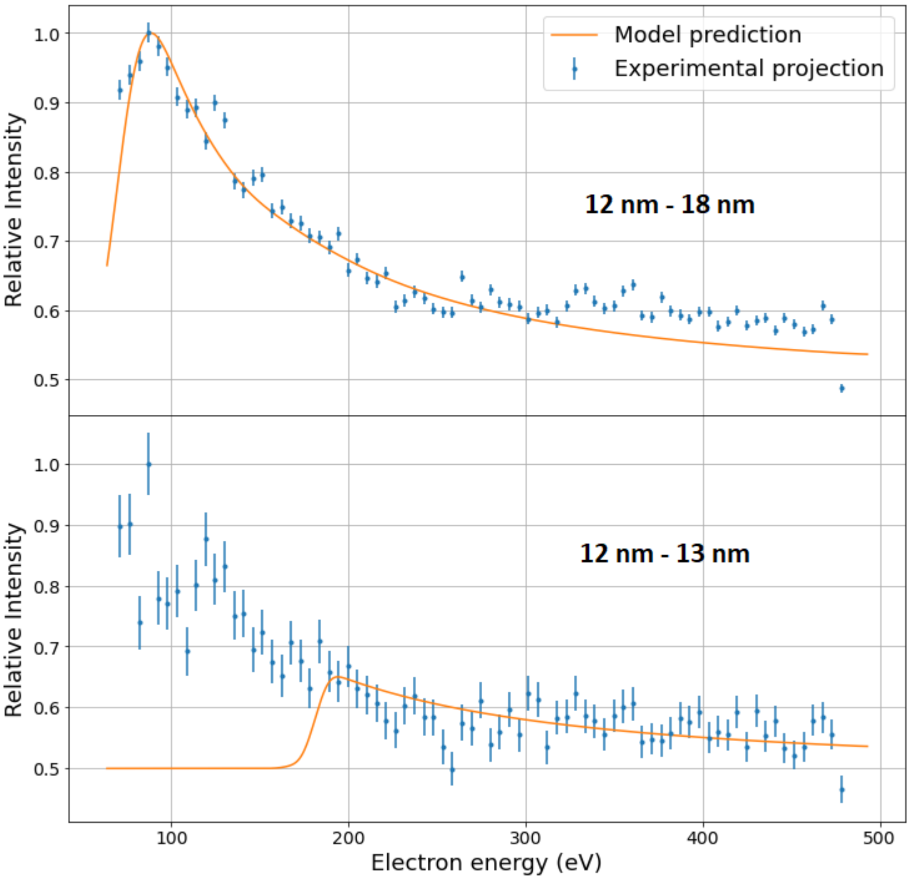

Figure 7.7: Top: Projection of all recorded events for the measurement focusing on Sn^{14+} and prediction of the intensity variation using the second model described in the main text. **Bottom:** Projection of all events in the wavelength region of 12 nm - 13 nm and the corresponding model prediction. The predicted intensities are folded with a gaussian with a width of $\sigma = 30\,\text{eV}$ and $\sigma = 10\,\text{eV}$ respectively, to account for the electron energy uncertainty observed in the experiment and the width of energy ensembles.

additional improvements discussed in the outlook.

Nonetheless, as this second model seems to recover the overall intensity variation quite well, a comparison can be done to the distribution of the found thresholds depicted in Figure 6.12. By compiling each excitation pathway in the new model and weighting those pathways with the oscillator strength of the transition as well as the population of the lower state, which gets excited, during the breeding phase, one obtains an analogous distribution to the one experimentally determined. Threshold energies can be defined by the energy difference of the involved levels for each of the calculated collisional excitation channels as

$$\Delta E = E_{\text{upper}} - E_{\text{lower}} \tag{7.3}$$

The relative oscillator strength for each of these excitation pathways can be calculated again from the excitation cross section at the energy threshold via

$$f_{if} \propto \frac{\sigma_{\text{exc}}(\Delta E)}{\Delta E^2} \tag{7.4}$$

Note here, that the collisional excitation cross section for each channel is only calculated for 32 discrete energy values. For the determination of the individual oscillator strength, the cross section value at the discrete energy value nearest to the threshold energy has been chosen. When comparing the intensity of the different radiation thresholds to experimental results, these oscillator strengths have been weighted by the population of the lower state $n_l(E_{\text{breed}})$ as well (see equation 7.1).

The results for the distribution of production thresholds given by the model for all five investigated charge states is displayed in Figure 7.8, where the threshold occurences have been additionally weighted by the relative abundance of the charge states over the five fast measurements, as determined in section 6.1: Sn^{11+}: 18.8 %, Sn^{12+}: 33.1 %, Sn^{13+}: 16.9 %, Sn^{14+}: 17.0 %, Sn^{15+}: 14.3 %. The contributions of other charge states are disregarded, as there are no calculations done for them with this second model and their abundance during the fast scans should be low due to the choice of breeding energies. As a comparison, the combined occurrences of thresholds as displayed in Figure 6.12 is also shown.

The initial block of thresholds, which is attributed mostly to collisional excitations from the ground state to singly excited states is recovered well in the model prediction. There, as well as in the experimentally determined distribution, most radiation originates from thresholds at an electron energy of approximately 75 eV. At higher energies, both in the experimental observation and in the model prediction, far fewer thresholds, or thresholds with far smaller corresponding oscillator strengths, are found. Some groups of thresholds at around 120 eV and 150 eV, which are found in the experiment are also contained in the model. Still, many excitation thresholds, which are observed in the experiment are not predicted in the model, such as the prominent group at 90 eV. Also at higher energies, some features are missing in the model prediction. As the overall shape of the distribution however is the same, the principle behind the theoretical model seems to grasp the origin of the threshold formation in the recorded spectra well.

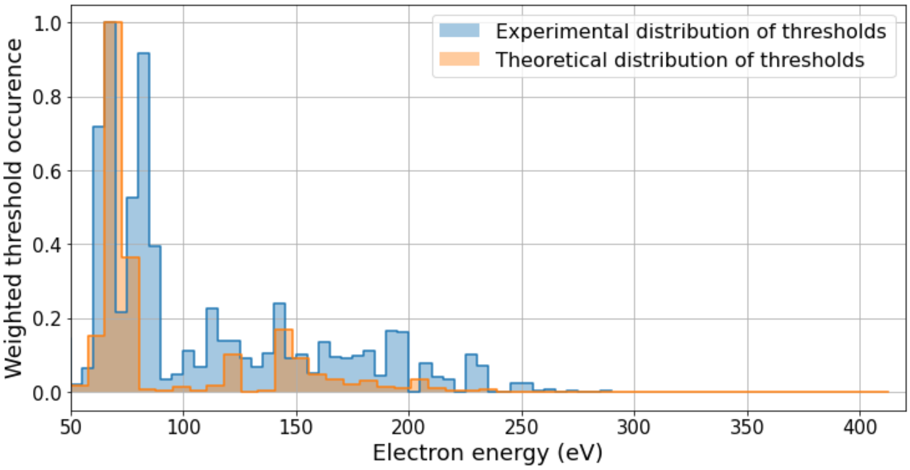

Figure 7.8: The distribution of radiation thresholds as observed in the fast scans compared to the results from the second model. The theoretical results encompass a mixture of the results for the individual charge states, replicating the same charge state mixture as in the compilation of the fast measurements. Displayed is the sum of all oscillator strengths for excitation processes with a threshold energy in 5 eV-energy windows, weighted by the individual lower state population and the relative abundance of the charge state. As a comparison the sum of all thresholds found in the fast scans, as depicted in Figure 6.12 is also shown.

This second model delivers a confirmation of the driving factors behind the observed radiation being radiative decay of excited states produced via collisional excitation and correctly predicts the initial threshold for radiation production and certain additional thresholds occuring at higher energies. Further, an inclusion of missing features and correct predictions when only evaluating small wavelength regions should be achievable when including more states and cascades into the model.

Chapter 8

Discussion & Outlook

8.1 Importance of Multiply Excited States

For many of the projections presented in this work, sufficient descriptions of line intensities in dependence of the electron kinetic energy were only possible when including the radiation coming from additional thresholds at higher energies.
This in turn means, that at high average electron energies, the contributions of multiply excited states to the spectrum of several highly charged tin ion species may not be neglected, even when discussing low density plasmas, such as the ones produced inside an EBIT.
A similar trend was observed for a multitude of different tin charge states produced in the different measurements. Therefore it can be stated, that multiply excited states indeed contribute to a significant degree to the industrially relevant EUV spectrum originating from laser-produced tin plasmas containing those charge states. However, the properties of the plasmas are significantly different, leading to a different magnitude in these contributions.

8.2 Comparison to the Results of Theoretical Studies on Laser-Produced-Plasmas

As presented in the beginning, the theoretical work in [97] and [108] predicts most of the radiation in the industrially relevant 13.5 nm-wavelength band in laser-produced plasmas to originate from transitions originating from multiply excited states.
The radiation stemming from additional thresholds found in this work proved to have total oscillator strengths comparable to transitions from singly excited states to the ground state. While the spectrum overall didn't change significantly, the persistence of existing lines at higher energies showed the importance of the contribution of these multiply excited states.
One major difference in the methodology between the experiment conducted in this work and the calculations in [97] is the energy distribution of the free electrons, as well as the plasma density. The conditions in the laser produced plasma yield electrons of a very high temperature and thus high average kinetic energy. This fact in turn leads to larger populations of electronic states of high

energies in laser-produced plasmas compared to the EBIT plasma. Furthermore a higher density of ions and electrons leads to large increases in the amounts of collisions. Therefore the production of multiply excited states via chains of several excitation processes becomes much more prevalent. This increases the production rates of those multiply excited states and therefore increases their contributions to the observable spectra of laser produced tin plasmas.

Contrary to these conditions, inside the EBIT, the electron kinetic energy was controlled tightly. With the electron energy having a gaussian distribution and an average energy in the range of the excitation thresholds, the populations of the multiply excited states tend to be much lower than in the usual laser produced plasmas. Additionally the density of tin ions in the generated plasma is a lot lower than in the case of laser-produced-plasmas, further contributing to a difference in the magnitude of the population of multiply excited states. The reason behind that is the difference in populating and depopulating rates of excited states in these cases [36]. In the case of a thin plasma, most excited states are depopulated via spontaneous emission on a timescale given by the radiative lifetime of the excited state. During these lifetimes, usually no collisional interactions with other ions or electrons take place (except for long-lived metastable states). In high density plasmas however, collision rates are much higher and thus it is common to have collisional excitations from already excited states, before they can decay spontaneously back to the ground state.

A direct comparison of the assumed parameters in the study on laser-produced-plasmas and the assumed conditions inside the EBIT shows those stark contrasts.

Table 8.1: Plasma conditions as found in a typical laser-produced plasma (e.g. as assumed in [108]) compared to the conditions inside an EBIT as observed in this work.

Parameter	Laser-produced-plasma	EBIT
Electron density	$\approx 1 \cdot 10^{20} \, \frac{1}{\mathrm{cm}^3}$	$\approx 1 \cdot 10^{10} \, \frac{1}{\mathrm{cm}^3}$
Ion density	$\approx 1 \cdot 10^{11} \, \frac{1}{\mathrm{cm}^3}$	$\approx 5 \cdot 10^{9} \, \frac{1}{\mathrm{cm}^3}$
Electron energy distribution	Maxwellian, $T \approx 32\,\mathrm{eV}$	Gaussian, $\sigma \approx 5\,\mathrm{eV}$

A calculation of the state populations using the CRM employed throughout, for the example of Sn^{13+} with states included in the calculation as given in Table 7.1 for these to sets of plasma properties gives an impression of their influence of the state balance. The results of this calculation are shown in Figure 8.1, with the calculated density of states of Sn^{13+} given at the bottom. On top, the relative populations for the properties as given in the EBIT and in the typical laser produced plasma is shown.

There the increased population of multiply excited states in the laser produced plasma is apparent, whereas at EBIT-conditions almost all ions are in their ground state. The energy region including the ground state was in both cases the most populated region at a relative population of one.

8.3 Discussion of the Experiment

The experimental method and data analysis presented in this work could still be improved upon. On several occasions, a lack of resolution is apparent, both

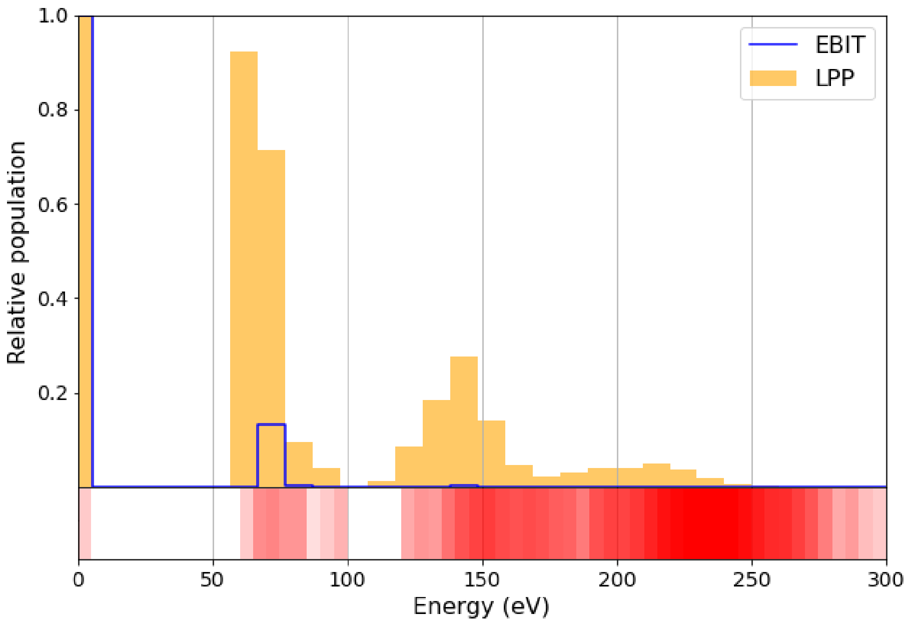

Figure 8.1: Top: Relative state populations of Sn^{13+}-ions in plasmas with properties as typical for EBITs or laser produced plasmas. The results were calculated using the CRM with the included configurations as given in Table 7.1 for both cases. **Bottom:** Calculated density of states of Sn^{13+} in a logarithmic color scale.

in terms of wavelength resolution of the EUV spectrometer, as well as in terms of the electron energy determination.

Prior works with FLASH-EBIT had much lower line uncertainties in the EUV regime ([92], [64]) while using a CCD (charge-coupled-device) [48] instead of an MCP as a detector for the EUV-spectrometer. Therefore it can be assumed that the main problem in wavelength determination comes from the impurities of the MCP. Although these impurities were tried to be compensated for in section 4.2, still a fluctuation of the calibration lines around the fit was observed, independent of the order of the used polynomial for the fit. Therefore, if one wants higher accuracy in terms of wavelength determination of lines, the CCD setup would be superior.

However, the MCP was chosen here due to its ability to provide a timing information for each detected event to a degree which would not be possible with a CCD. Fast switching scans with breeding and ramping phases make for the need of such a timing information, to relate the observed events to the electron energy.

An additional improvement of the experimental setup would consist of an extraction beamline for direct determination of the charge state balance in the trap, via $\frac{q}{m}$ - separation of ions, as for example used in [94] or [107]. This setup would give the direct information about the relative abundance of the different tin ion charge states during the experimental scans, allowing for a better optimization of the parameters for those yields. Here only the influence of changing the electron beam energy at one specific electron density on the abundance has been estimated, using the conducted NMF in section 5. With an extraction beamline this estimation could be conducted more accurately. Also the effects of other parameters on the charge state distribution, like breeding and scan duration or different electron densities, could be determined, to better optimize the experiment for the different ionic species. Right now, the existing extraction beamline at FLASH-EBIT needs extensive refurbishment to function properly again and be used in successive studies.

The statistical significance of the individual projections for the individual measurements in this thesis could also be improved upon. This was especially apparent, as the data for the individual projections onto the electron energy needed to be binned heavily, in order to observe trends in the relative intensities. Without such a binning, statistical uncertainties would be to high to find conclusive signs of the additional thresholds. This binning however also reduces the ability to accurately determine the exact energy values of the additional thresholds and prohibited the extraction of fit uncertainties for the fits with multiple Van Regemorter relations.

During the measurement at least 80 % of the time needed to be invested into the breeding phase to obtain relatively pure tin charge state populations. Then, from the remaining 20 % of events, all events outside of a circular region of interest, smaller than the detector itself, needed to be discarded due to strong distortions at the detector edges. And then from these remaining data sets, slices in wavelength space were taken, to be projected onto the electron energy axis, where every single bin still needs a significant amount of counts for high statistics. Therefore the overall amount of events which needed to be collected for the determination of the behavior of the relative collision excitation cross sections was enormous. Even at measurement times of roughly two weeks per scan, which was set for the acquisition of the data in this thesis, the noise in the individual projections was still pretty significant.

Improvements of the experiment could therefore include a larger collection angle for photons or even longer measurement times, in order to improve the signal to noise ratio.

Nonetheless, compilation of the data from multiple measurements as well as the compilation of the fit results from many different projections allowed to extract overall trends in the contributions of multiply excited states.

Additional work also needs to be done on the theoretical side. Many of the theoretical projections produced using the collisional radiative model did not resemble the experimental results, as crucial features were left unexplained. Often, the initial onset of the spectral lines found in the experimental spectra were not reproduced. Even in cases, where this initial onset was present in the theoretical as well as in the experimental projection, additional features at higher electron energies were left unexplained by the theoretical modeling, hinting at additional higher lying states, that contribute significantly to the tin spectrum but were left out in the present calculations. More extensive calculations, including more highly excited states, might lead to those features also appearing in the theoretical cross sections. Including calculations for more different charge states may also help in the effort of explaining those features, as the charge state distribution during the measurements may have been broader than expected.

Also the second model presented here, taking into account the state distribution during the breeding phase must still be expanded upon. The assumptions made in that model will overestimate the prevalence of the electronic states produced during the breeding phase, as the population distribution is assumed to be unchanged during the scanning phase. In reality however, the metastable states produced during the breeding phase will decay over scanning time and the states produced at the energies in the scanning phase will also significantly alter the state balance. Both of these effects were neglected. Also, to get a true comparison to the intensity evolution at different electron energies in the experiment for different wavelength regions, cascades would need to be rigorously included in the model, including the time dependence of the light emitted via the cascades.

Thus, in the end, a synthesis of both presented models would suit best to reproduce the experimental data, including both the cascades included in the CRM, as well as a population distribution, somewhere between the one during the breeding phase and the distribution calculated when treating the scanning phase as a slow energy variation, with a steady state distribution at each energy.

Using measurements of relative collisional excitation cross sections gave insights into the level structure of tin charge states between Sn^{11+} to Sn^{15+} and the contributions of the different excited states to the EUV spectrum. Although a discussion of the structure of the individual charge states based on the taken data is hardly possible, due to the found mixture of charge states inside the trap, the structure and spectra of the group of charge states as a whole can be discussed. As expected from their similarities in the calculated atomic structure, the distribution of thresholds extracted via the electron collisional excitation cross section measurements were quite similar. The energy thresholds found for the production of radiation agreed with the calculated density of states and the prediction of the threshold energies using the second model.

8.4 Future Work

As part of the space charge determination in section 4.5, dielectronic recombination of tin has been observed. The observed resonances turned out to be MNn-resonances after comparison to FAC calculations. More resonances can be found at higher electron energies, for which preliminary measurements have been conducted, as given in 8.2.

Extensive calculations are needed, as well as several measurements for the investigation of dielectronic recombination in multiple charge states. Such dielectronic recombination measurements are valuable, as in any plasma, dielectronic recombination plays a crucial role in setting the charge balance [25] and is notoriously difficult to calculate when including recombination into shells of high n [3] [93], such as the N-shell (n=4). This provides the need for experimental benchmarks, which could be delivered in future experiments with the same methodology. A deeper understanding of which charge states and to an extent. which electronic states are involved in these dielectronic recombinations can also help to understand the state balance during the experiments presented here and could be used to refine the assumed populations in the theoretical models.

At several points of this thesis, the relevance of metastable states to the electronic state balance in highly charged tin became apparent. During the work

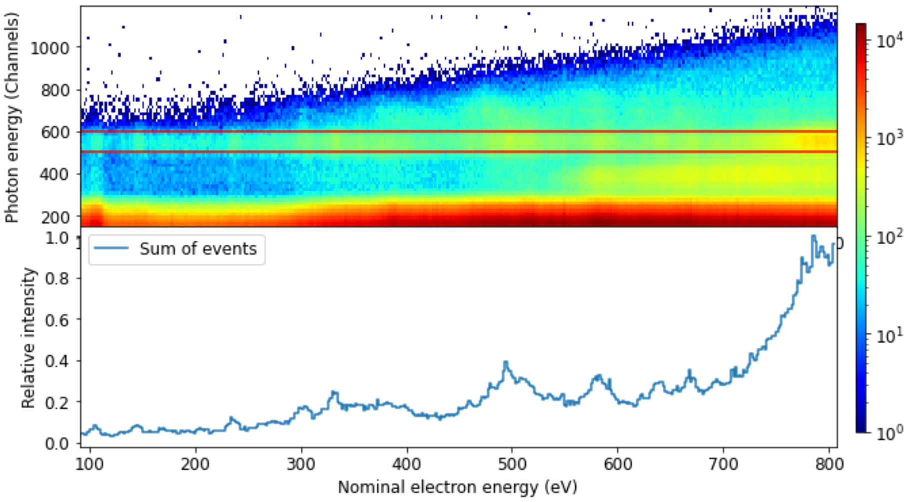

Figure 8.2: Dielectronic recombination measurement up to 800 eV. Many dielectronic resonances of highly charged tin are captured, which warrants further investigation.

presented here, additionally direct measurements of lifetimes of metastable states were attempted, using the EBIT in magnetic trapping mode [5]. The electron beam was switched on and off and the time dependant EUV spectrum after switching off the electron beam was recorded. One would expect spectral lines originating from metastable states to still be present after the switch, with exponentially decaying intensity. However, such behavior was not observed and overall line strengths during these measurements very low. Presumedly the signal was low due to insufficient trapping of the ions. Continuing and improving on these measurements could deliver additional information on the prevalence of metastable states in tin plasmas, and could confirm the hypothesis that those were responsible for the production of several tin charge states at lower electron energy than expected. Then also their role in influencing the electron energy dependant line intensities could become tractable.

Determination of absolute excitation cross sections and absolute oscillator strengths for the presented transitions can also still be achieved with additional measurements. Taking measurements at varying injection pressures while measuring the space charge compensation by the positive ions inside the trap may give insight on the ion density in the trap. Together with the estimated electron density and a comparison to lines of known strength, for example in oxygen, might allow such a calibration, to convert the relative quantities given here into absolutes.

The methods explained in this thesis could also be extended to further elements and ionic species. This may in turn help to understand the structure of ever more complex systems. An example for an application for lines produces by such complex, high Z ions is the further extension of the energies used for the production of light in nanolithographic applications, in an effort to imprint even smaller features than using the 13.5 nm-wavelength band. One example for a candidate for an ion usable for this effort is Gadolinium. Spectra can be seen for example in [104].

Chapter 9

Bibliography

[1] R. S. Abhari, B. Rollinger, A. Z. Giovannini, O. Morris, I. Henderson, and S. S. Ellwi. Laser-produced plasma light source for extreme-ultraviolet lithography applications. *Journal of Micro/Nanolithography, MEMS, and MOEMS*, 11(2):021114, 2012.

[2] M. Altunbulak and A. Klyachko. The pauli principle revisited. *Communications in Mathematical Physics*, 282(2):287–322, 2008.

[3] C. Ballance, S. Loch, M. Pindzola, and D. Griffin. Dielectronic recombination of w35+. *Journal of Physics B: Atomic, Molecular and Optical Physics*, 43(20):205201, 2010.

[4] M. Bartelmann, B. Feuerbacher, T. Krüger, D. Lüst, A. Rebhan, and A. Wipf. *Theoretische Physik 2— Elektrodynamik*. Springer, 2018.

[5] P. Beiersdorfer, L. Schweikhard, J. C. López-Urrutia, and K. Widmann. The magnetic trapping mode of an electron beam ion trap: New opportunities for highly charged ion research. *Review of Scientific Instruments*, 67(11):3818–3826, 1996.

[6] O. Bely and H. Van Regemorter. Excitation and ionization by electron impact. *Annual Review of Astronomy and Astrophysics*, 8(1):329–368, 1970.

[7] F. A. Berezin and M. Shubin. *The Schrödinger Equation*, volume 66. Springer Science & Business Media, 2012.

[8] S. Bernitt. *Resonante anregung astrophysikalischer röntgen-Übergänge in hochgeladenen eisenionen mit dem freie-elektronen-laser lcls.* PhD thesis, 2013.

[9] M. Blaha. Effective gaunt factors g_ {eff} for excitation of positive ions by electron collisions in a simplified coulomb-born approximation. *The Astrophysical Journal*, 157:473, 1969.

[10] M. A. Blessenohl. *Fine-structure investigations in highly charged ions using spectroscopy in the vacuum ultraviolet regime.* PhD thesis, 2020.

[11] M. Blume and R. Watson. Theory of spin-orbit coupling in atoms i. derivation of the spin-orbit coupling constant. *Proceedings of the Royal Society of London. Series A. Mathematical and Physical Sciences*, 270(1340):127–143, 1962.

[12] K. Bockasten and K. B. Johansson. The spectrum of o v. *Ark. Fys. (Stockholm)*, 38:563–584, 1968.

[13] N. Bohr. I. on the constitution of atoms and molecules. *The London, Edinburgh, and Dublin Philosophical Magazine and Journal of Science*, 26(151):1–25, 1913.

[14] C. Brown, S. Tilford, and M. L. Ginter. Absorption spectrum of sn i between 1580 and 2040 å. *JOSA*, 67(5):607–621, 1977.

[15] E. H. S. Burhop. *The Auger effect and other radiationless transitions.* CUP Archive, 1952.

[16] S. Churilov and Y. Joshi. Revised and extended analysis of eight-times ionized barium: Ba ix and nine-times ionized barium: Ba x. *Physica Scripta*, 62(4):282, 2000.

[17] S. Churilov, Y. Joshi, and R. Gayasov. Analysis of seven-times-ionized barium: Ba viii. *JOSA B*, 18(1):113–120, 2001.

[18] S. Churilov, Y. Joshi, and A. Ryabtsev. The 4d10 1s0-4d9 (np+ n'f) transitions in the pd i isoelectronic sequence from cd iii to cs x. *Journal of Physics B: Atomic, Molecular and Optical Physics*, 27(22):5485, 1994.

[19] W. Colson, J. McPherson, and F. King. High-gain imaging electron multiplier. *Review of scientific instruments*, 44(12):1694–1696, 1973.

[20] J. R. Crespo López-Urrutia and Z. Harman. Emission and laser spectroscopy of trapped highly charged ions in electron beam ion traps. In *Fundamental Physics in Particle Traps*, pages 315–373. Springer, 2014.

[21] F. J. Currell. *The Physics of Multiply and Highly Charged Ions: Volume 1: Sources, Applications and Fundamental Processes*, volume 1. Springer Science & Business Media, 2003.

[22] W. Demtröder. *Atoms, molecules and photons*, volume 3. Springer, 2010.

[23] G. Doggett and B. Sutcliffe. A modern approach to ls coupling in the theory of atomic spectra. *Journal of chemical education*, 75(1):110, 1998.

[24] J. P. Donohoe. A laboratory experiment to demonstrate gauss's law for electric fields. *American Journal of Physics*, 76(10):963–967, 2008.

[25] J. Dubau and S. Volonte. Dielectronic recombination and its applications in astronomy. *Reports on Progress in Physics*, 43(2):199, 1980.

[26] H. Egger, T. Luk, K. Boyer, D. Muller, H. Pummer, T. Srinivasan, and C. Rhodes. Picosecond, tunable arf* excimer laser source. *Applied Physics Letters*, 41(11):1032–1034, 1982.

[27] S. Epp. *Röntgen-Laserspektroskopie hochgeladener Ionen in einer EBIT am Freie-Elektronen-Laser FLASH.* PhD thesis, Ruprecht-Karls Universität Heidelberg, 2007.

[28] S. Epp, J. C. López-Urrutia, M. Simon, T. Baumann, G. Brenner, R. Ginzel, N. Guerassimova, V. Mäckel, P. Mokler, B. Schmitt, et al. X-ray laser spectroscopy of highly charged ions at flash. *Journal of Physics B: Atomic, Molecular and Optical Physics*, 43(19):194008, 2010.

[29] T. Feigl, S. Yulin, N. Benoit, and N. Kaiser. Euv multilayer optics. *Microelectronic Engineering*, 83(4-9):703–706, 2006.

[30] C. F. Fischer. Hartree–fock method for atoms. a numerical approach. 1977.

[31] K. Flamm. Has moore's law been repealed? an economist's perspective. *Computing in Science & Engineering*, 19(2):29–40, 2017.

[32] T. Fließbach. *Quantenmechanik: Lehrbuch zur Theoretischen Physik III.* Springer-Verlag, 2018.

[33] J. Fraunhofer. Bestimmung des brechungs-und des farbenzerstreungsvermögens verschiedener glasarten, in bezug auf die vervollkommnung achromatischer fernröhre. *Annalen der Physik*, 56(7):264–313, 1817.

[34] H. Friedrich and H. Friedrich. *Theoretical atomic physics*, volume 3. Springer, 2006.

[35] S. Fritzsche, P. Palmeri, and S. Schippers. Atomic cascade computations. *Symmetry*, 13(3):520, 2021.

[36] T. Fujimoto. Plasma spectroscopy. In *Plasma Polarization Spectroscopy*, pages 29–49. Springer, 2008.

[37] D. Gaspard. Connection formulas between coulomb wave functions. *Journal of mathematical physics*, 59(11):112104, 2018.

[38] M. F. Gu. Indirect x-ray line-formation processes in iron l-shell ions. *The Astrophysical Journal*, 582(2):1241, 2003.

[39] M. F. Gu. The flexible atomic code. *Canadian Journal of Physics*, 86(5):675–689, 2008.

[40] Y. Hahn and K. LaGattuta. Dielectronic recombination and related resonance processes. *Physics reports*, 166(4):195–268, 1988.

[41] S. Hansen, J. Bauche, C. Bauche-Arnoult, and M. Gu. Hybrid atomic models for spectroscopic plasma diagnostics. *High Energy Density Physics*, 3(1-2):109–114, 2007.

[42] T. Harada, K. Takahashi, H. Sakuma, and A. Osyczka. Optimum design of a grazing-incidence flat-field spectrograph with a spherical varied-line-space grating. *Applied optics*, 38(13):2743–2748, 1999.

[43] K. Haris, A. Kramida, and A. Tauheed. Extended and revised analysis of singly ionized tin: Sn ii. *Physica Scripta*, 89(11):115403, 2014.

[44] K. Haris and A. Tauheed. Revised and extended analysis of doubly ionized tin: Sn iii. *Physica Scripta*, 85(5):055301, 2012.

[45] J. He and Q. Zhang. An exact calculation of the voigt spectral line profile in spectroscopy. *Journal of Optics A: Pure and Applied Optics*, 9(7):565, 2007.

[46] G. Herrmann. Optical theory of thermal velocity effects in cylindrical electron beams. *Journal of Applied Physics*, 29(2):127–136, 1958.

[47] J. Hobson. Cryopumping. *Journal of Vacuum Science and Technology*, 10(1):73–79, 1973.

[48] S. B. Howell. *Handbook of CCD astronomy*, volume 5. Cambridge University Press, 2006.

[49] Q. Huang, V. Medvedev, R. van de Kruijs, A. Yakshin, E. Louis, and F. Bijkerk. Spectral tailoring of nanoscale euv and soft x-ray multilayer optics. *Applied physics reviews*, 4(1):011104, 2017.

[50] W. Johnson and G. Soff. The lamb shift in hydrogen-like atoms, 1 z 110. *Atomic Data and Nuclear Data Tables*, 33(3):405–446, 1985.

[51] T. Kinoshita. The fine structure constant. *Reports on Progress in Physics*, 59(11):1459, 1996.

[52] D. Knapp, P. Beiersdorfer, M. Chen, J. Scofield, and D. Schneider. Observation of interference between dielectronic recombination and radiative recombination in highly charged uranium ions. *Physical review letters*, 74(1):54, 1995.

[53] D. H. Kobe and V. Aguilera-Navarro. Derivation of the energy-time uncertainty relation. *Physical Review A*, 50(2):933, 1994.

[54] M. G. Kozlov, S. Porsev, M. Safronova, and I. Tupitsyn. Ci-mbpt: A package of programs for relativistic atomic calculations based on a method combining configuration interaction and many-body perturbation theory. *Computer Physics Communications*, 195:199–213, 2015.

[55] M. Kretzschmar. Particle motion in a penning trap. *European Journal of Physics*, 12(5):240, 1991.

[56] P. Kunz and E. Rost. The distorted-wave born approximation. In *Computational Nuclear Physics 2*, pages 88–107. Springer, 1993.

[57] L. Lamata, J. León, T. Schätz, and E. Solano. Dirac equation and quantum relativistic effects in a single trapped ion. *Physical review letters*, 98(25):253005, 2007.

[58] A. Lapierre, J. Crespo López-Urrutia, T. Baumann, S. Epp, A. Gonchar, A. González Martínez, G. Liang, A. Rohr, R. Soria Orts, M. Simon, et al. Compact soft x-ray spectrometer for plasma diagnostics at the heidelberg electron beam ion trap. *Review of Scientific Instruments*, 78(12):123105, 2007.

[59] A. Laska. Program for the combinatoric assignment of ls-and jj-coupling term symbols. Master's thesis, 2012.

[60] A. Lawrence. Counting statistics: Binomial and poisson distributions. In *Probability in Physics*, pages 55–68. Springer, 2019.

[61] J. Lawson. Perveance and the bennett pinch relation in partially-neutralized electron beams. *International Journal Of Electronics*, 5(2):146–151, 1958.

[62] P. Lechner, C. Fiorini, R. Hartmann, J. Kemmer, N. Krause, P. Leutenegger, A. Longoni, H. Soltau, D. Stötter, R. Stötter, et al. Silicon drift detectors for high count rate x-ray spectroscopy at room temperature. *Nuclear Instruments and Methods in Physics Research Section A: Accelerators, Spectrometers, Detectors and Associated Equipment*, 458(1-2):281–287, 2001.

[63] D.-T. Lee and B. J. Schachter. Two algorithms for constructing a delaunay triangulation. *International Journal of Computer & Information Sciences*, 9(3):219–242, 1980.

[64] G. Liang, J. C. López-Urrutia, T. Baumann, S. Epp, A. Gonchar, A. Lapierre, P. Mokler, M. Simon, H. Tawara, V. Mäckel, et al. Experimental investigations of ion charge distributions, effective electron densities, and electron–ion cloud overlap in electron beam ion trap plasma using extreme-ultraviolet spectroscopy. *The Astrophysical Journal*, 702(2):838, 2009.

[65] Y. Liu, K. Yao, R. Hutton, and Y. Zou. Numerical simulations using an improved calculational scheme for ion charge state distribution and ion temperature evolution in an ebit. *Journal of Physics B: Atomic, Molecular and Optical Physics*, 38(17):3207, 2005.

[66] W. Lotz. An empirical formula for the electron-impact ionization cross-section. *Zeitschrift für Physik*, 206(2):205–211, 1967.

[67] A. D. MacDonald. Properties of the confluent hypergeometric function. 1948.

[68] R. A. Mapleton. Theory of charge exchange. Technical report, National Standard Reference Data System, 1971.

[69] J. Mawhin and A. Ronveaux. Schrödinger and dirac equations for the hydrogen atom, and laguerre polynomials. *Archive for history of exact sciences*, 64(4):429–460, 2010.

[70] P. W. Milonni. Why spontaneous emission? *American Journal of Physics*, 52(4):340–343, 1984.

[71] B. L. Moiseiwitsch and S. J. Smith. Electron impact excitation of atoms. *Reviews of Modern Physics*, 40(2):238, 1968.

[72] C. E. Moore. Atomic energy levels. as derived from the analyses of optical spectra. volume 3. Technical report, NATIONAL BUREAU OF STANDARDS GAITHERSBURG MD, 1958.

[73] G. Moore. Moore's law. *Electronics Magazine*, 38(8):114, 1965.

[74] G. E. Moore. Lithography and the future of moore's law. *IEEE Solid-State Circuits Society Newsletter*, 11(3):37–42, 2006.

[75] C. Müller. *Spherical harmonics*, volume 17. Springer, 2006.

[76] N. Murphy, P. Niga, A. Cummings, P. Dunne, and G. O'Sullivan. 4d→ 5p transitions in the euv photoabsorption spectrum of ba iv, ba v and ba vi. *Journal of Physics B: Atomic, Molecular and Optical Physics*, 39(2):365, 2005.

[77] P. A. Packan. Pushing the limits. *Science*, 285(5436):2079–2081, 1999.

[78] V. P. Pauca, J. Piper, and R. J. Plemmons. Nonnegative matrix factorization for spectral data analysis. *Linear algebra and its applications*, 416(1):29–47, 2006.

[79] W. Pauli. Über den zusammenhang des abschlusses der elektronengruppen im atom mit der komplexstruktur der spektren. *Einführung und Originaltexte*, page 229, 1925.

[80] G. Peach, H. Saraph, and M. Seaton. Atomic data for opacity calculations. ix. the lithium isoelectronic sequence. *Journal of Physics B: Atomic, Molecular and Optical Physics*, 21(22):3669, 1988.

[81] B. Penetrante, J. Bardsley, D. DeWitt, M. Clark, and D. Schneider. Evolution of ion-charge-state distributions in an electron-beam ion trap. *Physical Review A*, 43(9):4861, 1991.

[82] B. Povh, K. Rith, C. Scholz, F. Zetsche, and W. Rodejohann. Particles and nuclei. *An Introduction to the Physical Concepts, Berlin and Heidelberg: Springer-Verlag (Italian Translation:(1998), Particelle e nuclei. Un'introduzione ai concetti sici, Torino: Bollati Boringhieri editore)*, 1995.

[83] J. R. Powell. The quantum limit to moore's law. *Proceedings of the IEEE*, 96(8):1247–1248, 2008.

[84] Y. Ralchenko. Nist atomic spectra database. *Memorie della Societa Astronomica Italiana Supplementi*, 8:96, 2005.

[85] Y. Ralchenko. *Modern methods in collisional-radiative modeling of plasmas*, volume 90. Springer, 2016.

[86] U. Ritgen. Fehlerfortpflanzung nach gauß. In *Analytische Chemie II*, pages 249–258. Springer, 2020.

[87] G. Rodrigues, P. Indelicato, J. Santos, P. Patté, and F. Parente. Systematic calculation of total atomic energies of ground state configurations. *Atomic Data and Nuclear Data Tables*, 86(2):117–233, 2004.

[88] RoentDek Handels GmbH, Im Vogelshaag 8; D-65779 Kelkheim-Ruppertshain; Germany. *MCP Delay Line Detector Manual*, version 11.0.2208.1 edition.

[89] F. B. Rosmej, V. A. Astapenko, and V. S. Lisitsa. *Plasma Atomic Physics*, volume 650. Springer, 2021.

[90] J. Rubio and J. Perez. Energy levels in the jj coupling scheme. *Journal of Chemical Education*, 63(6):476, 1986.

[91] D. H. Sampson and H. L. Zhang. Use of the van regemorter formula for collision strengths or cross sections. *Physical Review A*, 45(3):1556, 1992.

[92] J. Scheers, C. Shah, A. Ryabtsev, H. Bekker, F. Torretti, J. Sheil, D. Czapski, J. Berengut, W. Ubachs, J. C. López-Urrutia, et al. Euv spectroscopy of highly charged sn 13+- sn 15+ ions in an electron-beam ion trap. *Physical Review A*, 101(6):062511, 2020.

[93] S. Schippers, D. Bernhardt, A. Müller, C. Krantz, M. Grieser, R. Repnow, A. Wolf, M. Lestinsky, M. Hahn, O. Novotnỳ, et al. Dielectronic recombination of xenonlike tungsten ions. *Physical Review A*, 83(1):012711, 2011.

[94] M. Schwarz. *Photoionisation von neonartigem Argon in einer Elektronenstrahl-Ionenfalle.* PhD thesis, Ruprecht-Karls Universität Heidelberg, 2009.

[95] I. Shavitt. The method of configuration interaction. In *Methods of electronic structure theory*, pages 189–275. Springer, 1977.

[96] J. Sheil, O. Versolato, V. Bakshi, and H. Scott. Review of the 1st euv light sources code comparison workshop. *arXiv preprint arXiv:2208.12699*, 2022.

[97] J. Sheil, O. O. Versolato, A. J. Neukirch, and J. Colgan. Multiply-excited states and their contribution to opacity in co2 laser-driven tin-plasma conditions. *Journal of Physics B: Atomic, Molecular and Optical Physics*, 54(3):035002, 2021.

[98] P. E. Siegbahn. The configuration interaction method. In *Lecture notes in quantum chemistry*, pages 255–293. Springer, 1992.

[99] M. Simon, M. Schwarz, B. Schmitt, C. Beilmann, S. Epp, T. Baumann, K. Kubicek, R. Ginzel, S. Higgins, R. Klawitter, et al. Photoionization of ions in arbitrary charge states by synchrotron radiation in an electron beam ion trap. In *Journal of Physics: Conference Series*, volume 194, page 012009. IOP Publishing, 2009.

[100] J. C. Slater. The theory of complex spectra. *Physical Review*, 34(10):1293, 1929.

[101] S. E. Sobottka and M. B. Williams. Delay line readout of microchannel plates. *IEEE Transactions on Nuclear Science*, 35(1):348–351, 1988.

[102] J. Stevenson and A. Gundlach. The application of photolithography to the fabrication of microcircuits. *Journal of Physics E: Scientific Instruments*, 19(9):654, 1986.

[103] L. Strüder, P. Lechner, and P. Leutenegger. Silicon drift detector–the key to new experiments. *The Science of Nature*, 85(11):539–543, 1998.

[104] C. Suzuki, F. Koike, I. Murakami, N. Tamura, S. Sudo, H. Sakaue, N. Nakamura, S. Morita, M. Goto, D. Kato, et al. Euv spectroscopy of highly charged high z ions in the large helical device plasmas. *Physica Scripta*, 89(11):114009, 2014.

[105] A. Temkin and A. Bhatia. Autoionization. *Springer Handbook of Atomic*, page 391, 2006.

[106] S. E. Thompson and S. Parthasarathy. Moore's law: the future of si microelectronics. *Materials today*, 9(6):20–25, 2006.

[107] M. Togawa. *Investigation of the M-shell unresolved transition array of aluminium-like iron using monochromatic soft x-ray synchrotron radiation.* PhD thesis, Ruprecht-Karls-Universität Heidelberg, 2021.

[108] F. Torretti, J. Sheil, R. Schupp, M. Basko, M. Bayraktar, R. Meijer, S. Witte, W. Ubachs, R. Hoekstra, O. Versolato, et al. Prominent radiative contributions from multiply-excited states in laser-produced tin plasma for nanolithography. *Nature communications*, 11(1):1–8, 2020.

[109] M. Totzeck, W. Ulrich, A. Göhnermeier, and W. Kaiser. Pushing deep ultraviolet lithography to its limits. *nature photonics*, 1(11):629–631, 2007.

[110] J. A. Tully, M. J. Seaton, and K. A. Berrington. Atomic data for opacity calculations. xiv. the beryllium sequence. *Journal of Physics B: Atomic, Molecular and Optical Physics*, 23(21):3811, 1990.

[111] P. P. Urone and R. Hinrichs. Limits of resolution: The rayleigh criterion. *College Physics*, 2012.

[112] Verolaĭ. Radiative lifetimes of excited states of atoms.

[113] O. O. Versolato. Physics of laser-driven tin plasma sources of euv radiation for nanolithography. *Plasma Sources Science and Technology*, 28(8):083001, 2019.

[114] C. Wagner and N. Harned. Lithography gets extreme. *Nature Photonics*, 4(1):24–26, 2010.

[115] E. W. Weisstein. Pauli matrices. *https://mathworld. wolfram. com/*, 2002.

[116] K. Winter. On distorted-wave approximations for excitation. *Journal of Physics B: Atomic and Molecular Physics (1968-1987)*, 11(1):149, 1978.

[117] F. X. Witkowski, L. J. Leon, P. A. Penkoske, R. B. Clark, M. L. Spano, W. L. Ditto, and W. R. Giles. A method for visualization of ventricular fibrillation: Design of a cooled fiberoptically coupled image intensified ccd data acquisition system incorporating wavelet shrinkage based adaptive filtering. *Chaos: An Interdisciplinary Journal of Nonlinear Science*, 8(1):94–102, 1998.

[118] J. L. Wiza et al. Microchannel plate detectors. *Nucl. Instrum. Methods*, 162(1-3):587–601, 1979.

[119] P. Zeeman. Xxxiii. doublets and triplets in the spectrum produced by external magnetic forces.—(ii.). *The London, Edinburgh, and Dublin Philosophical Magazine and Journal of Science*, 44(268):255–259, 1897.

Chapter 10

Appendix

10.1 Correction of the Intensity in the Fast Scans for the Varying Electron Currents

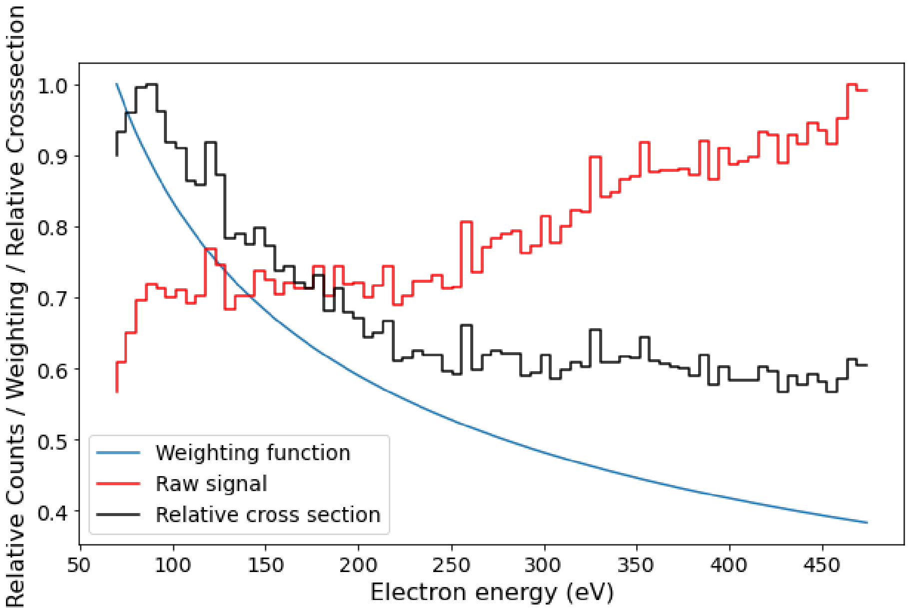

Figure 10.1: Correction of the number of events projected onto the electron beam energy. At each electron energy during the measurement cycle, the electron beam current is different. Hence, to extract the relative electron impact excitation cross section in this experiment, the event rate needs to be divided by this current. Here the multiplication with the defined weighting function converts the raw counts to relative cross sections.

Before displaying relative intensities as a function of the electron beam energy in section 6.3, the varying electron beam current during the scanning phase was corrected for. This is rescale the relative intensity to be proportional to the

electron impact excitation cross section. As discussed in section 3.4, in order to improve the confinement of the ions and thus experimental count rates, as well as having a well known electron beam energy at any point during the measurement, the space charge is being kept constant by varying the beam current.
As the excitation rate f, which determines the relative intensities of the recorded lines during the fast scans, depends not only on the likelihood of excitation upon collision between an ion and an electron, as expressed by the cross section, but also on the amount of possible collisions between exciting electrons and target ions, it is directly proportional to the electron current density j_{e^-}:

$$f \propto \sigma n_{\text{ion}} j_{e^-} \tag{10.1}$$

with the actual excitation cross section being σ and the target ion number density being n_{ion}. One can assume that the target density stays approximately constant, as the injection pressure is constant during the measurements and the scan duration is sufficiently short, for the charge state distribution to stay constant. Then one just needs to divide by the current density to find the relative cross section in dependence of the electron energy. This is done in all projections to be discussed. The influence this has on the individual projections can be seen in Figure 10.1.

10.2 Additional Figures and Tables

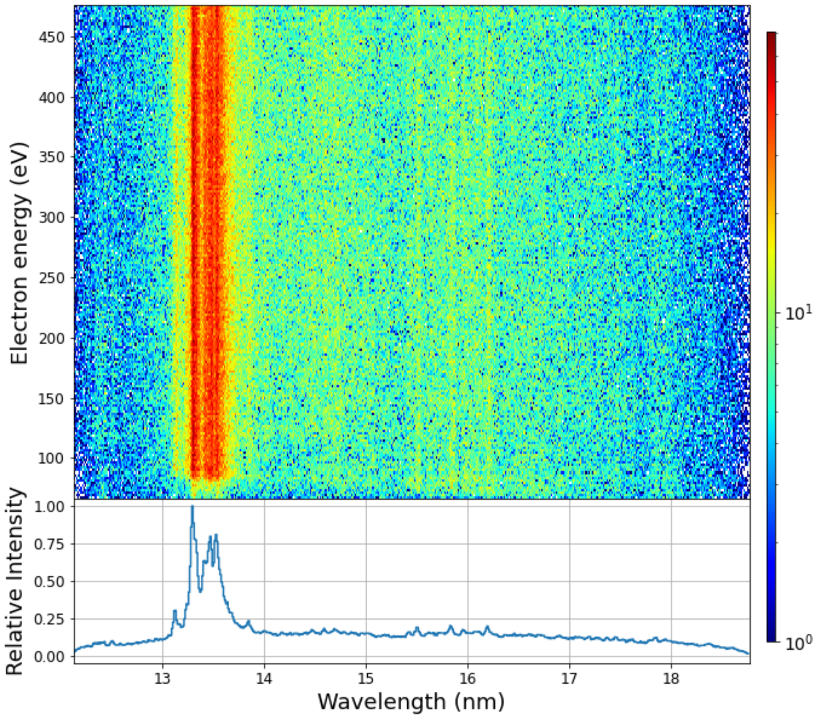

Figure 10.2: Two-dimensional spectrum of the measurement focused on Sn^{11+} with the projection along the photon wavelength.

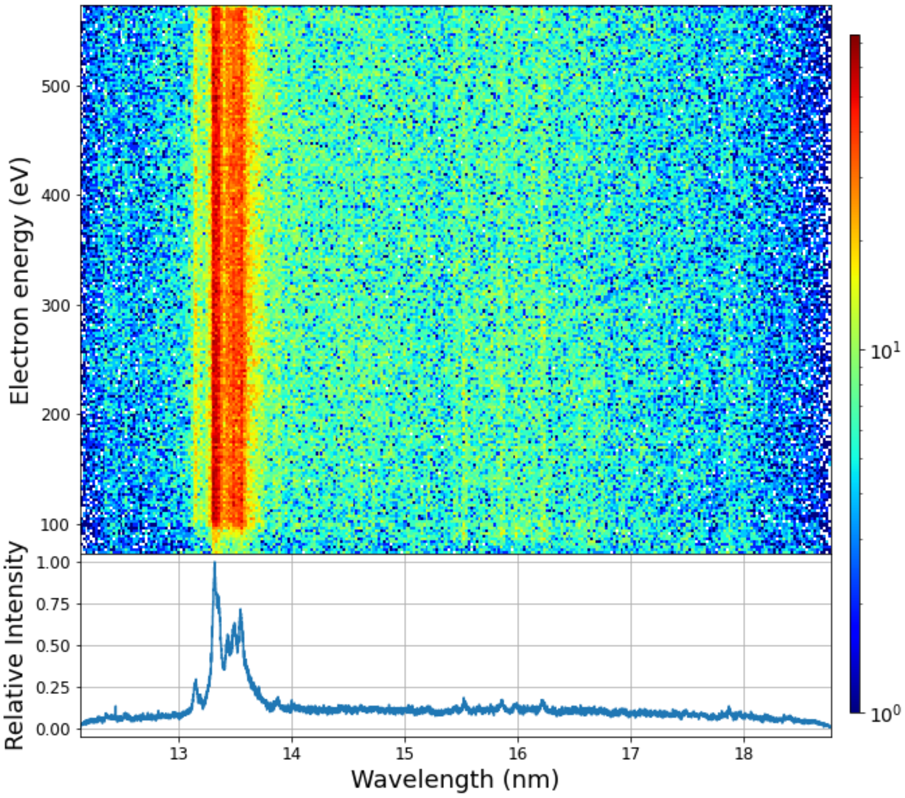

Figure 10.3: Two-dimensional spectrum of the measurement focused on Sn^{12+} with the projection along the photon wavelength.

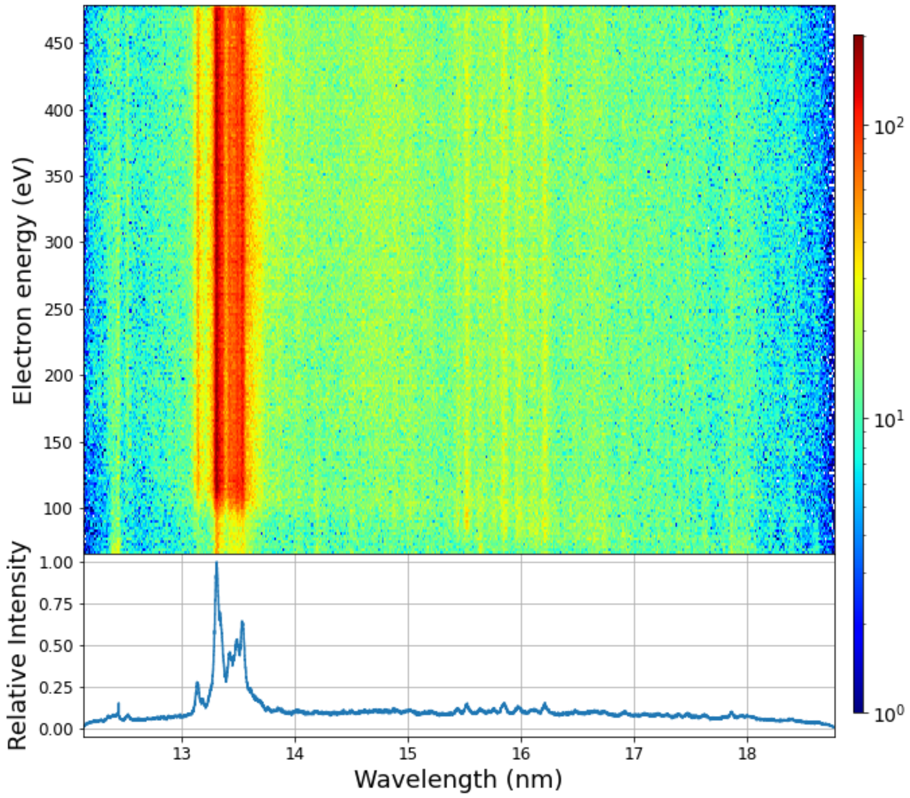

Figure 10.4: Two-dimensional spectrum of the measurement focused on Sn^{13+} with the projection along the photon wavelength.

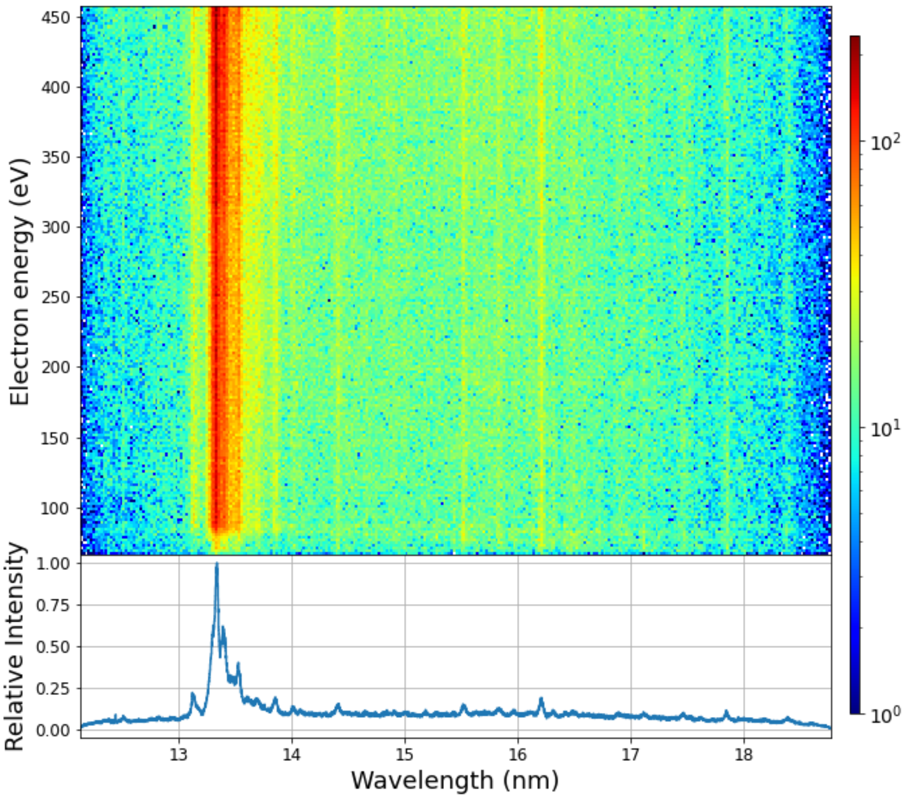

Figure 10.5: Two-dimensional spectrum of the measurement focused on Sn^{15+} with the projection along the photon wavelength.

Table 10.1: Spectral lines contained in the fast scan of with a breeding energy of 213 eV. As a wavelength error the fit uncertainty for the centroid of the gaussian fit is given. The additional systematic uncertainty due to the uncertainty of the calibration is $\Delta\lambda_{\mathrm{sys}} = 0.04\,\mathrm{nm}$.

λ(nm)	$\Delta\lambda$(nm)	I(rel.)	λ(nm)	$\Delta\lambda$(nm)	I(rel.)
12.5142	0.0011	0.0240 ± 0.0017	14.6989	0.0009	0.0697 ± 0.0028
13.1307	0.0005	0.0173 ± 0.0003	14.7442	0.0015	0.0402 ± 0.0026
13.1764	0.0012	0.086 ± 0.003	14.7922	0.0014	0.0378 ± 0.0024
13.2442	0.0007	0.152 ± 0.006	14.7922	0.0014	0.0402 ± 0.0026
13.2748	0.0025	0.135 ± 0.019	14.8824	0.0012	0.0395 ± 0.0024
13.3009	0.0005	0.748 ± 0.012	14.9720	0.0020	0.0251 ± 0.0023
13.33807	0.00029	0.550 ± 0.006	15.0193	0.0022	0.224 ± 0.023
13.4190	0.0007	0.200 ± 0.006	15.1889	0.0033	0.0134 ± 0.0022
13.4542	0.0017	0.180 ± 0.017	15.433	0.003	0.0117 ± 0.0018
13.5185	0.0024	0.326 ± 0.005	15.6338	0.0024	0.0153 ± 0.0019
13.541	0.003	0.380 ± 0.029	15.745	0.003	0.0121 ± 0.0018
13.5687	0.0021	0.316 ± 0.016	15.8413	0.0007	0.0598 ± 0.0020
13.5976	0.0011	0.231 ± 0.011	15.9642	0.0011	0.0347 ± 0.0019
13.6422	0.0007	0.120 ± 0.005	16.018	0.003	0.0118 ± 0.0018
13.6729	0.0015	0.121 ± 0.003	16.1051	0.0013	0.0285 ± 0.0018
13.7066	0.0012	0.075 ± 0.003	16.2041	0.0007	0.0526 ± 0.0020
13.7495	0.0010	0.043 ± 0.002	16.9073	0.0018	0.0144 ± 0.0014
13.8505	0.0006	0.057 ± 0.002	17.0920	0.0017	0.0151 ± 0.0014
13.9416	0.0014	0.0254 ± 0.0018	17.3832	0.0012	0.0268 ± 0.0016
14.0034	0.0015	0.0236 ± 0.0018	17.4629	0.0009	0.0345 ± 0.0016
14.0539	0.0017	0.0202 ± 0.0018	17.5299	0.0019	0.0158 ± 0.0015
14.4137	0.0024	0.0143 ± 0.0019	17.6144	0.0019	0.0165 ± 0.0015
14.464	0.003	0.0201 ± 0.0028	17.801	0.004	0.0085 ± 0.0015
14.494	0.003	0.017 ± 0.003	17.8506	0.0012	0.0282 ± 0.0016
14.6512	0.0015	0.0367 ± 0.0025	17.9500	0.0018	0.0166 ± 0.0015

Table 10.2: Spectral lines contained in the fast scan of with a breeding energy of 233 eV. As a wavelength error the fit uncertainty for the centroid of the gaussian fit is given. The additional systematic uncertainty due to the uncertainty of the calibration is $\Delta\lambda_{\mathrm{sys}} = 0.04\,\mathrm{nm}$.

λ(nm)	$\Delta\lambda$(nm)	I(rel.)
12.2916	0.0021	0.0091 ± 0.0011
12.3595	0.0007	0.0308 ± 0.0013
12.5292	0.0010	0.0268 ± 0.0016
12.8370	0.0012	0.0104 ± 0.0015
13.14472	0.00019	0.1765 ± 0.0024
13.193	0.004	0.0728 ± 0.0022
13.2469	0.0008	0.086 ± 0.004
13.2778	0.0008	0.168 ± 0.004
13.31410	0.00015	0.839 ± 0.004
13.3520	0.0003	0.572 ± 0.004
13.4311	0.0011	0.062 ± 0.005
13.4916	0.0004	0.178 ± 0.004
13.54662	0.00024	0.276 ± 0.005
13.8689	0.0006	0.0318 ± 0.0012
14.0301	0.0024	0.0131 ± 0.0019
14.280	0.005	0.0035 ± 0.0010
14.4291	0.0015	0.0134 ± 0.0010
14.4935	0.0016	0.0129 ± 0.0010
14.6087	0.0012	0.0173 ± 0.0010
14.7164	0.0012	0.0173 ± 0.0010
14.8807	0.0015	0.0178 ± 0.0013
15.0224	0.0019	0.0140 ± 0.0012
15.2034	0.0011	0.0232 ± 0.0013
15.4461	0.0012	0.0224 ± 0.0013
15.5279	0.0006	0.0490 ± 0.0015
15.6498	0.0020	0.0126 ± 0.0012
15.7578	0.0013	0.0201 ± 0.0013
15.8546	0.0004	0.0505 ± 0.0012
15.9797	0.0007	0.0322 ± 0.0011
16.091	0.003	0.0089 ± 0.0011
16.1298	0.0023	0.0114 ± 0.0012
16.2185	0.0005	0.0461 ± 0.0012
16.4850	0.0015	0.0137 ± 0.0011
16.6548	0.0019	0.0105 ± 0.0010
16.7309	0.0027	0.0074 ± 0.0010
16.9235	0.0010	0.0197 ± 0.0011
17.1000	0.0026	0.0118 ± 0.0013
17.220	0.005	0.0089 ± 0.0011
17.4005	0.0009	0.0207 ± 0.0009
17.4794	0.0007	0.0258 ± 0.0009
17.5450	0.0014	0.0124 ± 0.0008
17.6309	0.0012	0.0145 ± 0.0009
17.8129	0.0025	0.0072 ± 0.0008
17.8678	0.0006	0.0290 ± 0.0009
17.9617	0.0017	0.0102 ± 0.0008
18.0160	0.0025	0.0070 ± 0.0008
18.4001	0.0014	0.0129 ± 0.0011

Table 10.3: Spectral lines contained in the fast scan of with a breeding energy of 259 eV. As a wavelength error the fit uncertainty for the centroid of the gaussian fit is given. The additional systematic uncertainty due to the uncertainty of the calibration is $\Delta\lambda_{\text{sys}} = 0.04\,\text{nm}$.

λ(nm)	$\Delta\lambda$(nm)	I(rel.)	λ(nm)	$\Delta\lambda$(nm)	I(rel.)
12.3507	0.0021	0.0178 ± 0.0017	15.6409	0.0015	0.0190 ± 0.0015
12.3904	0.0017	0.0275 ± 0.0019	15.7553	0.0016	0.0175 ± 0.0015
12.4316	0.0010	0.0358 ± 0.0018	15.8464	0.0006	0.0571 ± 0.0017
12.5200	0.0010	0.0294 ± 0.0016	15.9739	0.0009	0.0362 ± 0.0016
13.1352	0.0004	0.195 ± 0.004	16.0910	0.0028	0.0151 ± 0.0019
13.1824	0.0009	0.092 ± 0.003	16.126	0.003	0.0131 ± 0.0019
13.30534	0.00027	0.804 ± 0.029	16.2092	0.0007	0.0485 ± 0.0018
13.3435	0.0008	0.438 ± 0.025	16.4783	0.0020	0.0182 ± 0.0018
13.4204	0.0006	0.201 ± 0.006	16.6528	0.0017	0.0214 ± 0.0019
13.4576	0.0015	0.132 ± 0.008	16.7258	0.0021	0.0172 ± 0.0018
13.4887	0.0007	0.262 ± 0.008	16.915	0.004	0.0098 ± 0.0017
13.53524	0.00024	0.402 ± 0.006	17.0925	0.0018	0.0194 ± 0.0017
13.8543	0.0012	0.0283 ± 0.0019	17.2063	0.0019	0.0176 ± 0.0017
14.0164	0.0021	0.0160 ± 0.0017	17.2873	0.0027	0.0124 ± 0.0017
14.187	0.005	0.0070 ± 0.0016	17.3906	0.0027	0.0110 ± 0.0016
14.8779	0.0022	0.0195 ± 0.0022	17.4682	0.0025	0.0131 ± 0.0017
15.0118	0.0025	0.0167 ± 0.0021	17.621	0.006	0.0057 ± 0.0016
15.1998	0.0021	0.0142 ± 0.0017	17.8600	0.0008	0.0340 ± 0.0015
15.4371	0.0014	0.0205 ± 0.0015	18.387	0.003	0.0080 ± 0.0016
15.5195	0.0006	0.0479 ± 0.0016			

Table 10.4: Spectral lines contained in the fast scan of with a breeding energy of 285 eV. As a wavelength error the fit uncertainty for the centroid of the gaussian fit is given. The additional systematic uncertainty due to the uncertainty of the calibration is $\Delta\lambda_{\mathrm{sys}} = 0.04\,\mathrm{nm}$.

λ(nm)	$\Delta\lambda$(nm)	I(rel.)	λ(nm)	$\Delta\lambda$(nm)	I(rel.)
12.1632	0.0013	0.079 ± 0.007	13.6842	0.0012	0.0506 ± 0.0021
12.2039	0.0012	0.075 ± 0.006	13.7128	0.0012	0.0412 ± 0.0023
12.2461	0.0016	0.061 ± 0.006	13.7554	0.0014	0.0142 ± 0.0008
12.2807	0.0017	0.052 ± 0.006	13.8566	0.0008	0.0158 ± 0.0008
12.3273	0.0014	0.054 ± 0.007	14.0189	0.0004	0.0322 ± 0.0007
12.3646	0.0023	0.037 ± 0.006	14.065	0.004	0.0038 ± 0.0006
12.4054	0.0026	0.028 ± 0.007	14.178	0.003	0.0032 ± 0.0005
12.4442	0.0033	0.021 ± 0.007	14.2508	0.0025	0.0045 ± 0.0005
12.5007	0.0021	0.021 ± 0.007	14.4193	0.0005	0.0232 ± 0.0006
12.5262	0.0039	0.027 ± 0.008	14.4965	0.0019	0.0057 ± 0.0005
12.7627	0.0034	0.0037 ± 0.0006	14.5684	0.0016	0.0069 ± 0.0005
12.8236	0.0005	0.0285 ± 0.0007	14.6546	0.0010	0.0115 ± 0.0005
12.9184	0.0025	0.0062 ± 0.0007	14.748	0.006	0.0019 ± 0.0006
12.9551	0.0027	0.0062 ± 0.0007	15.0155	0.0014	0.0118 ± 0.0007
13.0533	0.0012	0.0195 ± 0.0011	15.1998	0.0003	0.0509 ± 0.0010
13.0936	0.0020	0.0191 ± 0.0014	15.445	0.003	0.0047 ± 0.0007
13.1319	0.0003	0.1153 ± 0.0014	15.5230	0.0006	0.0289 ± 0.0008
13.1774	0.0004	0.0602 ± 0.0012	15.6424	0.0009	0.0190 ± 0.0008
13.2703	0.0005	0.134 ± 0.004	15.7146	0.0014	0.0116 ± 0.0007
13.3004	0.0003	0.388 ± 0.003	15.8491	0.0009	0.0285 ± 0.0012
13.3378	0.0001	0.828 ± 0.003	15.9718	0.0012	0.0194 ± 0.0011
13.3813	0.0005	0.1452 ± 0.0026	16.1285	0.0012	0.0194 ± 0.0011
13.4134	0.0004	0.1592 ± 0.0026	16.2173	0.0003	0.0872 ± 0.0017
13.4556	0.0005	0.1081 ± 0.0023	16.9102	0.0012	0.0110 ± 0.0007
13.4883	0.0005	0.0968 ± 0.0021	17.1206	0.0017	0.0078 ± 0.0007
13.5300	0.0002	0.1710 ± 0.0019	17.4618	0.0005	0.0220 ± 0.0007
13.577	0.004	0.0465 ± 0.0024	17.6142	0.0021	0.0045 ± 0.0006
13.6105	0.0017	0.0680 ± 0.0023	17.8449	0.0003	0.0301 ± 0.0006
13.6444	0.0013	0.0491 ± 0.0017	18.3808	0.0008	0.0164 ± 0.0008

Table 10.5: Spectral lines contained in the fast scan of with a breeding energy of 332 eV. As a wavelength error the fit uncertainty for the centroid of the gaussian fit is given. The additional systematic uncertainty due to the uncertainty of the calibration is $\Delta\lambda_{\mathrm{sys}} = 0.04\,\mathrm{nm}$.

λ(nm)	$\Delta\lambda$(nm)	I(rel.)	λ(nm)	$\Delta\lambda$(nm)	I(rel.)
12.2762	0.0012	0.0099 ± 0.0007	14.9999	0.0017	0.0111 ± 0.0009
12.3352	0.0009	0.0170 ± 0.0008	15.1879	0.0026	0.0069 ± 0.0009
12.3756	0.0008	0.0218 ± 0.0008	15.2801	0.0024	0.0075 ± 0.0009
12.5110	0.0008	0.0242 ± 0.0011	15.431	0.003	0.0058 ± 0.0009
12.8235	0.0013	0.0167 ± 0.0013	15.5211	0.0004	0.0549 ± 0.0012
13.12761	0.00018	0.1121 ± 0.0013	15.6349	0.0016	0.0117 ± 0.0009
13.1716	0.0005	0.0410 ± 0.0012	15.8089	0.0019	0.0185 ± 0.0016
13.26506	0.00010	0.141 ± 0.007	15.8421	0.0012	0.0307 ± 0.0016
13.2981	0.0007	0.371 ± 0.009	15.9598	0.0013	0.0184 ± 0.0011
13.33546	0.00022	0.868 ± 0.009	16.082	0.003	0.0096 ± 0.0013
13.3866	0.0003	0.502 ± 0.006	16.1186	0.0019	0.0159 ± 0.0013
13.4480	0.0008	0.1202 ± 0.0026	16.20595	0.00029	0.0944 ± 0.0017
13.4835	0.0008	0.0969 ± 0.0026	16.3115	0.0013	0.0183 ± 0.0011
13.52527	0.00025	0.1795 ± 0.0024	16.4245	0.0019	0.0120 ± 0.0011
13.6033	0.0008	0.0270 ± 0.0015	16.4939	0.0014	0.0170 ± 0.0011
13.6914	0.0011	0.0188 ± 0.0016	16.7238	0.0026	0.0068 ± 0.0008
13.8506	0.0004	0.0928 ± 0.0024	16.8923	0.0010	0.0172 ± 0.0009
14.0106	0.0011	0.0311 ± 0.0018	17.1178	0.0012	0.0148 ± 0.0009
14.0787	0.0026	0.0125 ± 0.0017	17.4600	0.0005	0.0249 ± 0.0009
14.236	0.006	0.0038 ± 0.0011	17.5192	0.0010	0.0162 ± 0.0007
14.4073	0.0004	0.0614 ± 0.0015	17.6145	0.0014	0.0096 ± 0.0007
14.557	0.004	0.0055 ± 0.0011	17.8462	0.0004	0.0368 ± 0.0009
14.650	0.003	0.0067 ± 0.0011	18.1809	0.0014	0.0158 ± 0.0011
14.8442	0.0018	0.0103 ± 0.0009	18.3888	0.0010	0.0236 ± 0.0013
14.9014	0.0014	0.0139 ± 0.0009			

Table 10.6: Fit results for the electron energy projections produced from the data of the Sn^{11+}-measurement. The denoted relative oscillator strengths f_{rel} add up to 100 for each fit. Again, they are obtained by weighting the intensity of the individual Van Regemorter curves at threshold by the square of the threshold energy ΔE^2. In the second to last column the total photon counts in the denoted wavelength range are given. These are used to compare the contributions of the different thresholds between wavelength ranges and measurements.

λ (nm)	Thresholds (eV)	f_{rel}	Counts	χ^2_{red}
12.0 - 12.6	75/116/197	42/33/25	24657	1.11
12.6 -13.0	73/95/128/224	33/11/18/37	27316	1.63
13.0 - 13.2	69/88/113/217	18/42/14/26	26820	1.48
13.4 - 13.6	74/90/118/235	10/47/13/30	81405	2.31
13.6 - 13.8	68/87/145/185	10/53/22/15	100684	2.09
13.8 - 14.0	69/83/155	11/46/43	41949	2.75
14.0 - 14.4	51/83/120/151/197	14/24/22/13/27	44814	1.88
14.4 - 14.8	61/86/133/197	20/27/30/22	48450	1.43
14.8 - 15.2	50/80/148/203	20/33/29/18	43506	1.46
15.2 - 15.6	51/86/156/187	23/40/26/11	42553	2.15
15.6 - 15.9	52/81/149	11/58/31	35460	2.08
15.9 - 16.15	71/113	76/24	29110	1.38
16.15 - 16.5	71/126	76/24	1.75	38232
16.5 - 17.0	71/150	69/31	49179	1.13
17.0 - 17.5	39/97/125	58/4/38	37714	1.70
17.5 - 18.0	50/118	64/36	37714	1.70
18.0 - 18.5	75/118	75/25	28599	1.59

Table 10.7: Fit results for the electron energy projections produced from the data of the Sn^{12+}-measurement. The denoted relative oscillator strengths f_{rel} add up to 100 for each fit. Again, they are obtained by weighting the intensity of the individual Van Regemorter curves at threshold by the square of the threshold energy ΔE^2. In the second to last column the total photon counts in the denoted wavelength range are given. These are used to compare the contributions of the different thresholds between wavelength ranges and measurements.

λ (nm)	Thresholds (eV)	f_{rel}	Counts	χ^2_{red}
12.15 - 12.6	60/85/104/139/200	21/17/6/10/46	13339	1.34
12.6 - 13.1	59/88/115/185	24/25/25/26	19396	1.82
13.1 - 13.22	50/89/126	14/57/29	11757	1.11
13.22 - 13.4	72/88/147/210	20/48/12/20	48627	2.02
13.4 - 13.45	72/88/100/149/189	18/40/9/14/19	12545	1.48
13.45 - 13.52	88/101/144/200	38/17/15/30	20166	3.49
13.52 - 13.6	83/169	62/38	22636	1.54
13.6 - 14.0	83/105/147/182/232	18/36/8/17/21	36885	1.44
14.0 - 14.5	72/112/142/197	37/14/16/34	30488	1.39
14.5 - 15.0	82/126/165/215	51/22/19/8	29406	1.22
15.0 - 15.3	67/99/145/195	42/14/16/28	16778	1.11
15.3 - 15.8	72/123/201	43/19/38	29399	1.11
15.8 - 15.9	72/127	66/34	6872	1.32
15.9 - 16.1	72	100	12178	1.56
16.1 - 16.3	73/233	47/53	12694	1.25
16.3 - 16.8	74/147	67/33	27433	1.68
16.8 - 17.8	70/115/136	61/14/25	44588	2.48
17.8 - 18.3	68/120/192	53/17/30	18640	1.21

Table 10.8: Fit results for the electron energy projections produced from the data of the Sn^{13+}-measurement. The denoted relative oscillator strengths f_{rel} add up to 100 for each fit. Again, they are obtained by weighting the intensity of the individual Van Regemorter curves at threshold by the square of the threshold energy ΔE^2. In the second to last column the total photon counts in the denoted wavelength range are given. These are used to compare the contributions of the different thresholds between wavelength ranges and measurements.

λ (nm)	Thresholds (eV)	f_{rel}	Counts	χ^2_{red}
12.1 - 12.3	65/82/119/180	19/14/29/38	15224	1.71
12.3 - 12.45	75/98/120	61/22/17	25549	1.66
12.45 - 12.6	68/95/112/179	39/15/19/28	21712	1.27
12.6 - 13.05	68/88/115/184/210	30/17/14/25/13	70021	2.30
13.05 - 13.2	67/90/168	23/62/15	57644	1.83
13.2 - 13.27	70/90/130/170	12/51/27/11	32863	1.48
13.27 - 13.32	41/92/169	7/80/13	88702	2.31
13.32 - 13.39	69/90/144/177	16/56/7/21	92022	2.23
13.39 - 13.45	69/88/122/170	16/53/11/20	60057	2.03
13.45 - 13.5	69/88/160	19/59/22	59894	1.72
13.5 - 13.57	66/87/152	18/61/21	88162	3.10
13.57 - 13.7	66/87/117/155/174	20/43/8/14/14	65741	1.72
13.7 - 14.1	50/85/120/176	21/36/25/18	104824	2.36
14.1 - 14.35	45/85/129/171	35/36/8/21	56889	1.38
14.35 - 14.7	68/87/125/176	41/21/13/25	83951	1.97
14.7 - 14.85	67/85/119/163	41/21/12/26	38558	1.70
14.85 - 14.95	70/82/124/163	39/22/21/18	25871	1.31
14.95 - 15.1	70/83/114/191	35/27/10/28	37344	1.86
15.1 - 15.35	65/124/141	48/18/34	55751	1.41
15.35 - 15.47	70/130/171	45/12/43	28920	1.12
15.47 - 15.7	74/165	83/17	28110	1.12
15.7 - 15.8	69/93/125	63/14/23	25452	1.88
15.8 - 15.9	76/106/138	78/5/17	29437	3.22
15.9 -16.05	65/71/150	5/82/13	39189	1.36
16.05 - 16.3	69/141	82/18	65987	1.39
16.3 - 16.8	69/130	87/13	114724	2.29
16.8 - 17.0	69/103/141	88/4/8	41300	1.78
17.0 - 17.32	70/101/138/171	72/7/12/9	63515	1.98
17.32 - 17.52	69/104/130	80/8/12	37188	1.10
17.52 - 17.75	69/125	88/12	37894	1.47
17.75 - 18.0	71/128	88/12	44314	1.58
18.0 - 18.5	49	100	63823	1.30

Table 10.9: Fit results for the electron energy projections produced from the data of the Sn^{15+}-measurement. The denoted relative oscillator strengths f_{rel} add up to 100 for each fit. Again, they are obtained by weighting the intensity of the individual Van Regemorter curves at threshold by the square of the threshold energy ΔE^2. In the second to last column the total photon counts in the denoted wavelength range are given. These are used to compare the contributions of the different thresholds between wavelength ranges and measurements.

λ (nm)	Thresholds (eV)	f_{rel}	Counts	χ^2_{red}
12.0 - 12.5	50/82/116/185/296/378	8/5/12/12/30/33	22483	1.76
12.5 - 13.0	60/83/118/190/309/442	10/4/9/12/28/38	42216	1.66
13.0 - 13.2	60/88/119/195/315	11/20/9/11/49	33016	1.91
13.2 - 13.35	52/87/101/149/310/384	4/25/4/4/46/18	96768	3.62
13.35 - 13.5	47/87/134/169/333/364/444	3/18/5/8/29/12/26	92807	3.95
13.5 - 13.65	50/85/115/170/326/386/452	4/14/3/12/30/7/29	50884	2.44
13.65 - 13.8	50/85/118/170/318/385/468	4/11/2/14/37/6/27	32203	1.62
13.8 - 14.0	65/90/113/167/295/395	14/20/8/21/13/24	34848	2.59
14.0 - 14.3	50/76/116/182/225/297/375	12/19/9/19/5/9/27	42992	2.87
14.3 - 14.6	81/124	83/17	44576	1.85
14.6 - 15.0	80/124	83/17	54108	3.29
15.0 - 15.2	70/82/119	55/31/14	26322	1.28
15.2 - 15.6	76/155	73/27	56301	3.74
15.6 - 15.9	82/155	79/21	43997	2.41
15.9 - 16.3	82/170	76/24	60086	3.74
16.3 - 16.6	76	100	40273	1.71
16.6 - 17.0	74	100	47158	1.40
17.0 - 17.5	76	100	54229	2.04
17.5 - 18.0	76	100	45437	1.45
18.0 - 18.5	65/119	82/18	36750	1.83

Table 10.10: Configurations used in the configuration interaction for Sn^{11+}, Sn^{12+} and Sn^{15+}, separated by degree of excitation. Continuation of Table 7.1.

Ion	State ensemble	Configuration
Sn^{11+}	Ground state	4s2 4p6 4d3
	Singly excited	4s2 4p5 4d4
		4s2 4p6 4d2 4f1
	Doubly excited	4s2 4p6 4d1 4f2
		4s2 4p5 4d3 4f1
		4s2 4p4 4d5
		4s1 4p6 4d4
	Triply excited	4s2 4p5 4f3
		4s2 4p5 4d2 4f2
		4s2 4p4 4d4 4f1
		4s2 4p3 4d6
		4s1 4p5 4d5
		4s2 4p6 4d3 4f1
Sn^{12+}	Ground state	4s2 4p6 4d2
	Singly excited	4s2 4p5 4d3
		4s2 4p6 4d1 4f1
	Doubly excited	4s2 4p6 4f2
		4s2 4p5 4d2 4f1
		4s2 4p4 4d4
		4s1 4p6 4d3
	Triply excited	4s2 4p5 4d1 4f2
		4s2 4p4 4d3 4f1
		4s2 4p3 4d5
		4s1 4p6 4d2 4f1
		4s1 4p6 4d2 4f1
Sn^{15+}	Ground state	4s2 4p5
	Singly excited	4s2 4p4 4d1
		4s2 4p4 4f1
	Doubly excited	4s2 4p3 4d2
		4s1 4p6
	Triply excited	4s2 4p3 4d1 4f1
		4s1 4p4 4d2

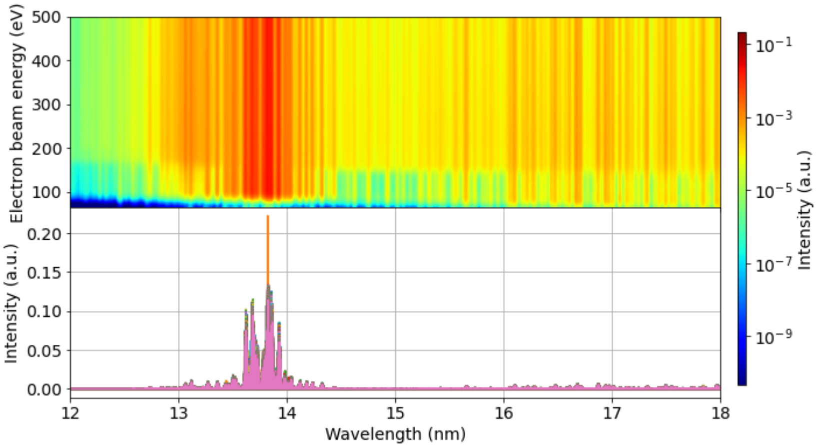

Figure 10.6: **Top:** Theoretical two-dimensional spectrum resulting from spectra of Sn^{12+} calculated via the CRM of FAC for many different electron energies. The result is has the same form as the two dimensional map shown in Figure 6.1. **Bottom:** Individual CRM-spectra of Sn^{12+} at different electron energies in different colors. Each of those spectra represents one line in the two-dimensional spectrum above.

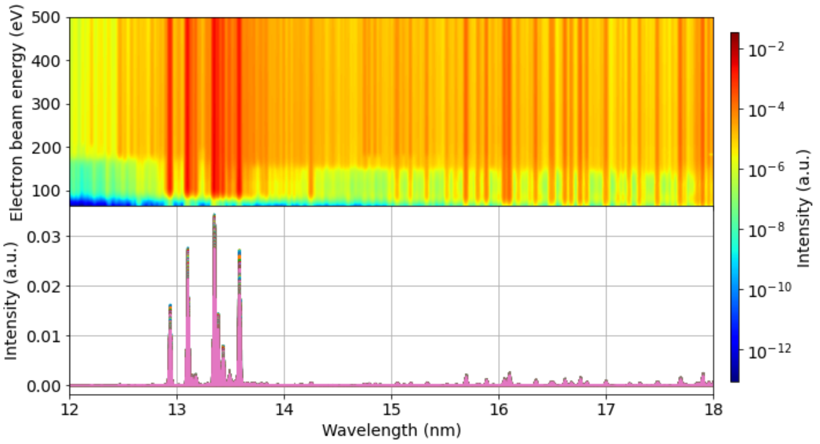

Figure 10.7: **Top:** Theoretical two-dimensional spectrum resulting from spectra of Sn^{13+} calculated via the CRM of FAC for many different electron energies. The result is has the same form as the two dimensional map shown in Figure 6.1. **Bottom:** Individual CRM-spectra of Sn^{13+} at different electron energies in different colors. Each of those spectra represents one line in the two-dimensional spectrum above.

Acknowledgements

Lastly I want to thank the many people who supported me during the writing of this thesis. Prof. Dr. José Crespo López-Urrutia, for allowing me to conduct this work on the topic of my liking, with much free room to develop my own ideas on how to tackle the topic, while continuously providing helpful input. I'd also to thank Kehlan and Filipé for support in running the experiment during their stays at the MPIK, as well as Oscar and John for lots of helpful suggestions on how to improve the measurements and introducing me to the topic of tin nanolithography, including the invitation to the EUV Litho. Source workshop this year. Special thanks as well to the people reading through drafts of this work, providing information on which parts could be improved upon. Additionally I'd like to extend those thanks to the many people in the work group for the nice atmosphere and many relaxing lunch breaks. In the end I have to thank my family of course, providing support throughout the year and allowing me to fully focus on my work towards the end.

Erklärung

Ich versichere, dass ich diese Arbeit selbstständig verfasst und keine anderen als die angegebenen Quellen und Hilfsmittel benutzt habe.

Heidelberg, den 07.12.22, Max